



UNIVERSITÀ DI PISA

Department of Nuclear Engineering

CFD Verification and Validation of Twin Parallel Jets

Supervisors

Dr. Francesco D'Auria

University of Pisa

Dr. Yassin A. Hassan

Texas A&M University

Student

Giacomo Busco

Abstract

The present thesis work has been realized during a six-months internship period at Texas A&M University, Department of Nuclear Engineering.

A CFD Verification and Validation study of twin parallel jets has been conducted using the computational fluid dynamics code Ansys-CFX. The twin jets water facility resides in the Thermal-Hydraulic research laboratory of Texas A&M university. Particle Image Velocimetry (PIV) and Laser Doppler Anemometry (LDA) measurements were carried out to investigate the flow field and for obtaining high fidelity experimental data for benchmarking different numerical models. Experimental data were also taken as benchmark for the V&V first benchmark problem for the ASME V&V30 standard committee “Verification and Validation in Computational Nuclear System Thermal Fluids Behavior”, whose scope is to provides the best practices and procedures for verification and validation of software used to calculate the nuclear system thermal fluid behavior, including system analysis and computational fluid dynamics and the coupling of them.

The scope of this study is to apply the V&V best practices and to assess different mathematical models capabilities (Reynolds Averaged Navier-Stokes Equations) for the twin jet physics, since in new generation nuclear reactors designs, there are present some zones in the core coolant system where there is the formation of parallel jets (Sodium Fast Reactors and Very High Temperature Reactors) and a bad mixing of coolant coming from different zones of the reactor core, at different temperatures, could lead to thermal striping phenomena at the fluid-structure boundary.

The results of this work have been presented during the 2016 ASME V&V Symposium in Las Vegas, Nevada, in May 2016.

Contents

1 Introduction.....	6
2 Twin Jets Water Facility	8
Justification.....	8
Physics.....	10
Facility description	11
Experimental data.....	15
Mean Velocity	17
Turbulence intensity	18
Reynolds stresses.....	19
Validation experimental data.....	19
3 Verification and Validation.....	21
Verification assessment	23
Code verification	23
Solution verification	24
Discretization error.....	26
Validation	32
Validation nomenclature	34
4 V&V Twin Jets	38
Ansys CFX CFD code	38
Discretization method	38
Order of accuracy	39
Advection term.....	40
Diffusion Terms	40
Pressure Gradient Term.....	40
Solution Strategy	40
Residuals normalization procedure	42
Boundary Conditions.....	42
Inlet Boundary conditions	42
Outlet boundary condition.....	43
Turbulence Models	43
<i>k</i> – <i>epsilon</i> turbulence model.....	44

<i>k</i> – <i>omega</i> -based Shear Stress Transport model	44
SSG Reynolds stress transport turbulence model.....	44
Mesh	45
Solution Verification	48
System Response Quantities	50
Simulations control	51
Solution Validation.....	51
5 Results.....	53
<i>V_y</i> Contour plots	53
<i>V_y</i> at <i>Y/a</i> = 1.4	55
<i>V_y</i> at <i>Y/a</i> = 4.2.....	58
<i>V_y</i> at <i>Y/a</i> = 7.....	61
<i>V_y</i> at <i>Y/a</i> = 10.....	64
<i>V_y</i> at <i>Y/a</i> = 11.5.....	67
<i>V_x</i> at <i>Y/a</i> = 1.4	70
<i>V_x</i> at <i>Y/a</i> = 4.2.....	73
<i>V_x</i> at <i>Y/a</i> = 7	76
<i>V_x</i> at <i>Y/a</i> = 10.....	79
<i>V_x</i> at <i>Y/a</i> = 11.5.....	82
Reynolds Stress Tensor components at <i>Y/a</i> = 1.4.....	85
Reynolds Stress Tensor components at <i>Y/a</i> = 4.2.....	86
Reynolds Stress Tensor components at <i>Y/a</i> = 7 a.....	87
Reynolds Stress Tensor components at <i>Y/a</i> = 10.....	88
Reynolds Stress Tensor components at <i>Y/a</i> = 11.5.....	89
Merging Point (MP) and Combining Point (CP)	90
Uniform Inlet Velocity Profile	90
Experimental Inlet Velocity Profile.....	91
Summary	92
6 Comments and Future Work.....	93
7 References.....	97

1 Introduction

A Verification and Validation (V&V) study has been performed for the ASME V&V30 Subcommittee – First Benchmark Problem: Twin Jets Computational Fluid Dynamics (CFD) Numeric Model Validation [1].

The ASME V&V30 “Verification and Validation in Computational Nuclear System Thermal Fluids Behavior”, provides the practices and procedures for verification and validation of software used to calculate the nuclear system thermal fluid behavior, including system analysis and computational fluid dynamics and the coupling of them [1].

The scope of the first benchmark problem is to investigate the physics and CFD simulation capabilities of two parallel water jets entering in a vertical tank of water.

The study of the mixing of two parallel jets is an important thermal hydraulic aspect that can be found in some of the new nuclear systems, like metal-cooled reactors and very high temperature reactors, where great attention is given to some regions of the core coolant system, for example the outlet/inlet plenum, where a not uniform and efficient thermal turbulent mixing of the coolant, coming from different regions of the reactor core at different temperatures, could cause some fluid/structure problems like, thermal striping due to random coolant temperature fluctuations or thermal stratifications caused by an inefficient coolant mixing, leading to high cycle thermal fatigue and potential crack initiation at the surface level of the structure. For these reasons, mixing conditions of the core coolant exit plenum, needs to be accurately evaluated and fully understood.

The V&V ultimate goal is validation, defined as the process of determining the degree to which a mathematical model is an accurate representation of the real world, from the prospective of the intended use of the model [5]. Validation must be preceded by code and solution verification. Code verification establishes that the code accurately solves the mathematical model implemented in the code, i.e. the code is free of mistakes and its numerical algorithm is convergent. Solution verification estimates the numerical accuracy of a particular calculation. The estimation of an uncertainty range, within which the simulation modelling error lies, is the primary objective of the validation process and it is accomplished by comparing a simulation results with the available

experimental data. There can be no validation without experimental data, with which to compare the results of the simulations.

In this study the focus is on the isothermal mixing process of water, coming from two parallel jets, and its scope is to evaluate the sensitivity of the CFD simulation results from the use of different turbulence models and boundary conditions. After the solution verification phase, mainly focused on a mesh sensitivity study, quantitative estimation of the modelling error and the uncertainties of the results, have been evaluated for the model validation part. The next step, which will not be presented in this work, will be the introduction of a temperature difference in the two interacting jets, to better evaluate the influence of thermal turbulent mixing and buoyancy effects.

The experimental data velocity field was measured using Particle Image Velocimetry (PIV) and Laser Doppler Anemometry (LDA) techniques, with measurement uncertainties estimated using accepted ASME practices for experimental uncertainty (ASME PTC 19.1 Test Uncertainty) [2].

The CFD simulations were conducted using the verified, element-based finite volume CFD code, Ansys-CFX and, for each simulation, the numerical results have been verified by applying Roache's Grid Convergence Index (GCI), for the estimation of the numerical error uncertainty. In a second phase of this work, the results have been validated by using the approach proposed in the ASME V&V-20 "Standard for Verification and Validation in Computational Fluid Dynamics and Heat Transfer" ASME [3], for the estimation of the modelling error and its associated uncertainty.

2 Twin Jets Water Facility

Justification

The turbulent mixing of parallel jets can be found, as physical phenomenon, in some of the new generation concept nuclear reactors, such as very high temperature reactors (VHTR), and liquid metal cooled fast reactors (LMFR). In their reactor core coolant system design, the imposed flow path lead to the formation of parallel jets at different temperature, in some regions. Those regions are, for example, the lower plenum of the very high temperature reactors and the upper plenum of the sodium cooled fast reactors and, due to the differences in temperatures of the different mixing flows arising from the core fuel assemblies, and inhomogeneous mixing, it could cause the thermal striping phenomenon at the fluid-structure boundary and, depending on the attenuation of the temperature fluctuations at the boundary, could potentially lead to thermal fatigue issues and cracks initiations at the surface of the structure.

In the following picture is presented an example of the outlet region of the Japanese Sodium Fast Reactor (JSFR) cooling system [4], where there is the potential for a thermal fatigue issue in the bottom of the Upper Instrument System (UIS), due to the mixing of two different families of jets:

- Hot sodium from the fuel assemblies region.
- Cold sodium from control rod channels and blanket fuel assemblies.

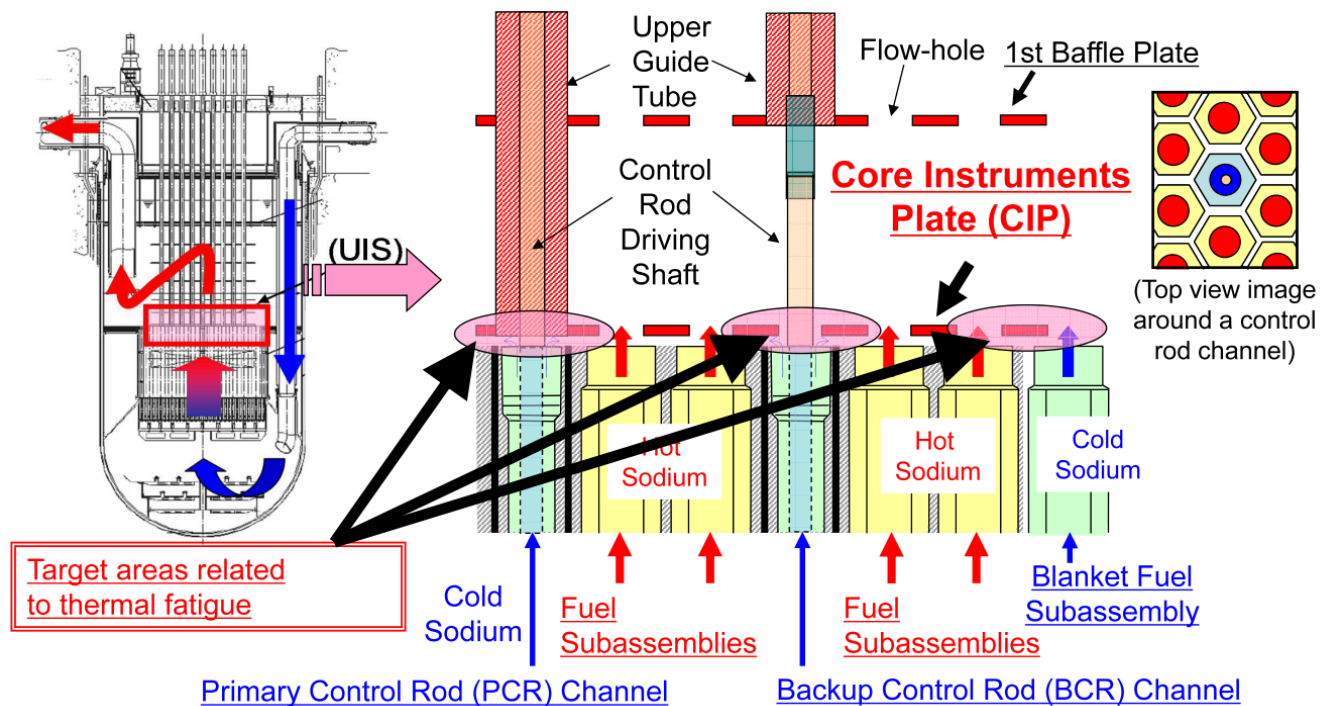


Fig. 2.1 Upper Instrument System representation of the JSFR

The next figure, instead, shows the half of the VHTR cross section of the lower plenum, the various jets of different dimensions are highlighted.

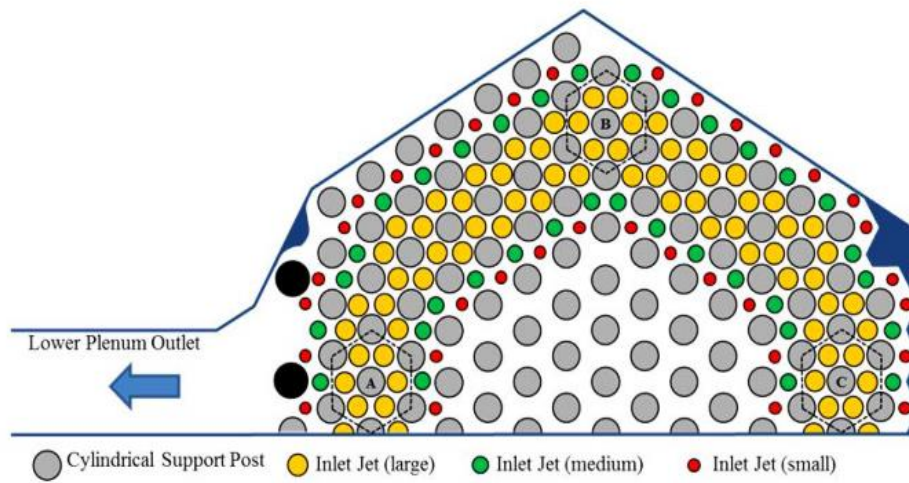


Fig. 2.2 VHTR Lower plenum cross section

Because of the infeasibility and impracticality of conducting true validation experiments on most complex systems like a reactor coolant system, the method, for the evaluation of the simulation capabilities of a general code, is to use a complexity hierarchy approach. It divides the complex engineering system of interest, into multiple, progressively simpler tiers. The strategy is to assess how accurately the computational results compare with the experimental data, with quantified uncertainty estimates at multiple degree of physics coupling and geometric complexity, accumulating, in this way, validation evidence, with the focus always being on the complete system.

Under this point of view, the main purpose of the twin jets water facility is to investigate one part of the physics of the problem and thanks to the experimental measurement, gives the possibility to validate different CFD codes and models.

In the present benchmark activity, the main interest is on the isothermal mixing of the two jets with equal inlet mean velocities, in order to evaluate the capabilities of different turbulence models for this simple case. The next step should be the introduction of a temperature and velocity difference between the two jets, increasing the degree of physics coupling of the problem.

Physics

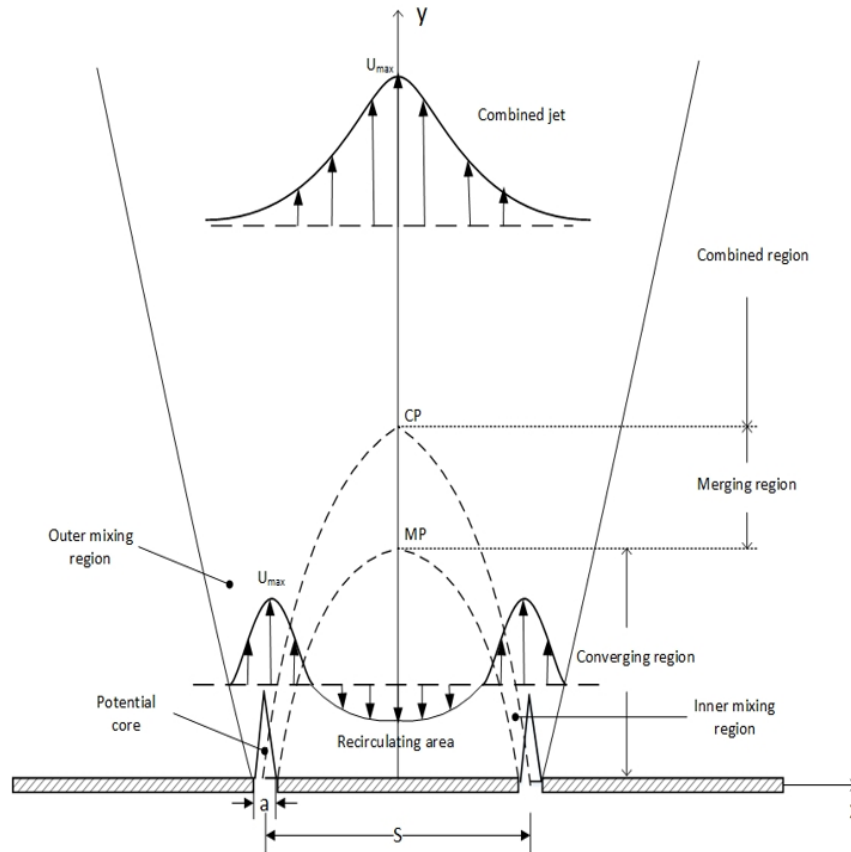


Fig. 2.3 Twin Jets Flow field characteristics [2]

Due to the high imposed velocity field, and the high relative velocity between the jets and the surrounding liquid, a sub atmospheric region is created in the vicinity of the inlet region, resulting in the mutual entrainment of the two jets, being so deflected towards each other. The two initially separate jets, tends to combine into a single jet downstream.

The flow field can be divided in to three different regions: *converging region*, *merging region* and *combined region*.

The *converging region* is the region between the inlet zone of the two jets and the *merging point* (MP), defined as the point along the symmetry axis, where the velocity component in the streamwise direction V_y , is zero (*stagnation point*). In the converging region there is the formation of a sub-atmospheric zone, called *mixing region*, which is defined as the region between the common wall of the two jets (*dividing wall*) and the inner part of the shear layer of the jets. In this region the central part of the velocity profile is reversed, creating a local reverse flow in the opposite direction of the main two jets flow direction, increasing the turbulent mixing. The mixing does not only

happen between the jets themselves but also between the jets and the static surrounding fluid that was entrained, as a result of shear forces created.

The entrainment of the two jets continue after the merging point (MP) in the *merging region*, which is the region between the merging point and the *combining point* (CP), defined as the point where the velocity component in the streamwise direction V_y , along the symmetry axis, reaches its maximum. Downstream after the combining point, there is the *combined region* where the two jets merge completely forming a single jet.

The *potential region* is the region close to the jet outlet section where the centerline velocity of the jet flow, is the same as the outlet section of the jet.

Facility description

In this section there will be reported some technical drawings and data about the twin jet water facility [2].

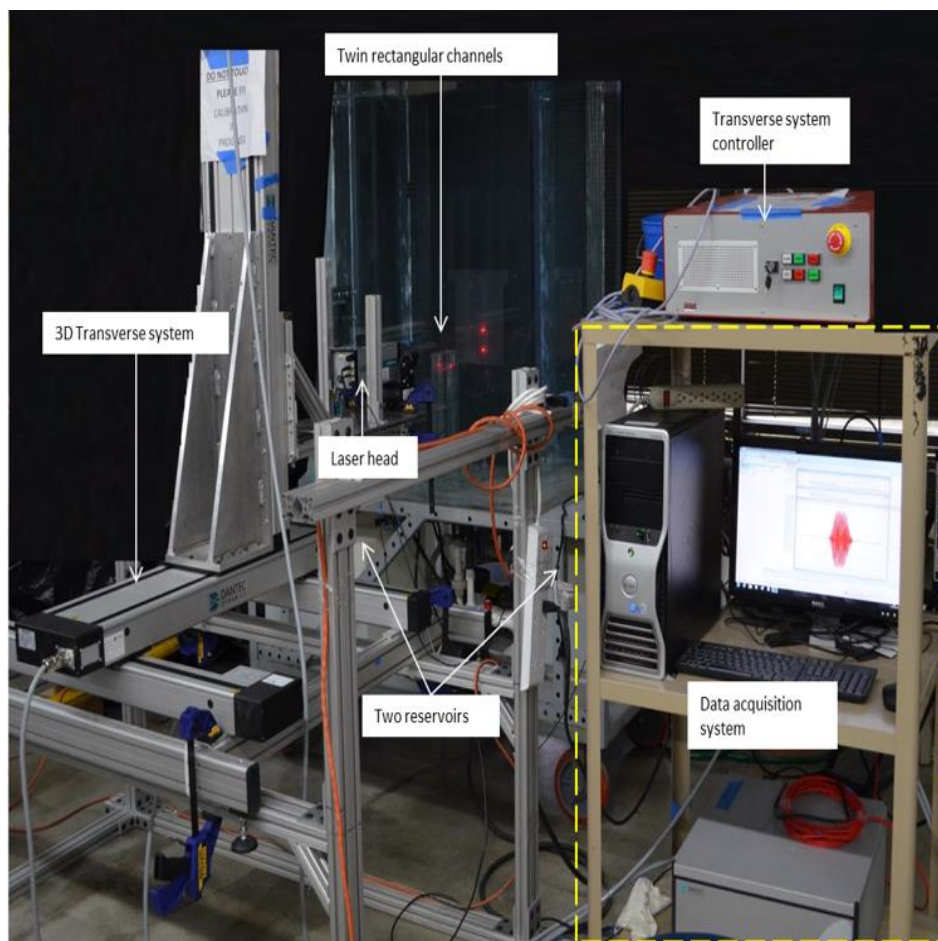


Fig. 2.4 Facility setup overview

The rectangular acrylic tank had a capacity of 0.76 m^3 . In the center of the tank is placed the jet nozzles assembly and, at the two sides of the tank are present two outflow rectangular plates, for the outflow of the water from the tank. The tank is closed with a flat plate, with a rectangular opening.

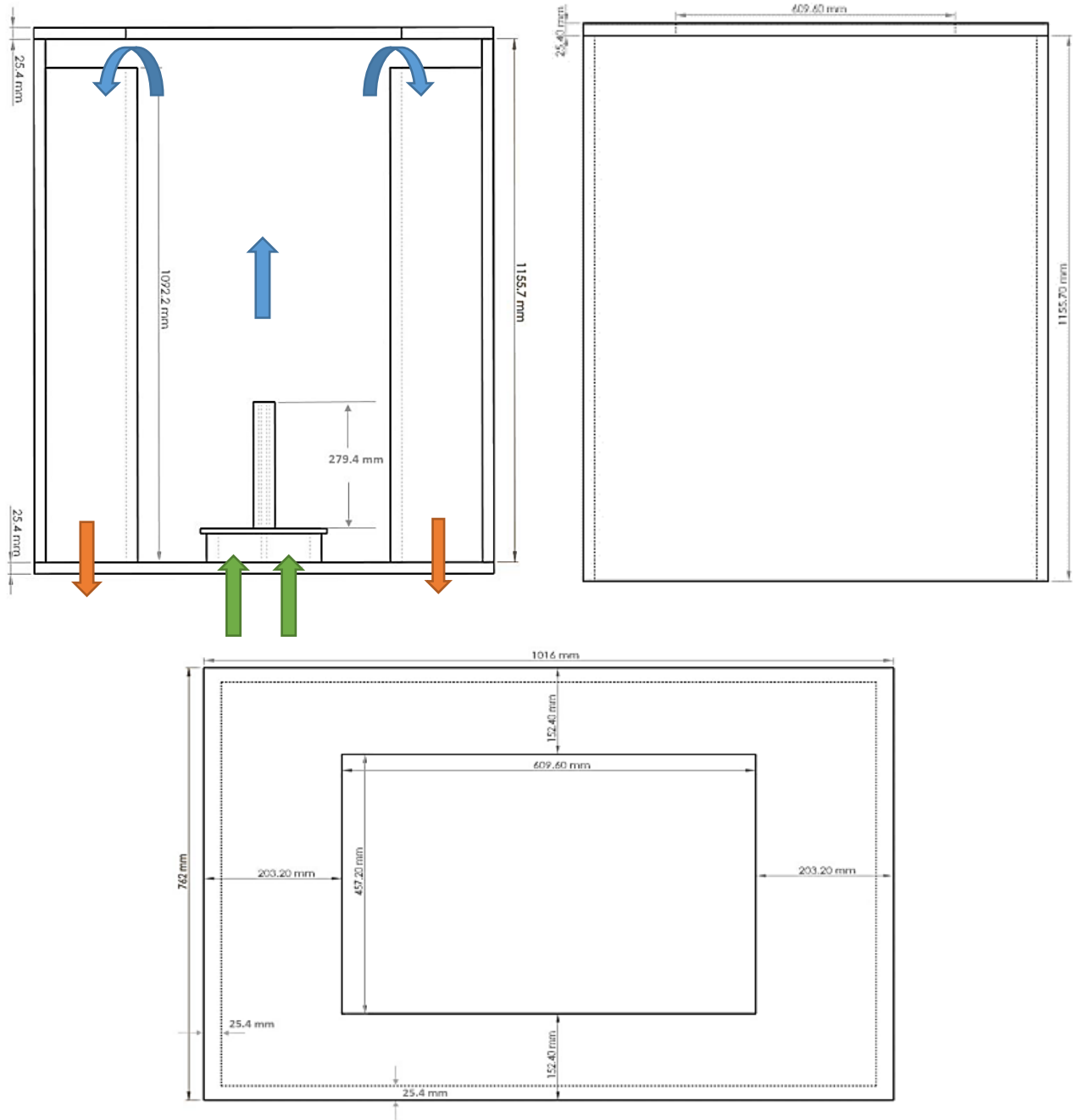


Fig. 2.5 Water tank views and flow path: inlet (green) and outlet (orange)

The nozzle test section is designed to operate at a jet Reynolds number equal to $Re = 9100$, based on the average discharge velocity for each rectangular nozzle, which is 0.75 m/s . The water flow is driven by two $\frac{1}{2}$ horsepower pumps, (Manufacturer: WEG), and its flow rate is controlled by two valves, and monitored with two GPI TM100 flow meters with an accuracy of 97% and repeatability of 95%. The facility is capable to operate as a single or dual jet, in the dual operation mode, velocities and temperatures can operate independently, thanks to the two independently controlled separate pumps, flow meters and pump suction reservoir.

The rectangular nozzle have a width of $a = 5.8 \text{ mm}$ and length of 87.6 mm , the spacing between the centerline of the two nozzles is of $s = 17.8 \text{ mm}$. The height of the nozzles slot is 279.4 mm , long enough to ensure a fully developed turbulent velocity profile in each nozzle rectangular section.

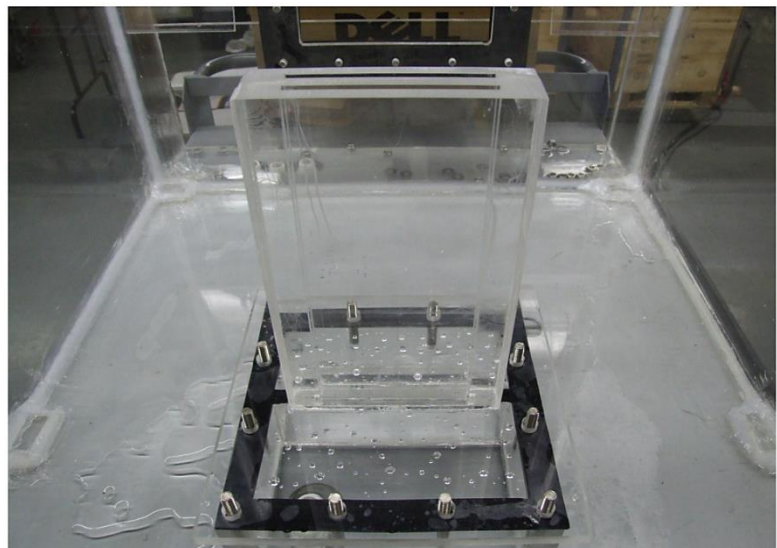
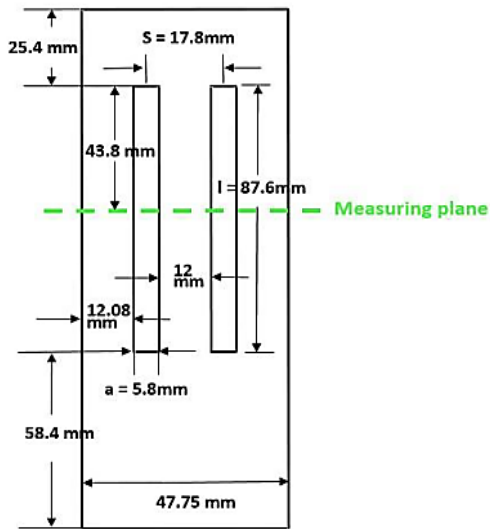
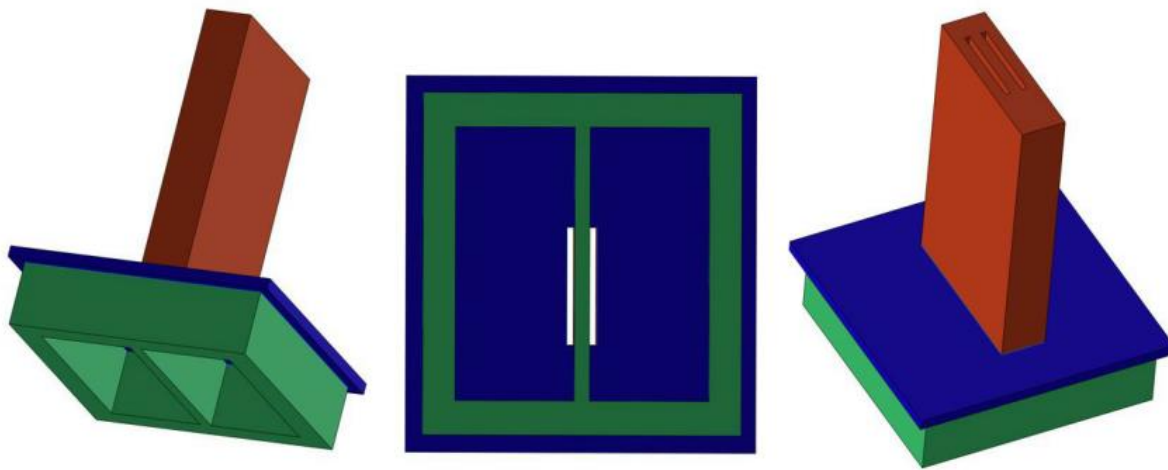


Fig. 2.6 Jet inlet slot assembly: particulars

The nozzles slot is placed at the center of the tank, and the jets can develop freely without being affected by the presence of the lateral walls. For this work, the two jets have the same discharge velocity and are at room temperature.

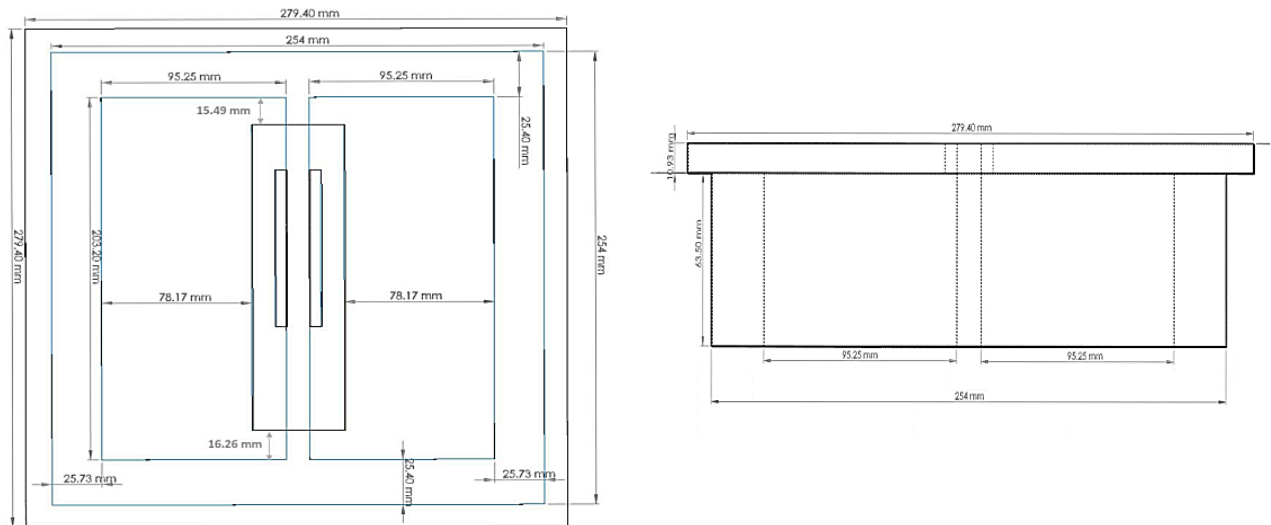


Fig. 2.7 Jet inlet slot assembly: dimensions

The flow enters the tank from the bottom and, before entering in the two nozzles slot, it passes through two separated rectangular stagnation boxes, whose function is to dump every kind of undesired fluctuation in the flow. The two jets then enter the tank. The outflow of the free water level of the tank is possible thanks to two separate outflow rectangular plates where water is recirculated in both of the two independent water loops.

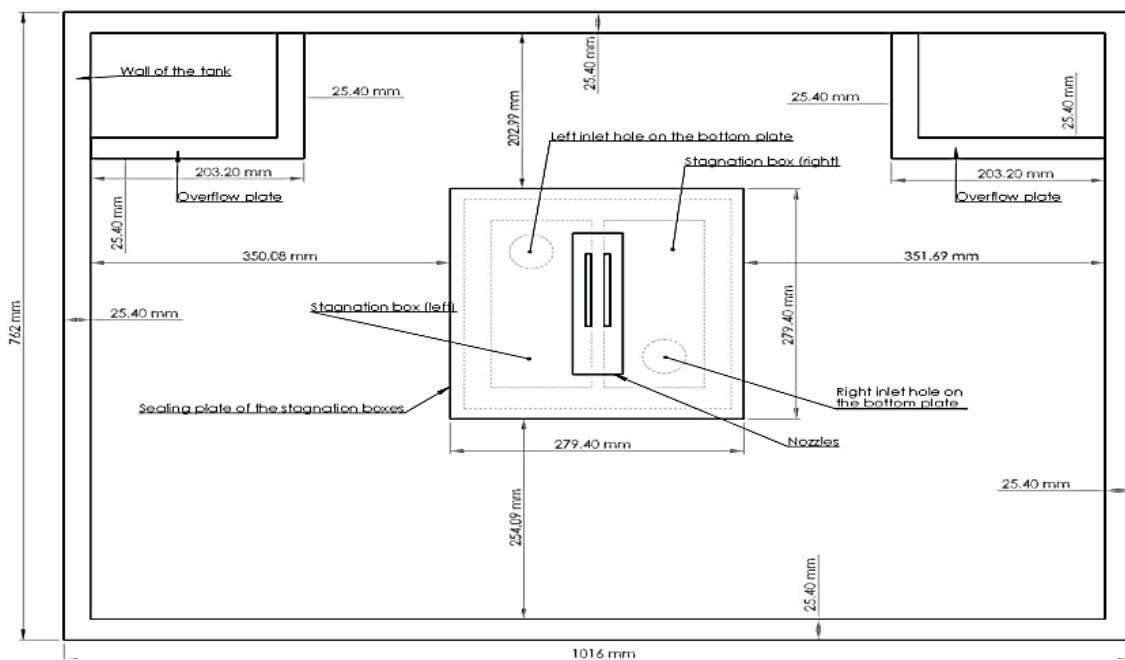


Fig. 2.8 Tank top view: dimensions

Experimental data

The available experimental data on the velocity field, are from a set of Particle Image Velocimetry (PIV) measurements [2].

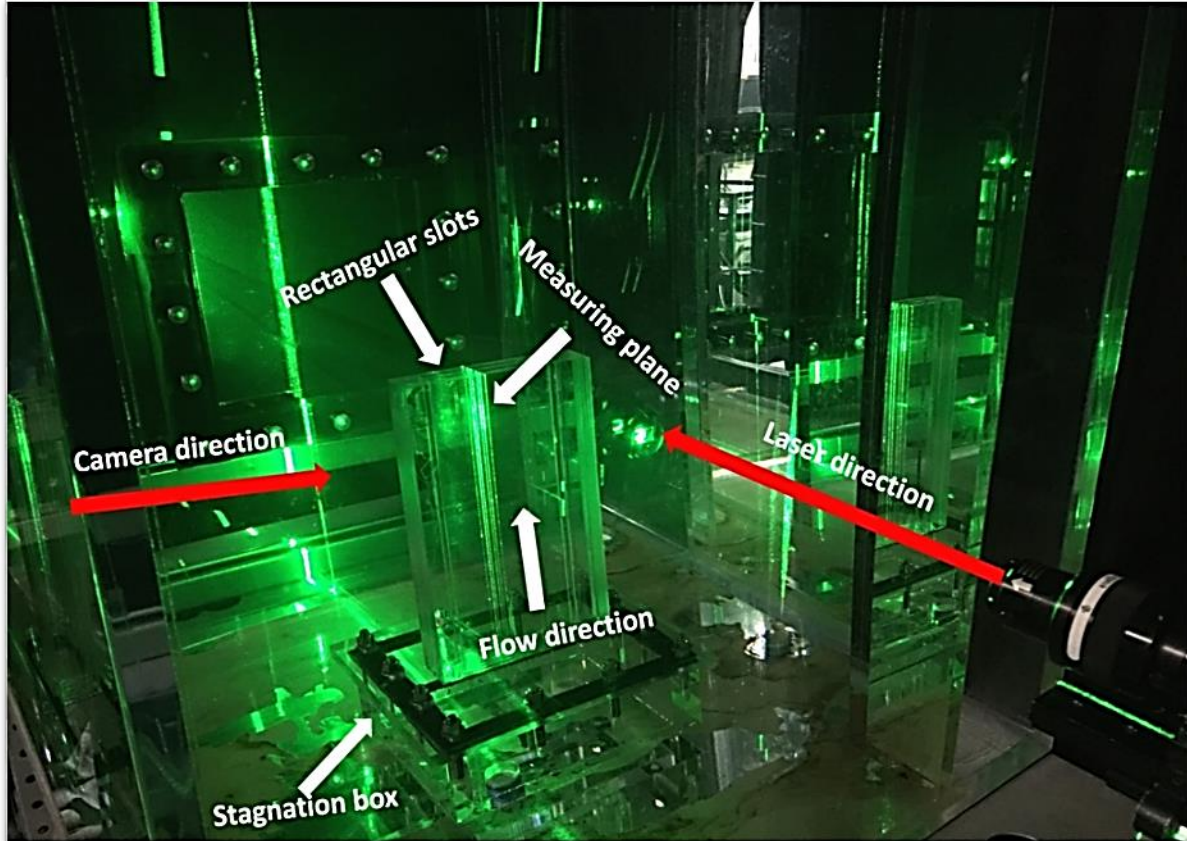


Fig. 2.9 PIV measurements: setup

The PIV system used to measure the velocity field consisted of an high-power Nd:YAG dual laser head (GX3 V190 B/W) equipped with a 1.3 Mpixel sensor. The maximum laser energy was 100 mJ/pulse , and the maximum shooting frequency can be varied between 15, 500 and 1000 Hz, the experimental data used for this work, are at 15 Hz frequency and a wavelength of 572 nm (Green). The maximum rate of the camera was 198000 fps and the maximum resolution 1280x1024 pixels. The high speed camera and the laser were synchronized by high accuracy pulse generator. The time period between each pair of images was 0.5ms.

The high speed camera is sitting on a 3D traversing system with an accuracy of 0.01 mm so that the camera can be moved accurately to investigate different regions of the jet. The seeding particles used in the experiments are hollow glasses/polyamide hollow spheres, with a refractive index of 1.5. The density of the seeding particles varies from 1.05 to 1.15 g/cm^3 . The Stokes number, which is an indicator of the tracer fidelity was, 0.0009, which means that particles can follow very well the flow field, without influence.

The particles were injected into the system from two water reservoirs under the water tank, and the system ran long enough, before the measurements were taken, to minimize any unstable effect. Each measurement generates 812 pairs of images. The images were then analyzed using an open source code PIVlab.

The measurements were repeated three times to evaluate the experimental uncertainties, each measurement were taken at different times and independently, and for each measurement the facility was cleaned and resampled to ensure the independence of each measurement.

The results from the three independent measurement were then ensemble-averaged to evaluate the mean streamwise velocity component V_y , and the mean lateral velocity V_x , and other turbulence quantities such as turbulent intensities and the root mean squares of the velocity components, $V_{y,rms}$, $V_{x,rms}$ and Reynold stresses.

The difference between PIV and LDA measurement is that, in the former case, all the fluid field can be captured at the same time.

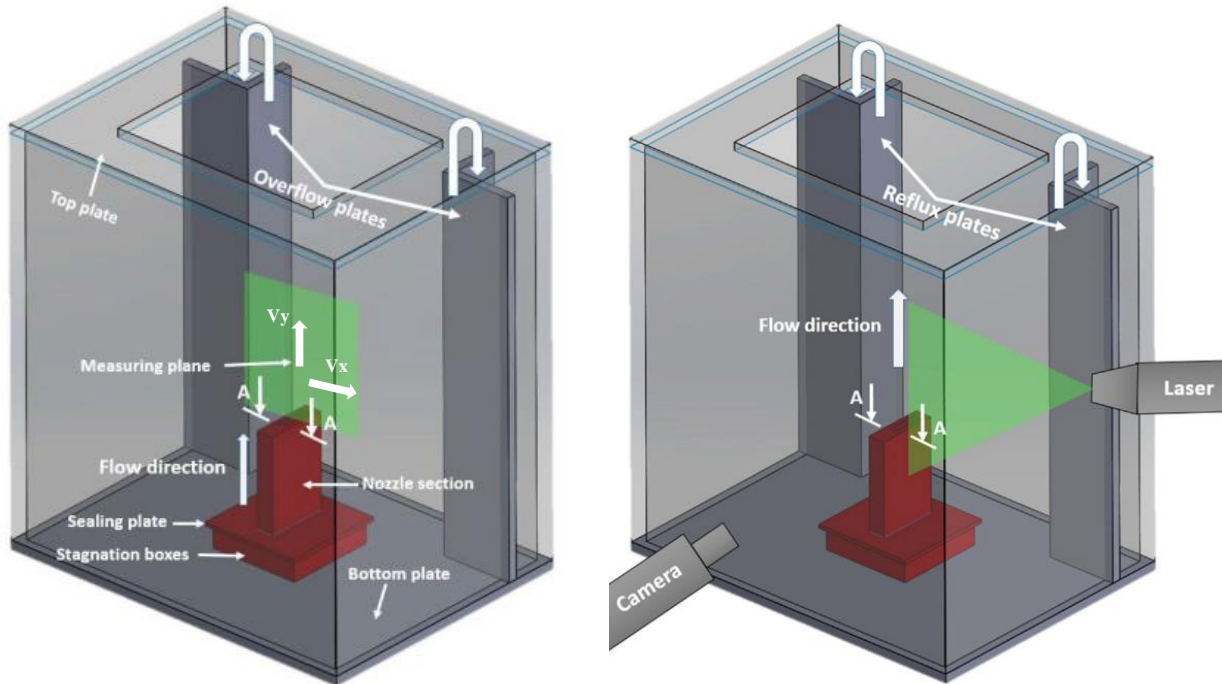


Fig. 2.10 PIV measurements: measuring plane and PIV setup

Mean Velocity

The mean velocities profiles V_y, V_x , were calculated by time averaging over 800 frames of pairs of images, then the three averaged mean velocities were ensemble averaged to obtain the final mean values. The location of merging point was found to be at $y/a = 3.45$ (a is the nozzle width). The errors in the measurement was less than 3% except for those points of velocities close to zero.

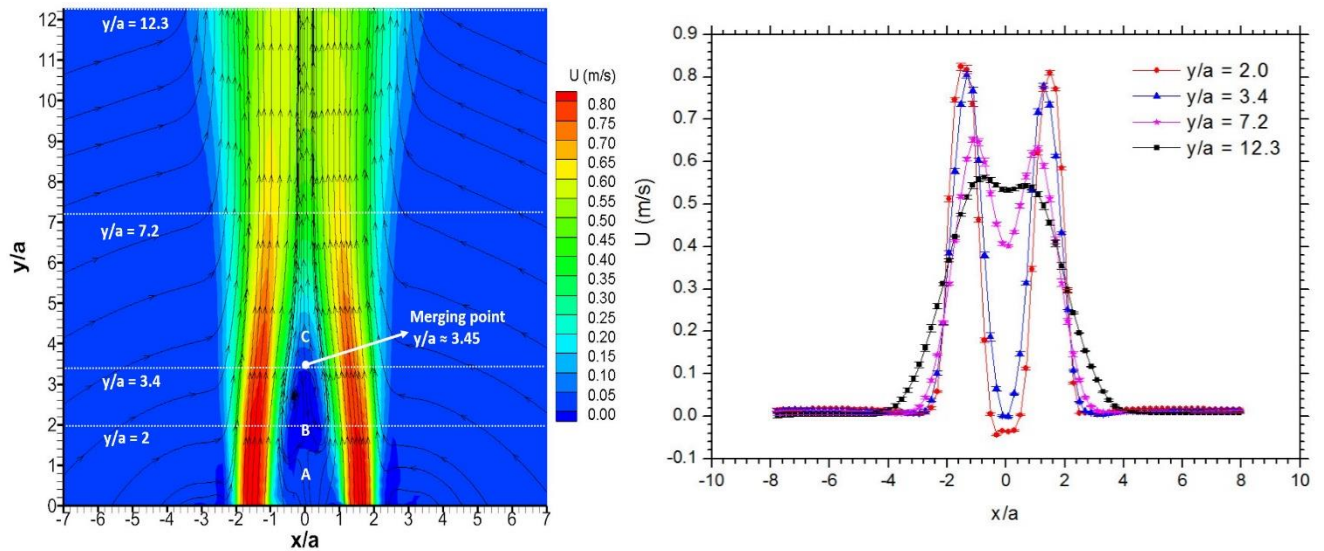


Fig. 2.11 V_y time average velocity profiles

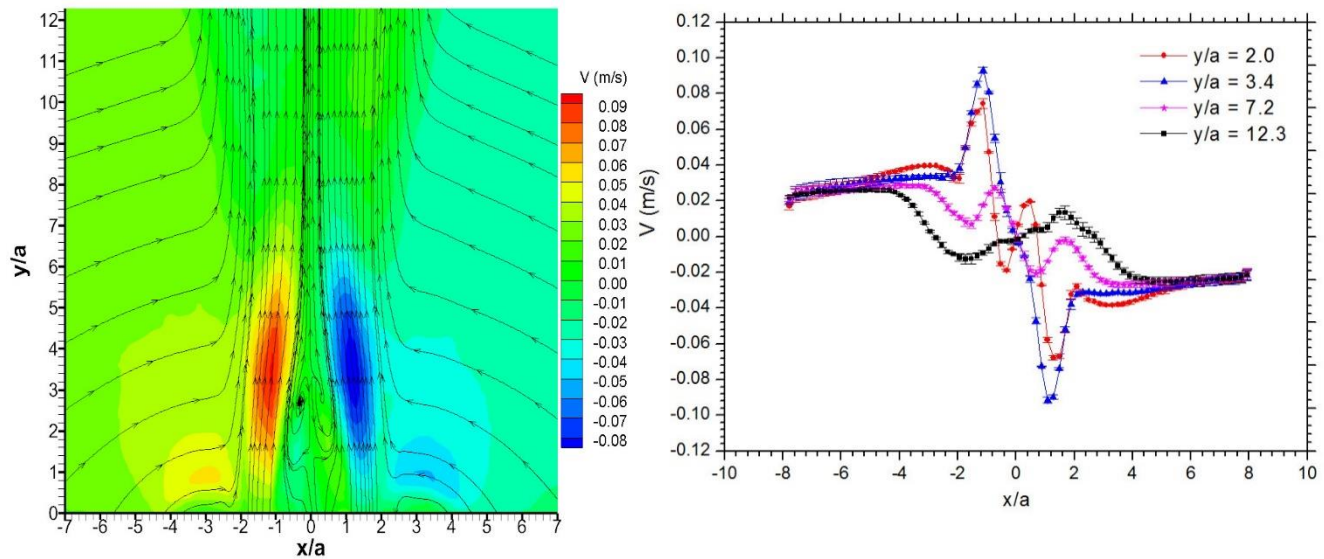


Fig. 2.12 V_x time average velocity profiles

In the figure above are presented the time average, experimental velocity profiles of the velocity components in the streamwise direction, V_y and in the horizontal direction V_x . For the V_y velocity profile it can be observed the typical double peak profile, in the region close to the outlet of the jets, and as far as the fluid develops downstream, the velocity profile tends to the single peak profile of a single jet. The same happens to the V_x component.

Turbulence intensity

The turbulence intensity can be evaluated by measuring the root mean squares of the velocities fluctuations in time.

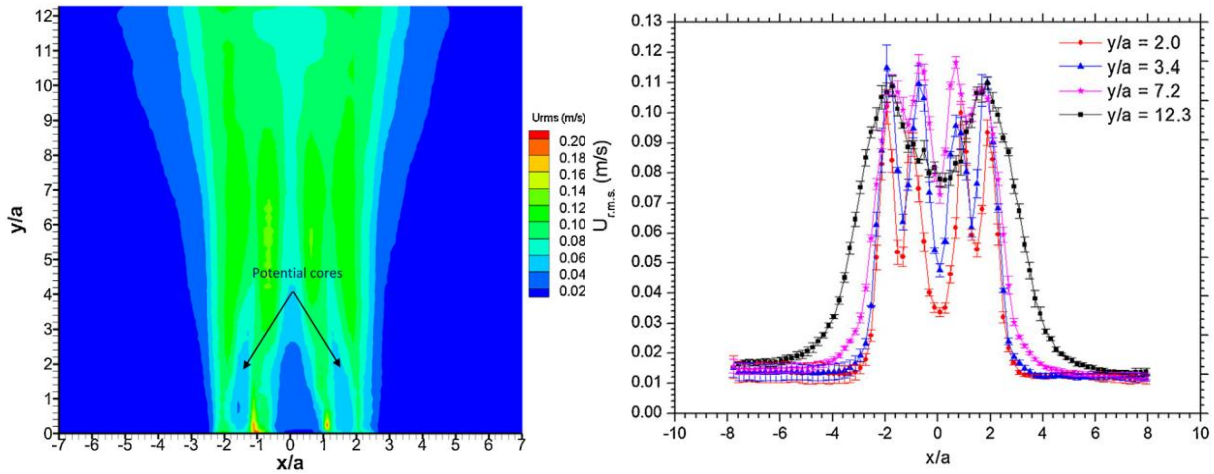


Fig. 2.13 V_y -R.M.S. Profiles

There were found that, as expected, the turbulence intensity in the region close to the inlet nozzle, the potential core region, the turbulence intensity was close to zero.

Due to shear forces at the edges of the jets, the turbulence intensity is larger in this region. It was also found that the turbulence intensity in the recirculation zone is low, although the flow behavior in this zone is characterized by reverse flow.

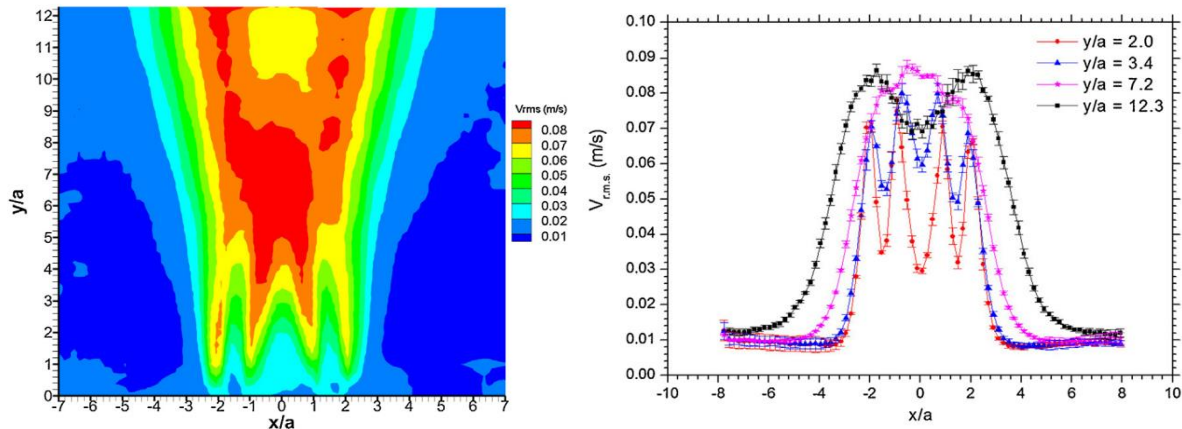


Fig. 2.14 V_x -R.M.S. Profiles

The zone where the turbulence intensity is high is in the merging zone, after the merging point, implying that the momentum exchange happened mainly in this region.

Reynolds stresses

Reynolds stresses comes from the application of the time average operator to the Navier-Stokes equations, to account for the turbulent fluctuations of the flow field, and is a measure of turbulent, non advective, momentum flux in the flow due to turbulence. For this case the component of the Reynolds stress tensor on the measuring plane have been calculated. The turbulent momentum transfer is mainly localized in proximity of the edges of the jets, due to the shear stresses between the jet flow and the surrounding liquid.

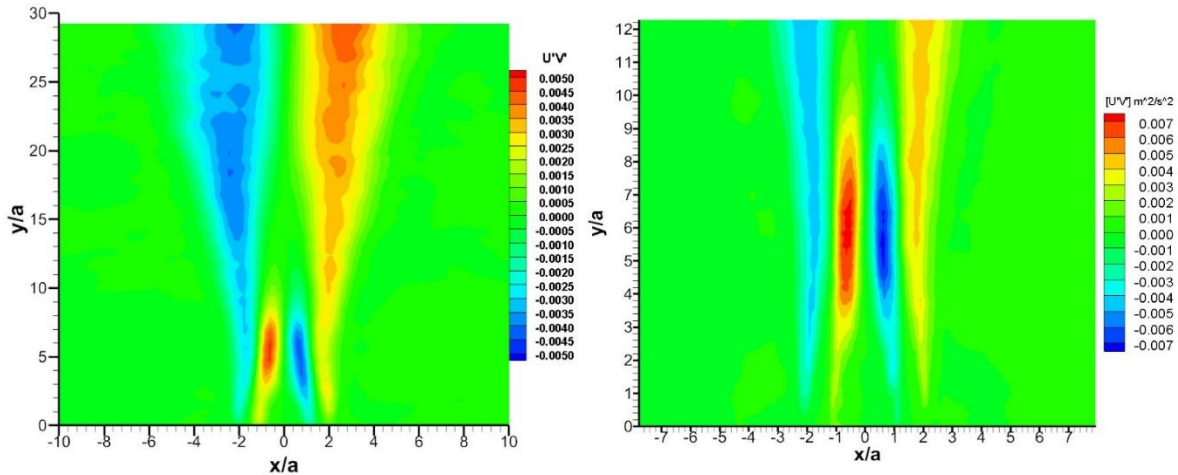


Fig. 2.15 Reynolds Stresses

Validation experimental data

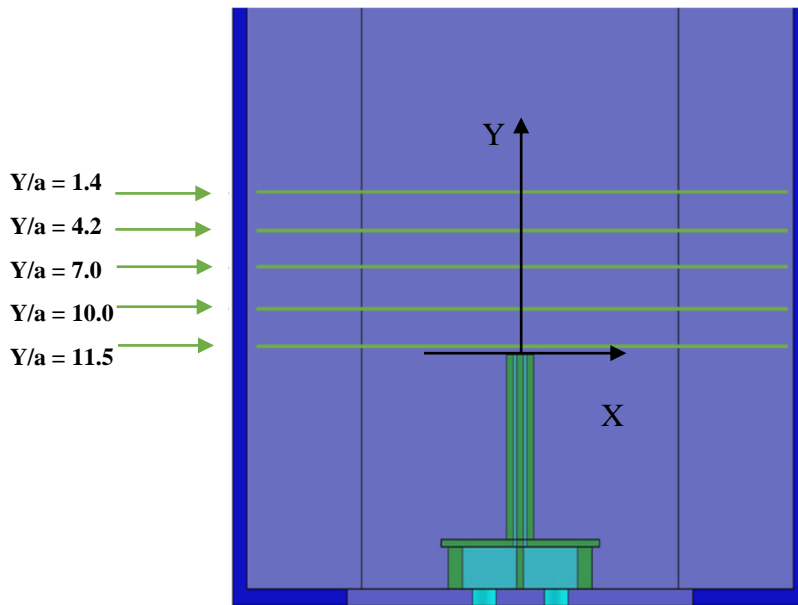


Fig. 2.16 Measurements Heights

The available data for validation purposes are:

- V_y velocity profile
- V_x velocity profiles
- Reynolds Stress tensor components
- Positions of the Merging Point and Converging Point along the centerline jets axis.

The experimental profiles, from PIV measurements at 15 Hz, are measured at 5 different heights, starting from the nozzle outlet. The heights are expressed in an dimensionless form, the scale factor is the rectangular nozzle width $a = 5.8 \text{ mm}$.

In addition there are present the V_x, V_y profiles at the nozzles outlets at $Y = 0$, this profiles will then be used as a boundary condition, as it will be explained in a later section, to perform a sensitivity analysis, of the computational results, on the boundary conditions.

Each set of this experimental data includes:

- The ensemble time average values, from three independent measurements, of the profiles.
- The measurements standard deviations
- The root mean square of each quantity

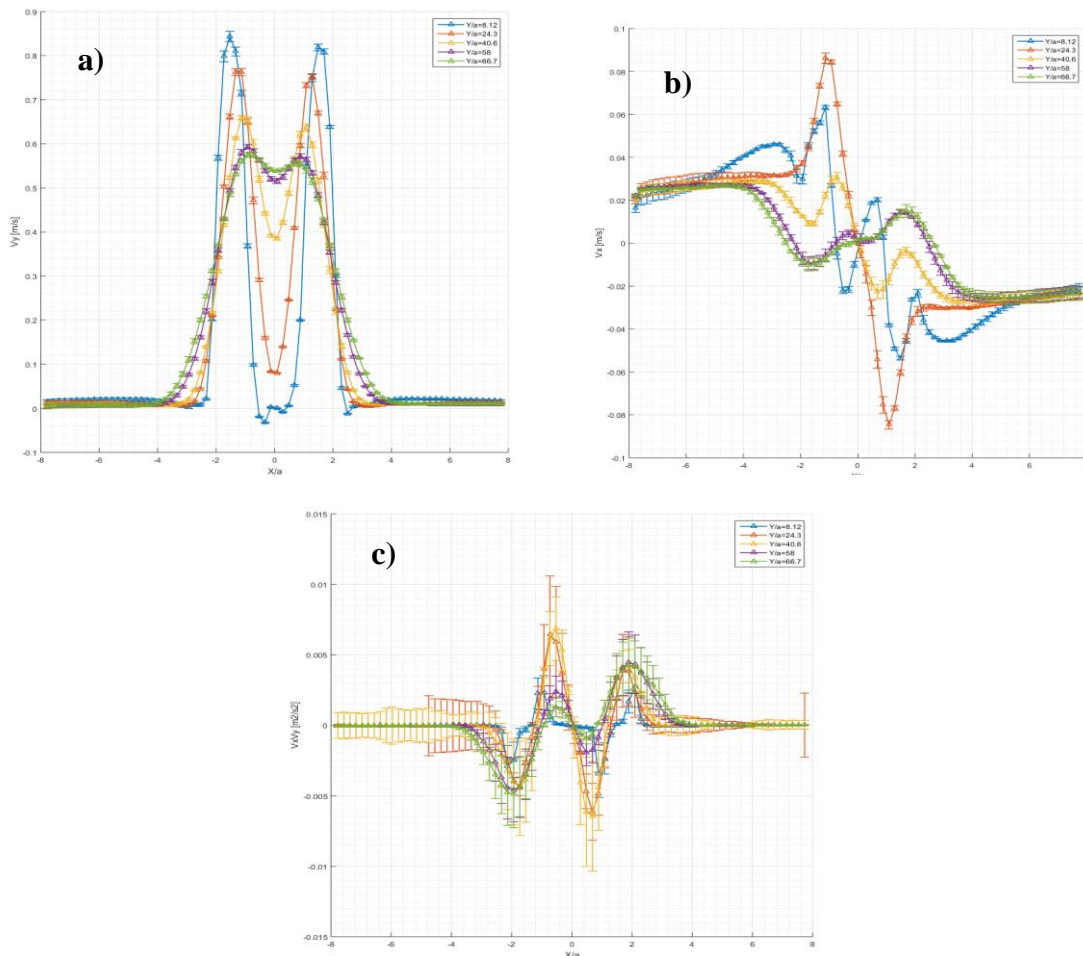


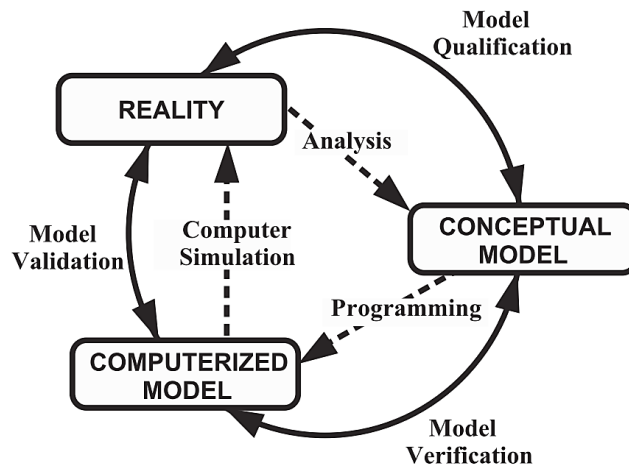
Fig. 2.17 Experimental Data: a) V_y b) V_x c) R_{ss}

3 Verification and Validation

One of the main concerns about computational simulation analysis is how to critically assess the credibility and confidence of simulation results. Verification and Validation (V&V) activities are the primary means for building and quantifying this confidence. In the literature there are a large number of definitions for Verification and Validation, we can start this discussion by reporting the Roache definition of V&V [5]:

Verification is a purely mathematical exercise that intends to show that we are solving the equations right, and Validation is an activity that intends to show that we are solving the right equations.

To better understand what is the meaning of this sentence, it is better to analyze the following figure, developed by the Society of Computer Simulation (SCS) and it is referred to as the *Sargent Circle* [6], which graphically summarize the V&V activity.



3.1 Sargent Circle

This diagram provides an illustration of the modeling and simulation activities (solid lines) and the assessment activities (dashed lines).

The **reality** block, represents the physical system for which experimental data is being obtained, and represents the validation database, which generally includes a hierarchy of experiments, starting from simple problems and ending, when possible to a full representation of the physical system of interests.

The figure shows also two kinds of models related with the reality block. The **conceptual (or mathematical model)**, which takes into account all the information, model assumptions, and mathematical equations that describes the physical (real) system of interests, usually it takes the form of a system of partial differential equations (PDEs), constitutive relations, geometry, initial and boundary conditions, needed to describe mathematically the relevant physics. The process of

assessment of the adequacy of a mathematical model to provide an acceptable, mathematical representation, of the physical system is defined as **model qualification procedure** or simply modeling. Since we are focusing on V&V, we will not address the model qualification issues, because the starting point of the V&V process starts right after this procedure, in other words the V&V activity starts when the reality of interest experimental data and the mathematical model are already given. The other model present is the **Computerized (or discretized model)**, and it represent the implementation of the mathematical model, in form of numerical discretization and solution algorithms, in a code. The computer model comprises the computer program (code), the discretized domain, mathematical assumptions and code inputs.

The verification and validation activities are the activities associated with the three blocks showed: **reality, mathematical model and computerized model.**

Verification is then the activity related with the mathematical model and the discretized model. The verification activity is usually a two steps process, the code verification and the subsequent solution verification. The first focuses on the identification and removal of errors in the code, the second try to estimate the numerical error introduced in the process of translating the mathematical problem from the continuum of space and time into a discrete representation of them [7].

Validation is the final phase of the V&V activity, whose scope is to quantify the accuracy of the mathematical model through the comparison between the experimental data and the simulation solution from the discretized model [7].

It is clear from the description given above that the Verification and Validation activities are strictly connected between each other but, at the same time are completely separate activities, since verification is in the domain of mathematics and validation is in the domain of physics. The connection between the two activities is of fundamental importance, since the evaluation of the accuracy between the mathematical model and reality can be done only by comparing the simulation results from the discretized representation of the mathematical model and the reality. That is the reason why it is extremely important an accurate verification activity before the validation procedure, in fact, the validation activity does not concern the model itself, but its discretized representation.

Validation depends on discretized solution accuracy as well as on experimental measurements accuracy. For example, computational errors that arises from failure to adequately converge a calculation, contributes to increase the discrepancy in the agreement between the calculation solution and the results from the experiments with which the discretized solution is compared when the validation is performed. If severe enough, this computational error could dominate this discrepancy and the simulation solution is not anymore a good representation of the mathematical model solution and the validation would be at this point worthless.

Verification assessment

Verification provides a framework for the quantification of the numerical approximation error between the discretized solution and its relative mathematical model, generally identified as a system of partial differential equations or integral equations, boundary conditions, and any kind of auxiliary algebraic equation, since the exact solution of mathematical model are extremely rare.

Verification is composed of two distinct activities: Code verification and Solution verification.

Code verification

The scope of code verification is to verify that a given code solves correctly the equations of the discretized model without mistakes or “bugs” and it is a faithful representation of the mathematical model without inconsistencies in the chosen numerical algorithm. In order to do that, the direct evaluation of the numerical error ϵ_{num} is needed, and the exact solutions of the mathematical problem ϕ_{model} and the discretized model $\phi_{discrete}$ should be available.

$$\epsilon_{num} = \phi_{discrete} - \phi_{model} \quad (1)$$

There are only a limited number of cases for which direct solutions of the PDE mathematical models are available, in the other cases, this solution cannot be evaluated (eg. Complex turbulent flows) and, in order to perform a code verification activity, the most widely used technique to overcome this problem is the use, for example, of the Method of Manufactured Solution (MMS) [7].

The typical procedures for code verification are:

- *Code to code comparisons*
- *Discretization error quantification*
- *Convergence and order of accuracy test*

Code to code comparisons approach compares two solutions from two different codes. This can be done when the two codes employ the same mathematical model and one of the two codes have been already verified with some acceptable type of code verification.

Discretization error evaluation can be used when the exact solution of the mathematical model is known, this test involves the quantitative assessment of the discretization error, the difference between the exact solution and the code solution. The main drawback is that this approach requires a subjective judgement of whether or not the error is reasonably small.

The convergence and the order of accuracy tests are foremost the most rigorous code verification procedures. The first part, convergence test, involves the study of the discretization error as the spatial and temporal increments are refined and, also in this case, the exact solution of the mathematical problem should be known. The convergence test should be coupled with the order

of accuracy test, which examines the order of convergence of the numerical solution for a given solution algorithm and discretization method, and whether or not it matches with the order of convergence of the numerical model (discretized model), in other words it ascertain that the discretization error is reduced at the theoretical rate order of convergence as the mesh/time step are refined.

The order of accuracy test coupled with the convergence test is the most rigorous type of code verification, it is extremely sensitive to small mistakes in the code and deficiencies in the numerical algorithm. As it will be shown in the next section, the order of accuracy test and the convergence test are powerful tools used also for the evaluation of the discretization error, in the solution verification process where, the exact solution of the mathematical problem is not known.

Solution verification

Solution Verification answers the question of whether the discretized solution of mathematical model is sufficiently accurate for its intended use. It includes the accuracy not only of the simulation for the case of interest, but also the accuracy of the inputs of the code and any post processing of the code results. It relies also on the use of consistent and convergent numerical algorithms as well as mistake free codes. If code validation studies have not been conducted, the solution verification procedures are useless since there is no guarantee that the simulation result will converge to the exact solution of the mathematical problem. The main focus of solution verification is the estimation of the numerical error that occur when a mathematical model is discretized and solved on a computer. While strategies in conducting code and solution verification are very similar, the difference is that in the code verification case, as we already said, the exact solution of the mathematical model is known a priori and then the numerical error can be evaluated, in the solution verification case the exact solution of the mathematical model is unknown and only an estimation of the numerical error can be calculated.

Numerical errors occur in every scientific computing simulation, and thus they must be estimated in order to have a certain degree of confidence about the mathematical accuracy of the solution. When numerical errors are found to be large, then they should be accounted for in the total uncertainty due to modelling and simulation predictions or be reduced by refining the spatial and temporal domain. Numerical errors can be classified in different groups:

- Round-off errors
- Iterative errors
- Discretization errors

Round off errors come from the use of finite arithmetic on digital computers. Repeated arithmetic operations will degrade the accuracy of a simulation if this error is large enough, but they can be reduced by using more significant digits in the computation. In the majority of the cases the round-off error can be negligible, compared to iteration and discretization errors. In this work the double precision CFX executables have been employed, where the floating point format is 64-bit words, for more accurate mathematical operations.

Iteration errors are defined as the difference between the iterative and exact solution of the algebraic equation system, in the case an iterative or relaxation method is used for the solution of the discretized equation system. The iteration process for solving a set of algebraic equations seeks to find a series of approximate solutions by starting with an initial guess of the solution itself. Starting from the original set of the algebraic problem expressed in a matrix form:

$$A \phi = b \quad (2)$$

where A is the matrix of the coefficients, ϕ is the unknown solution and b is the vector of the known terms.

The iteration problem can be recast and expressed in the form

$$\phi^{n+1} = H \phi^n + c \quad (3)$$

where ϕ^{n+1} is the solution at the (n+1)-th iteration, H is the iteration matrix, ϕ^n is the solution from the last iteration, and c is the vector of known coefficients.

The difference between the approximate solution at the n-th iteration ϕ^n and the exact solution ϕ_a of the algebraic system is the iteration error.

$$\epsilon^n = \phi_a - \phi^n \quad (4)$$

If we substitute the solution of the system at the n-th iteration in the original form of the matrix problem, we can define the iteration residual ρ^n expressed as:

$$A \phi^n - b = \rho^n \quad (5)$$

If we subtract the two equations, we can have a relation between the iteration error and the iteration residual at the n-th iteration:

$$A \epsilon^n = \rho^n \quad (6)$$

Since the exact solution of the algebraic system ϕ_a is not known, the best way to estimate the iteration error is the evaluation of the residuals of the numerical scheme, since they are related.

A number of studies have shown that the iterative residual reduction follows the iterative error reduction for a wide range of linear and non-linear problems, in particular the rate of the iterative error and residuals reduction is almost the same [8]. This supports the common practice of assessing iterative convergence by examining the norm of the iterative residuals. In this work the CFX normalized L_2 norm of the residuals have been monitored, and their range was reasonably small enough to not include the iterative error as a source of numerical error.

It has been demonstrated that as a general rule of thumb if the round-off errors and iteration errors are two orders of magnitude smaller than the discretization error estimation the only non-negligible source of numerical error is the discretization error [9,10]

Discretization error

Since it has been assumed that the discretization error is the main source of the numerical error we will give a detailed description of the Roache's Grid Convergence Index (GCI) [11] discretization error estimation procedure, which has been used in this work.

The discretization error is the error that comes from the translation of the original mathematical model, governed by partial differential equations or integral equations and their associated boundary conditions, into a discretized set of them in space and time.

The discretization error can formally be defined as the difference between the exact solution of the Mathematical (PDE) model $\tilde{\phi}$ and the solution of the algebraic problem ϕ_h :

$$\epsilon_h = \phi_h - \tilde{\phi} \quad (7)$$

Discretization error is the most difficult type of numerical error source to estimate reliably and is usually the largest of the different numerical error sources. The main problem is that the exact solution of the mathematical model is not known and there is only the possibility to estimate the discretization error.

The most widely used approach to estimate the discretization error is the Grid Convergence Index method and it is based on the Richardson Extrapolation concept:

If one knows the formal rate of convergence of the discretized numerical scheme p , and if two sets of discretized solutions are available on different refined meshes, with a constant refinement factor $r = h_{\text{fine}}/h_{\text{coarse}}$ (h is the node spacing), then one can use this set of information for the discretization error estimation.

Recalling the definition of discretization error, for a local or a global quantity ϕ , on a mesh h , the idea is to expand in a Taylor series the numerical solution ϕ_h around the exact solution $\tilde{\phi}$, and in the case of p th-order accurate scheme we have:

$$\phi_h = \tilde{\phi} + \frac{\partial^p \tilde{\phi}}{\partial h^p} \frac{h^p}{p!} + \frac{\partial^{p+1} \tilde{\phi}}{\partial h^{p+1}} \frac{h^{p+1}}{(p+1)!} + \dots \quad (8)$$

This can be recast in a simple form

$$\phi_h = \tilde{\phi} + g_p h^p + g_{p+1} h^{p+1} + g_{p+2} h^{p+2} + g_{p+3} h^{p+3} \dots \quad (9)$$

Now we can express the discretization error in a Taylor series expansion:

$$\epsilon_h = \phi_h - \tilde{\phi} = g_p h^p + g_{p+1} h^{p+1} + g_{p+3} h^{p+3} + \dots \quad (10)$$

If two meshes are refined with a refinement factor $r = h_{fine}/h_{coarse} > 1$ and we have two solutions on the two refined meshes h_{fine} and $h_{coarse} = r h_{fine}$, choosing $h_{fine} = h$, the discretization error equations on the two meshes can be expressed in the form:

$$\phi_h = \tilde{\phi} + g_p h^p + g_{p+1} h^{p+1} + o(h^{p+2}) \quad (11)$$

$$\phi_{rh} = \tilde{\phi} + g_p (rh)^p + g_{p+1} (rh)^{p+1} + o(h^{p+2}) \quad (12)$$

These equations can be used to eliminate the g_p coefficient and solve for $\tilde{\phi}$ to give

$$\tilde{\phi} = \phi_h + \frac{\phi_h - \phi_{rh}}{r^p - 1} + g_{p+1} h^{p+1} \frac{r^p (r - 1)}{r^p - 1} + o(h^{p+2}) \quad (13)$$

Combining terms of order h^{p+1} and higher with the exact solution $\tilde{\phi}$

$$\bar{\phi} = \tilde{\phi} - g_{p+1}h^{p+1} \frac{r^p(r-1)}{r^p-1} + o(h^{p+2}) \quad (14)$$

Substituting this expression into the previous one, results in the generalized Richardson extrapolation estimate $\bar{\phi}$

$$\bar{\phi} = \phi_h + \frac{\phi_h - \phi_{rh}}{r^p - 1} \quad (15)$$

The idea then is to estimate the exact solution with the solution of the discretized model on the finest mesh. This estimate is generally (p+1)-nth order accurate estimate of the exact solution of the mathematical model $\tilde{\phi}$, the accuracy is higher than the underlying numerical scheme, supposed to be p. This estimate will converge then faster than numerical solution itself as mesh is refined. From the estimation of the exact solution $\bar{\phi}$ we can estimate the discretization error

$$\epsilon_h = \bar{\phi} - \phi_h = \frac{\phi_h - \phi_{rh}}{r^p - 1} \quad (16)$$

The most important assumption for the Richardson extrapolation is that the two discretized solutions must be in the asymptotic range. When mesh refinement is employed, then the asymptotic range is defined as:

the sequence of systematically refined meshes over which the discretization error reduces at the formal order of accuracy p of the discretization scheme.

Examining the discretization error expansion for a pth-order accurate scheme

$$\epsilon_h = \phi_h - \tilde{\phi} = g_p h^p + g_{p+1} h^{p+1} + g_{p+3} h^{p+3} + \dots \quad (17)$$

the asymptotic range is achieved when h is sufficiently small that the h^p term is much larger than any of the higher-order terms. Due to possible differences in the signs for the higher-order terms, the behavior of the discretization error outside of the asymptotic range is unpredictable. Demonstrating that the asymptotic range has been reached using systematic mesh refinement is achieved by evaluating the observed order of accuracy \hat{p} .

The observed order of accuracy is the measure that is used to assess the confidence in a discretization error estimate. When the observed order of accuracy is shown to match the formal order, then one can have a high degree of confidence that the error estimate is reliable.

In order to calculate the observed order of accuracy it is necessary to have at least three sets of solutions on three refined meshes. In case of constant grid refinement r and a p -th order accurate scheme, with a numerical solution on the finest mesh h_1 , medium mesh h_2 and coarse mesh h_3 , we can write

$$h_1 = h, h_2 = r h, h_3 = r^2 h \quad (18)$$

Using the discretization error expansion, we can have for the three solutions

$$\phi_1 = \tilde{\phi} + g_p h^p + g_{p+1} h^{p+1} + o(h^{p+2}) \quad (19)$$

$$\phi_2 = \tilde{\phi} + g_p (r h)^p + g_{p+1} (r h)^{p+1} + o(h^{p+2}) \quad (20)$$

$$\phi_3 = \tilde{\phi} + g_p (r^2 h)^p + g_{p+1} (r^2 h)^{p+1} + o(h^{p+2}) \quad (21)$$

Neglecting terms of order h^{p+1} and higher allows us to recast these three equations in terms of a locally-observed order of accuracy \hat{p} :

$$\phi_1 = \tilde{\phi} + g_p h^{\hat{p}} \quad (22)$$

$$\phi_2 = \tilde{\phi} + g_p (r h)^{\hat{p}} \quad (23)$$

$$\phi_3 = \tilde{\phi} + g_p (r^2 h)^{\hat{p}} \quad (24)$$

which will only match the formal order of accuracy if the higher order terms are small.

Subtracting ϕ_2 from ϕ_3 and ϕ_1 from ϕ_2 gives

$$\phi_3 - \phi_2 = g_p r^{\hat{p}} h^{\hat{p}} (r^{\hat{p}} - 1) \quad (25)$$

$$\phi_2 - \phi_1 = g_p h^{\hat{p}} (r^{\hat{p}} - 1) \quad (26)$$

Which gives

$$r^{\hat{p}} = \frac{\phi_3 - \phi_2}{\phi_2 - \phi_1} = \frac{g_p r^{\hat{p}} h^{\hat{p}} (r^{\hat{p}} - 1)}{g_p h^{\hat{p}} (r^{\hat{p}} - 1)} \quad (27)$$

Taking the natural logarithm of both sides

$$\hat{p} = \frac{\ln\left(\frac{\phi_3 - \phi_2}{\phi_2 - \phi_1}\right)}{\ln(r)} \quad (28)$$

Note that it is only when the observed order of accuracy matches the formal order of the numerical scheme that we can expect the discretization error estimate to be accurate

$$\epsilon_h = \frac{\phi_h - \phi_{rh}}{r^p - 1} \quad (29)$$

This is equivalent to saying that the solutions on all three meshes are in the asymptotic range.

In practice, when this locally observed order of accuracy is used for the extrapolation estimate, it is often limited to be in the range [7]

$$0.5 p \leq \hat{p} \leq p \quad (30)$$

since in most of the cases it is almost impossible to match the two quantities.

Allowing the observed order of accuracy to increase above the formal order can result in discretization error estimates that are not conservative (i.e., they underestimate the error). Furthermore, as \hat{p} approaches zero, the magnitude of the extrapolated estimate grows without bound.

As discussed previously, when it has been demonstrated that the solutions are in the asymptotic range, then one can have confidence that the error estimate is reliable and therefore use the error estimate to correct the solution. While the calculation of the observed order of accuracy requires

three systematically refined meshes, a fourth mesh level is recommended to confirm that the asymptotic range has indeed been reached. However, the much more common case is when the formal order does not match the observed order. In this case, the error estimate is much less reliable and should generally be converted into a numerical uncertainty. Uncertainties due to such a lack of knowledge are called epistemic uncertainties and are distinct from aleatory (or random) uncertainties. They can be reduced by providing more information, in this case, additional computations on more refined meshes.

The principal method for the evaluation of the discretization error as uncertainty, is the grid convergence index proposed by Roache 1994 [11].

Before the use of the GCI, authors reported discretization error estimates by giving the relative difference between two discrete solutions evaluated on two refined meshes

$$RDE = \frac{\phi_2 - \phi_1}{\phi_1} \quad (31)$$

This relative difference can be extremely misleading when used as an error estimate. To see why, consider the estimate of the relative discretization error (RDE) found from generalized Richardson extrapolation, which for the fine grid can be written as

$$RDE_1 = \frac{\phi_1 - \bar{\phi}}{\bar{\phi}} \quad (32)$$

Substituting the generalized Richardson extrapolation result from

$$\bar{\phi} = \phi_h + \frac{\phi_h - \phi_{rh}}{r^p - 1} \quad (33)$$

Into the above equation gives

$$RDE_1 = \frac{\phi_2 - \phi_1}{\phi_1 r^p - \phi_2} \quad (34)$$

As an example [7,11], consider two numerical solutions where some quantity of interest ϕ has fine and coarse grid values of 20 and 21, respectively, for a relative difference between solutions of 5%. For a third-order accurate scheme with refinement factor $r = 2$, the error estimate based on Richardson extrapolation from the previous equation is 0.71%. However, for a first-order accurate numerical scheme with a grid refinement factor of 1.5, the error estimate based on Richardson extrapolation is 9.1%. Thus, a 5% relative difference in the two solutions can mean very different values for the relative discretization error, depending on the order of accuracy of the scheme and the grid refinement factor.

This example illustrates the importance of accounting for the grid refinement factor r and the order of accuracy p when using Richardson extrapolation to estimate the discretization error.

The GCI is based on the often reported relative error between two discrete solutions, but it also accounts for the amount of grid refinement and the order of accuracy, it converts the error estimate into an uncertainty estimate using absolute values. The GCI for the fine numerical solution is defined as

$$GCI = \frac{F_s}{r^p - 1} \left| \frac{\phi_2 - \phi_1}{\phi_1} \right| \quad (35)$$

Where F_s is a factor of safety, usually when the observed order of convergence is not matched or it is not calculated, the factor of safety is taken as $F_s = 3$, instead when the observed order of accuracy is comparable with the formal order of accuracy it is equal to $F_s = 1.25$.

In his original paper [11], Roache proposed the value $F_s = 3$, since the idea behind the GCI is to relate the relative error RDE_1 between two discrete solutions evaluated on two refined meshes, obtained with whatever grid refinement study (p,r) to the same relative error that would be expected from a grid refinement study of the same problem using $p = 2$ and $r = 2$, grid doubling and second order accurate scheme, in fact in this case, using a factor of safety $F_s = 3$, the correspondent GCI coincides with the relative error $GCI = |RDE|$.

The GCI returns a fractional estimate of the discretization error uncertainty on the fine grid solution.

Validation

In V&V, the ultimate goal is solution validation, defined as the process of determining the degree to which a mathematical model is an accurate representation of the real world. The estimation of a range within which the simulation modelling lies is the main objective of validation.

In this section there will be presented the main definitions and procedures proposed by the ASME V&V-20 “Standard for Verification and Validation in Computational Fluid Dynamics and Heat Transfer” [12],

Let ϕ be an arbitrary variable that is both computed and experimentally measured, and Δ be the difference between the true or exact value of nature, ϕ_{nature} , and the computational result $\phi_{h,t}$, (the h,t subscripts indicate the spatial and temporal discretization that characterize the discrete solution) so that this difference can be recast and expressed as the sum of four error quantities [7]:

$$\Delta = \phi_{nature} - \phi_{h,t} = E_1 + E_2 + E_3 + E_4 \quad (36)$$

Where:

- $E_1 = (\phi_{nature} - \phi_{exp})$ represent all the errors and uncertainties due to measurement of a physical quantity referred to as *measurement error*.
- $E_2 = (\phi_{exp} - \phi_{model})$ represents all errors and uncertainties resulting from differences between the experimental measurement and the exact solution of the continuum PDEs (mathematical model) that are attempting to describe the experimental event. Note that ϕ_{model} also contains all of the initial conditions, boundary conditions and physical parameters that are needed to model the experiment. The term E_2 is usually referred to as *modeling error*.
- $E_3 = (\phi_{model} - \phi_{h,t \rightarrow 0})$, indicating with $\phi_{h,t \rightarrow 0}$ the exact solution of the discretized model, this term represent the error introduced by the exact solution of the discrete problem, and in principle, it can be argued that this term is zero from the standard principles that underlie the development of discrete algorithms for solving the PDEs. For example, it is commonly zero for strongly consistent and stable difference schemes. Trying to ensure that this term is zero is primarily the concern of the code verification phase.
- $E_4 = (\phi_{h,t \rightarrow 0} - \phi_{h,t})$ this term is the reason of solution verification assessment, since it represents the numerical error between the exact solution of the discrete problem and the actual solution.

The summation of the four terms clearly suggests that even if Δ is zero for a given comparison of computational results and experimental data, one cannot argue that all the terms are identically zero. An error or uncertainty in any of these terms can cancel the error and uncertainty in any other term, or combination of terms. To reduce the likelihood of this occurring, verification activities and solution-accuracy assessment activities are meant to provide estimates of E_3 and E_4 .

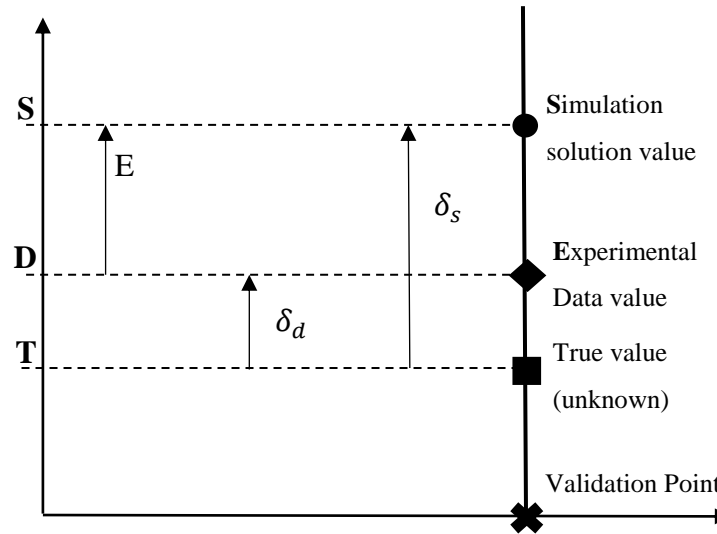
Validation activities attempt to provide an estimate of the magnitude of the experimental uncertainty, E_1 ; so that one can best estimate the magnitude of the modeling error and uncertainty, E_2 . Stated differently, validation comparisons are primarily meant to evaluate the fidelity of the continuum mathematics model of the physical process, not to find code verification errors or solution accuracy errors. This emphasizes the importance of robust verification activities before validation activities are conducted.

Validation nomenclature

Pertinent definitions for the validation metrics are the follows:

- *Error (of a measurement) δ* : result of a measurement minus the true value of the measurand, it has a particular sign and magnitude [12].
- *Uncertainty (of a measurement) U* : parameter associated with the result of a measurement that characterize the dispersion of the values that could be reasonably be attributed to the measurand [12].

The nomenclature used in the validation approach is presented in the next figure



3.2 Nomenclature

Defining the simulation solution as S , and the value determined from the experimental data as D , and the true but unknown real value as T , we define the **validation comparison error** as

$$E = S - D \quad (37)$$

The error in the solution value S , is the difference between S and T

$$\delta_s = S - T \quad (38)$$

And similarly the error from the experimental data

$$\delta_d = D - T \quad (39)$$

Using these definitions, we can express the validation comparison error as

$$E = S - D = (T + \delta_s) - (T - \delta_d) = \delta_s - \delta_d \quad (40)$$

The validation comparison error E is thus the combination of all of the errors in the simulation result and the experimental results, its sign and magnitude are known once the comparison is made.

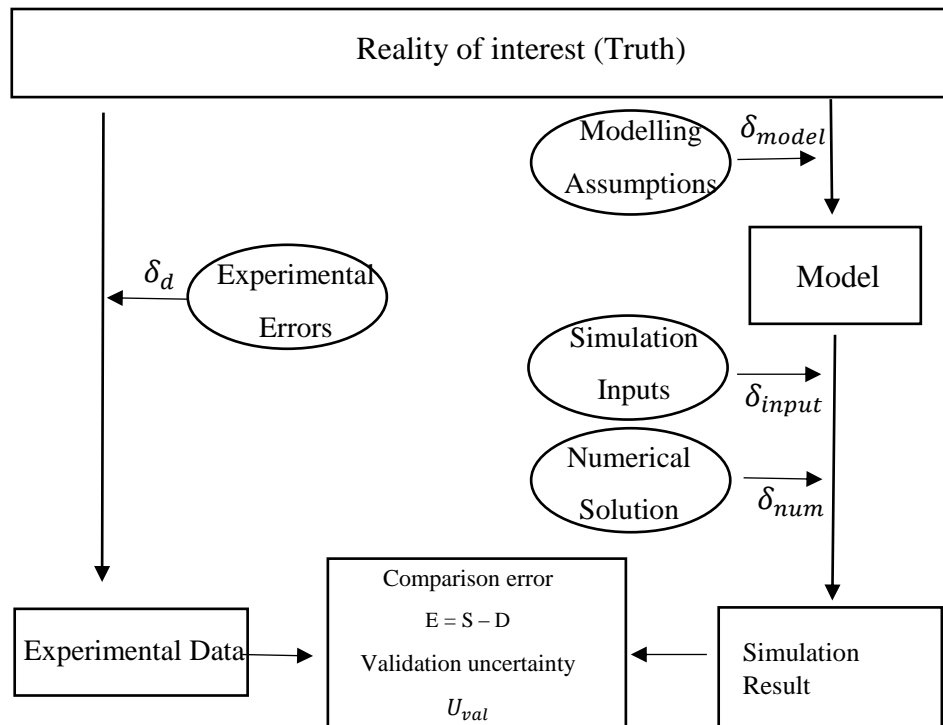
All the errors in the simulation results S , can be assigned to one of the three categories

- The errors δ_{model} due to modelling assumptions and approximations
- The errors δ_{num} due to the numerical solution of the equations
- The errors δ_{input} in the simulation result due to errors in the simulation input parameters

$$\delta_s = \delta_{model} + \delta_{num} + \delta_{input} \quad (41)$$

The comparison error then can be expressed as

$$E = \delta_{model} + \delta_{num} + \delta_{input} - \delta_d \quad (42)$$



3.3 Verification Scheme

As we have previously said the aim of the validation process is to quantify the modelling error, if we isolate the modelling error in the previous equation we have

$$\delta_{model} = E - (\delta_{num} + \delta_{input} - \delta_d) \quad (43)$$

Considering the terms on the right hand side of the equation, once S and D are determined, the sign and magnitude of E are known. However the sign and magnitudes of δ_{num} , δ_{input} , δ_d are unknown. The standard uncertainties corresponding to these errors are u_{num} , u_{input} , u_d .

Once D and S have been determined, their values differs by the same amount from the true value T. that is all the errors affecting D and S have become fossilized, and δ_{model} , δ_{num} , δ_{input} , δ_d are all systematic errors.

This means that the uncertainties to be estimated u_{num} , u_{input} , u_d are systematic standard uncertainties, and there is no distinction in the mathematical treatment between random and standard uncertainties.

A systematic error is a single realization from some parent of population of possible values from a systematic error source, and the corresponding systematic standard uncertainty, U, is the estimate of the standard deviation of that parent population.

A validation standard uncertainty, u_{val} , can be defined as an estimate of the standard deviation of the parent population of the combination of the errors ($\delta_{num} + \delta_{input} - \delta_d$). Then considering

$$E \pm u_{val} \quad (44)$$

it characterize an interval within which δ_{model} fall, or in other words

$$\delta_{model} \in [E - u_{val}, E + u_{val}] \quad (45)$$

The estimation of u_{val} is thus at the core of the methodology, and E and u_{val} are the validation metrics.

If the three errors δ_{num} , δ_{input} , δ_d are effectively independent, then

$$u_{val} = \sqrt{u_{num}^2 + u_{input}^2 + u_d^2} \quad (46)$$

In the case when the validation variable D is directly measured, then this assumption can be reasonable.

Debate on Verification and Validation has included discussion on whether errors such as the numerical error δ_{num} can be considered deterministic or stochastic, and thus how do they should be treated in uncertainty analysis.

In this work it will be used the so called strong model concept, in which the uncertainty due to the input parameters of the simulation is zero

$$u_{input} = 0 \quad (47)$$

Once the two validation metric quantities E and u_{val} have been determined, then if

- $|E| \gg u_{val}$ then probably $\delta_{model} \cong E$
- $u_{val} \geq |E|$ then $\delta_{model} \cong U_{val}$ is of the same order or less than $\delta_{num}, \delta_{input}, \delta_d$

In the first case one has information that can possibly be used to improve the model (i.e., reduce the modeling error). In the second case, however, the modeling error is within the “noise level” imposed by the numerical, input, and experimental uncertainties, and formulating model improvements is more problematic.

4 V&V Twin Jets

In this section, after a brief introduction to the ANSYS CFX code main features [13], necessary for the development of the solution verification activity, there will be presented the various CFD RANS turbulence models selected for the twin jet system, boundary conditions and the set of refined meshes, a summary of the solution verification and solution validation procedures adopted and a description of the results that will be presented in the next chapter.

Ansyes CFX CFD code

Discretization method

Ansyes CFX software uses a hybrid finite-element/finite-volume approach for the discretization of the Navier-Stokes equations defined as *Control-Volume Based Finite Element Method*. The mesh is used to construct finite volumes, which are used to conserve relevant quantities such as mass, momentum and energy. As a finite volume method, it satisfies strict global conservation by enforcing local conservation over control volumes that are constructed around each mesh vertex or node. The finite element methodology is used to describe the solution variation (needed for the evaluation of surface fluxes and source terms) within each element.

In this method the solution domain is subdivided into triangular elements. The elements then are used to describe the variation of the variables. The computational nodes are located at their vertices. Any variable Φ is assumed to vary linearly within each element i.e. its shape function is linear. The control volumes are formed around each node by joining the centroids of the elements and midpoint on the elements edges. The conservation equations in integral form are the applied to these CVs.

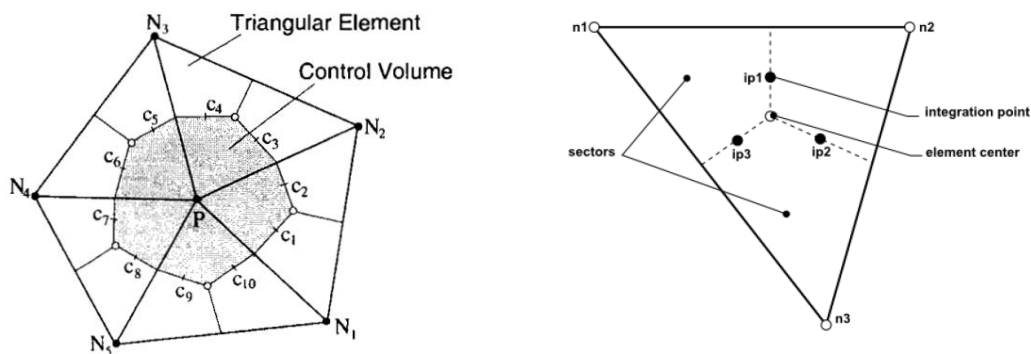


Fig.4.18 Domain Discretization

The first step in this methodology is to integrate the transport equations over each control volume, and the following step is the discretization of the volumes and surface integrals.

$$\underbrace{\frac{\partial}{\partial t} \int_V \rho \phi dV}_{\text{Unsteady}} + \underbrace{\oint_A \rho \phi \mathbf{V} \cdot d\mathbf{A}}_{\text{Advection}} = \underbrace{\oint_A \Gamma \nabla \phi \cdot d\mathbf{A}}_{\text{Diffusion}} + \underbrace{\int_V S_\phi dV}_{\text{Generation}}$$

Volume integrals are discretized within each element sector and stored to the control volume node n to which the sector belongs.

Surface integrals are discretized at the integration points (ip-n) located at the center of each surface segment within an element and then distributed to the adjacent control volumes. Because the surface integrals are equal and opposite for control volumes adjacent to the integration points, the surface integrals are guaranteed to be locally conservative.

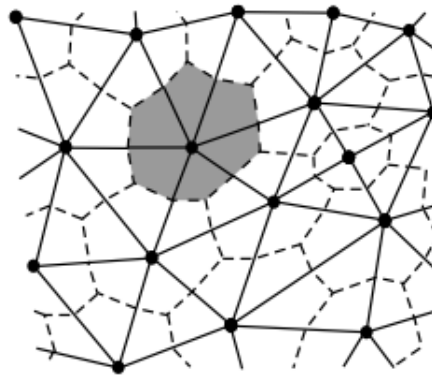


Fig. 4.19 Domain Discretization

Solution fields and other properties are stored at the mesh nodes n. However, to evaluate many of the terms, the solution field or solution gradients must be approximated at integration points on the sectors surfaces. ANSYS CFX uses finite-element linear shape functions to perform these approximations.

Order of accuracy

Many discrete approximations developed for CFD are based on series expansion approximations of continuous functions (such as the Taylor series). The order accuracy of the approximation is determined by the exponent on the mesh spacing or time step factor of the largest term in the truncated part of the series expansion, which is the first term excluded from the approximation. Increasing the order of accuracy of an approximation generally implies that errors are reduced more quickly with mesh or time step size refinement. ANSYS CFX uses second order accurate approximations as much as possible.

Advection term

The advection term of the transport equations, implemented in ANSYS CFX can be expressed in the form

$$\phi_{ip} = \phi_{up} + \beta \nabla \phi \cdot \Delta \vec{r} \quad (1)$$

Where ϕ_{ip} is the value of the variable at the integration point at the volume surface, ϕ_{up} is its value at the upwind node, and \vec{r} is the vector from the upwind node to the integration point ip. Choosing different values for β and $\nabla \phi$, yield different schemes.

For example a value of $\beta = 0$ yield a first order upwind differencing scheme. In fact the value $\beta \nabla \phi \cdot \Delta \vec{r}$ can be viewed as an anti-numerical diffusive correction applied to the upwind scheme.

By choosing the value $\beta = 1$ the scheme is second order accurate in space. In the simulations the selected value is in fact $\beta = 1$.

Diffusion Terms

Following the standard finite-element approach, shape functions are used to evaluate spatial derivatives for all the diffusion terms.

The shape function gradients can be evaluated at the actual location of each integration point ip (tri-linear interpolation) or at the location where each integration point surface intersects the element edge (linear-linear interpolation). The latter formulation improves solution robustness at the expense of locally reducing the spatial order-accuracy of the discrete approximation.

Pressure Gradient Term

As with the diffusion terms, the shape function used to interpolate can be evaluated at the actual location of each integration point or at the location where each ip surface intersects the element edge. By default the last interpolation is used unless the flow involves buoyancy, in which case the first type of interpolation is used for improved accuracy.

Solution Strategy

ANSYS CFX uses a coupled solver, which solves the hydrodynamic equations (for u, v, w, p) as a single system. This solution approach uses a fully implicit discretization of the equations at any given time step. For steady-state problems, the time-step behaves like an ‘acceleration parameter’, to guide the approximate solutions in a physically based manner to a steady-state solution. This reduces the number of iterations required for convergence to a steady state, or to calculate the solution for each time step in a time-dependent analysis.

ANSYS CFX uses a Multigrid (MG) accelerated Incomplete Lower Upper (ILU) factorization technique for solving the discrete system of linearized equations. It is an iterative solver whereby the exact solution of the equations is approached during the course of several iterations.

The linearized system of discrete equations described above can be written in the general matrix form:

$$[A][\phi] = b \quad (2)$$

The above equation can be solved iteratively by starting with an approximate solution ϕ^n , that is to be improved by a correction ϕ' , to yield a better solution, ϕ^{n+1} , that is

$$\phi^{n+1} = \phi^n + \phi' \quad (3)$$

Where ϕ' is a solution of

$$[A][\phi'] = r^n \quad (4)$$

With r^n , the residual of the sets of the equations

$$r^n = b - A \phi^n \quad (5)$$

Repeated application of this algorithm will yield a solution of the desired accuracy. By themselves, iterative solvers such as ILU tend to rapidly decrease in performance as the number of computational mesh elements increases. Performance also tends to rapidly decrease if there are large element aspect ratios present.

The convergence behavior of matrix inversion techniques is greatly enhanced by the use of a technique called ‘algebraic multigrid’. The multigrid process involves carrying out early iterations on a fine mesh and later iterations on progressively coarser virtual ones. The results are then transferred back from the coarsest mesh to the original fine mesh.

From a numerical standpoint, the multigrid approach offers a significant advantage. For a given mesh size, iterative solvers are efficient only at reducing errors that have a wavelength of the order of the mesh spacing. So, while shorter wavelength errors disappear quite quickly, errors with longer wavelengths, of the order of the domain size, can take an extremely long time to disappear. The Multigrid Method bypasses this problem by using a series of coarse meshes such that longer wavelength errors appear as shorter wavelength errors relative to the mesh spacing. To prevent the need to mesh the geometry using a series of different mesh spacing, ANSYS CFX uses Algebraic Multigrid.

Residuals normalization procedure

As described above, the residual, [r], is calculated as the imbalance in the linearized system of discrete equations. The residuals are then normalized for the purpose of solution monitoring and to obtain a convergence criterion.

For each solution variable, ϕ , the normalized residual is given in general by:

$$\widetilde{r}_\phi = \frac{r_\phi}{a_p \Delta\phi} \quad (6)$$

The exact calculation of a_p and $\Delta\phi$ is not discussed in the ANSYS CFX manual. However, some important notes are:

- The normalized residuals are independent of the initial guess.
- a_p is the central coefficient of the discretized control volume equation and therefore includes relevant advection, diffusion, source linearization, and other terms.
- For steady-state simulations, the time step is used only to under-relax the equations and is therefore excluded from the normalization procedure. This ensures that the normalized residuals are independent of the time step. The transient term is included in a_p for transient simulations.

Boundary Conditions

Inlet Boundary conditions

Two kinds of inlet (velocity and turbulence) boundary conditions have been used:

1. Uniform velocity $V = 0.75$ m/s for each of the two rectangular nozzle, with a uniform turbulence intensity of $I = 5\%$.
2. Velocity profiles from the experimental data and turbulence kinetic energy and dissipation rates derived from the experimental root mean squares values of the velocity components $V_{x,rms}, V_{y,rms}$.

$$\circ \quad k = \frac{1}{2} (V_{x,rms}^2 + V_{y,rms}^2 + V_{z,rms}^2)$$

$$\circ \quad \varepsilon = C_\mu^{3/4} k^{3/4} l^{-1}$$

With $C_\mu = 0.09$, and l is a characteristic length of the channel and it corresponds to the 10% of the channel nozzle hydraulic diameter. Since there are no experimental data for the velocity z-component, it has been assumed the equality $V_{y,rms}^2 = V_{z,rms}^2$.

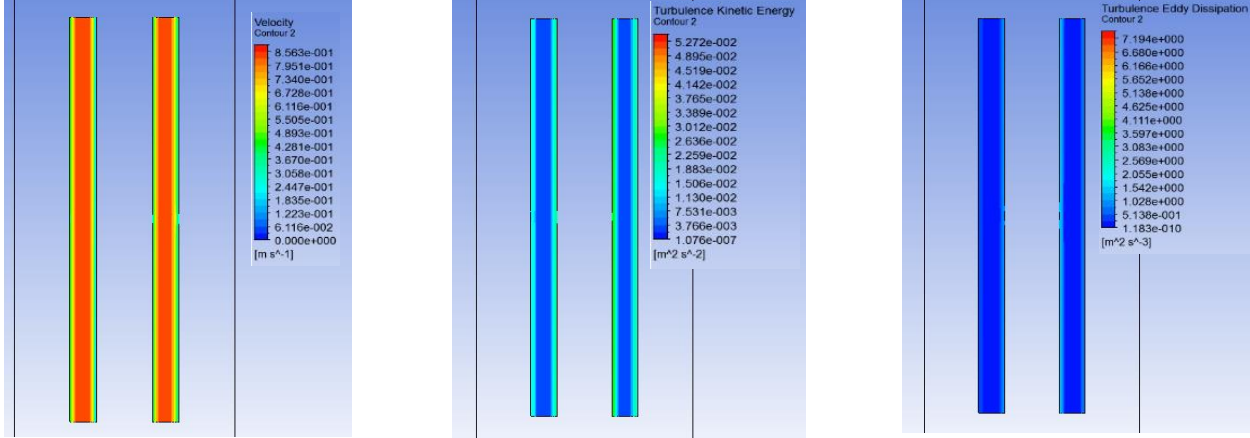


Fig. 4.20 Experimental Inlet Boundary Conditions Plots

Outlet boundary condition

For the outlet boundary condition it has been imposed a pressure outlet $P_{out} = 1 \text{ atm}$, since the tank is at atmospheric pressure and the water at ambient temperature.

Since the direction of the outflow is not positive, in the sense that it is highly possible to have an inflow of the mass flow, an outlet opening type boundary condition has been selected. An opening boundary condition allows the fluid to cross the boundary surface in both directions normal to the outlet surface.

Turbulence Models

Three main RANS turbulence models have been validated:

- Standard $k\epsilon$ turbulence model
- $k\omega$ -based Shear Stress Transport model (SST)
- Speziale-Sarkar-Gatski Reynolds stress transport turbulence model (SSG-RSM)

The first two models are two equations eddy-viscosity models, for the mathematical closure of the RANS problem, they add two transport equations to the PDE problem and they use the Boussinesq approximation for the evaluation of the Reynolds stress tensor $\tau_{Reij} = -\rho \overline{v'_i v'_j}$.

$$\tau_{Reij} = \mu_T \left(\frac{\partial \overline{v}_i}{\partial x_j} + \frac{\partial \overline{v}_j}{\partial x_i} \right) \quad (7)$$

The Reynolds stress transport model does not make use of the Boussinesq approximation but it defines six transport equations for each independent component of the Reynolds stress tensor. For three dimensional flows, indeed, the eddy viscosity may not be a scalar but a tensor quantity, this model takes into account the potential anisotropy of the turbulent flow.

k – *epsilon* turbulence model

It is the most used turbulence model, proposed by Launder and Sharma (1974).

For the closure of the RANS mathematical problem, this models add two transport equations for two different turbulence quantities:

- *k*: turbulent kinetic energy
- ϵ : turbulent kinetic energy dissipation term

By adding the transport equations for *k* and ϵ , to the RANS mass and momentum PDEs, it is the possible to solve for *k* and ϵ , and then evaluate the eddy viscosity as

$$\mu_T = C_\mu \rho \frac{k^2}{\epsilon} \quad (8)$$

k – *omega*-based Shear Stress Transport model

It is a two equations turbulence model. It combines the features of *k ϵ* and *Wilcox k ω* turbulence models. The boundary layer is solved using the *k ω* model and the *k ϵ* model is used in the free stream flow. A blending function ensures a smooth transition between the two models.

SSG Reynolds stress transport turbulence model

This model is a high level elaborate turbulence model, the method of closure is called second order closure. The eddy viscosity approach has been replaced by a directly evaluation of the Reynolds independent stress components, accounting for the directional effect of the Reynolds stress field. The derivation of the transport equation for each component of the Reynolds stress tensor makes higher order correlation terms to appear between the fluctuating components of the velocity ($\overline{v'_i v'_j v'_k}$). The model consists of six transport equations for the Reynolds stress components and one equation for the turbulent dissipation rate. The increased number of transport equations leads to reduced numerical robustness, requires increased computational effort and often prevents their usage in complex flows.

Mesh

The computational domain has been created by using the Ansys software ICEM-CFD.

One of the main characteristic of solution verification procedures is that a mesh sensitivity analysis on the mesh should be done. For this work two kinds of meshes have been created to take into account the two types of boundary conditions.

In the case of uniform velocity inlet boundary condition, the domain includes the two rectangular jets, whose length is long enough to obtain a fully developed turbulent flow.

In the case of experimental velocity inlet boundary condition the two rectangular nozzles are excluded from the mesh domain.

In order to properly apply the Grid Convergence Index study for the solution verification part, each simulation has been performed by using three different sets of structured refined mesh, with a refinement ratio of $r = 1.3$.

In the following table are summarized the number of nodes used for the discretization of the domain.

MESH	M1 (fine)	M2 (medium)	M3 (coarse)
EXPERIMENTAL	50.048.295	38.340.930	18.444.356
UNIFORM	53.989.825	41.069.096	20.806.327

Uniform velocity inlet domain

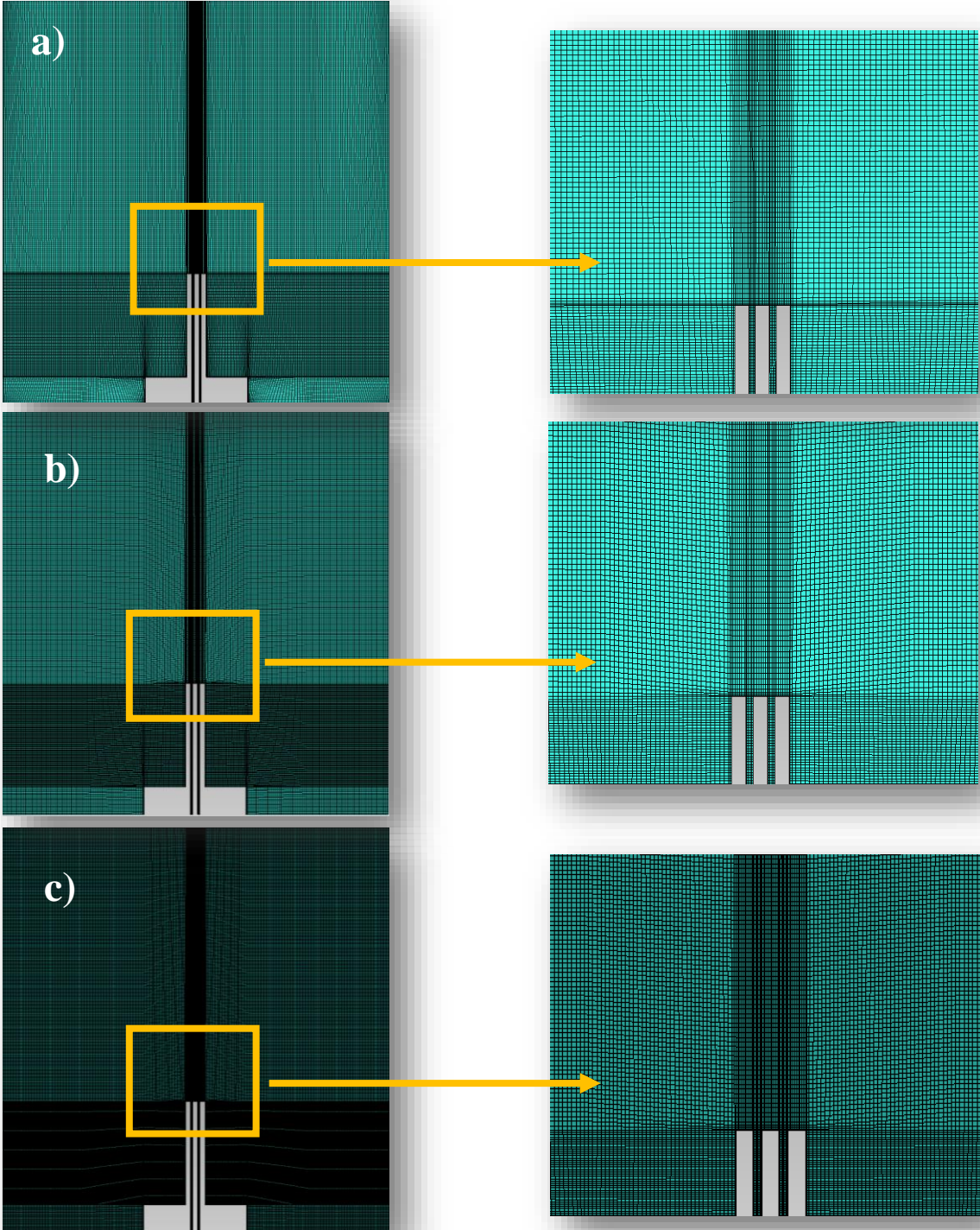


Fig. 4.21 Uniform Inlet Boundary a) coarse b) medium c) fine

Experimental velocity inlet domain

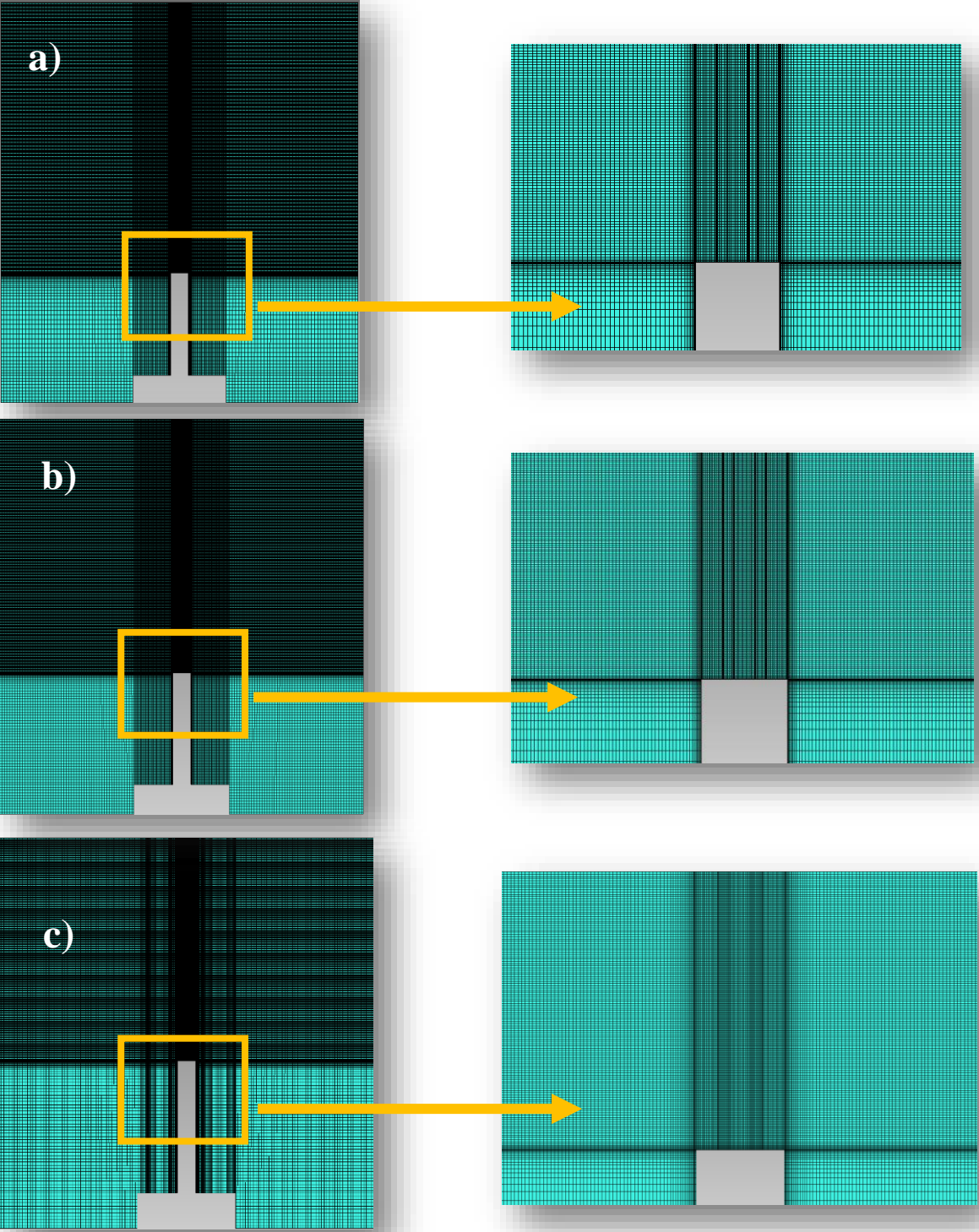


Fig. 4.23 Experimental Inlet Boundary a) coarse b) medium c) fine

Solution Verification

As assumptions of the solution verification procedures, we have assumed that two of the three main components of numerical error, round-off errors and iterative errors are negligible.

Round-off error can be considered negligible because in all the calculations all the numbers have been represented with a double-digit precision.

For the evaluation of the iteration error we know that it can be only estimated since we don't know the exact solution of our discretized problem, since we are solving it with an iterative method. But we can consider it negligible compared with the discretization error estimation. As we will show in a later section on average the relative discretization error uncertainty estimation (GCI) for all the quantities of interest is between 1-10 %, then if the relative iteration error is two order of magnitude lower than the discretization error we can argue that it is negligible [9,10]. In addition we know that the iteration error tends to follow closely with actual iterative error for a large class of problems. The normalized iterations residuals, for all simulations, were always between 10^{-6} and 10^{-7} . In order to relate the iteration residuals with the relative iteration error, we can assume as a good estimate of the discretization problem solution, the solution at the end of our simulation where the residuals are close to 10^{-7} , and then evaluate the relative iteration error through the iterations and comparing it with the normalized residuals. In the example that follows we can evaluate the velocity in a certain point of the domain (monitoring point) when the simulation residuals reached the value of 10^{-7} , and then evaluate the relative iteration error in the previous iterations. If we set a relative error level that can be considered negligible, let's say 0.01% (2 orders of magnitude less than the average discretization error uncertainty estimation) we can evaluate the corresponding residuals and show that our converged solution is well below the corresponding threshold.

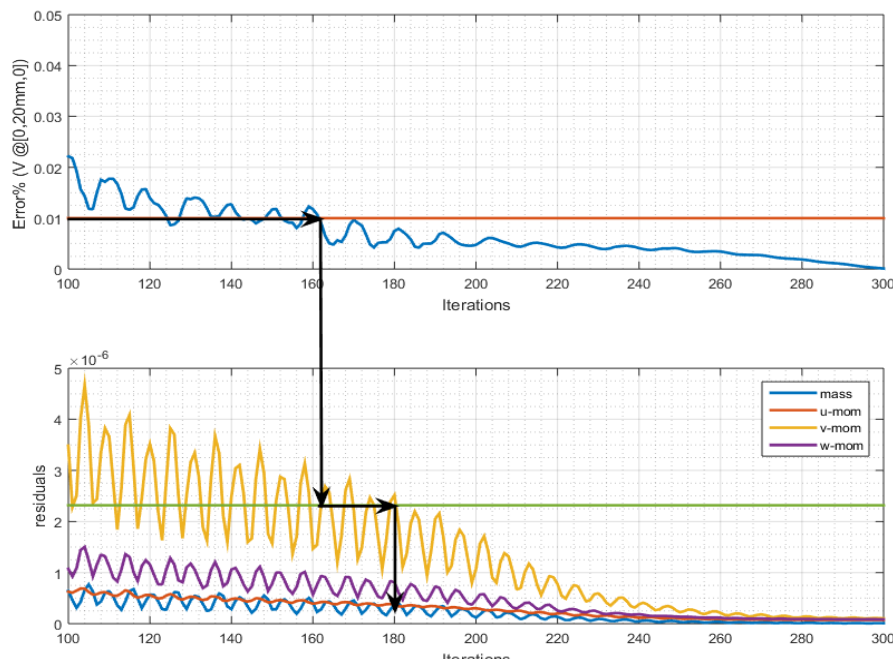


Fig. 4.24 Relative Iteration Error estimate and Residuals L2 norms (mass + momentum)

As we can see from fig.4.7, the higher residuals value corresponding to a relative iteration error of 0.01% is 2.3E-6, and since the convergence is not monotonic in this example, we will reach residuals values below this point after 180 iterations. As we can see the iterations have been stopped in this case at 300 (this is a relatively low number of iterations since we have used an initial guess of the solution from a coarse mesh simulation) and as we can see at that point (300 iterations) the residuals are well below the value of 2.3E-6, and then we can state that the converged solution is such that its iterative error can be negligible compared to the estimated discretization error uncertainty of 1%. This is not a rigorous justification for the exclusion of the iteration error contribution of the numerical error, but it can be taken as an estimate of the residuals values necessary, in order to have negligible values of the iteration errors.

For the solution verification phase of this work all the simulations results have been post-processed in order to obtain the Grid Convergence Index for each of the System Response Quantities (SRQ) of interests. In order to evaluate the Grid Convergence Index a 3 step procedure have been conducted:

- **Step 1**

Linear interpolation of the system response quantities of interests on a single mesh, since all the results comes from three sets of refined meshes, in order to evaluate the GCI the SRQs must be evaluated at the same node position. The results have been interpolated at the same position corresponding to the experimental data points coordinates, in order to facilitate also the solution validation part.

- **Step 2**

Evaluation of the observed order of accuracy

$$p = \frac{\left| \ln\left(\frac{|\phi_3 - \phi_2|}{|\phi_2 - \phi_1|}\right) \right|}{\ln(r)} \quad (9)$$

Where ϕ_3, ϕ_2, ϕ_1 corresponds to the interpolated SRQ of interest corresponding to the i-th refined mesh.

- **Step 3**

Evaluation of the Grid Convergence Index corresponding to the finest mesh solution

$$GCI = \frac{F_s}{r^p - 1} \left| \frac{\phi_2 - \phi_1}{\phi_1} \right| \quad (10)$$

For the factor of safety the value of $F_s = 1.25$, have been selected.

At the end of the solution verification calculations there were created for each SRQs, local and global, the discretization error bars, analogous to the experimental error bars.

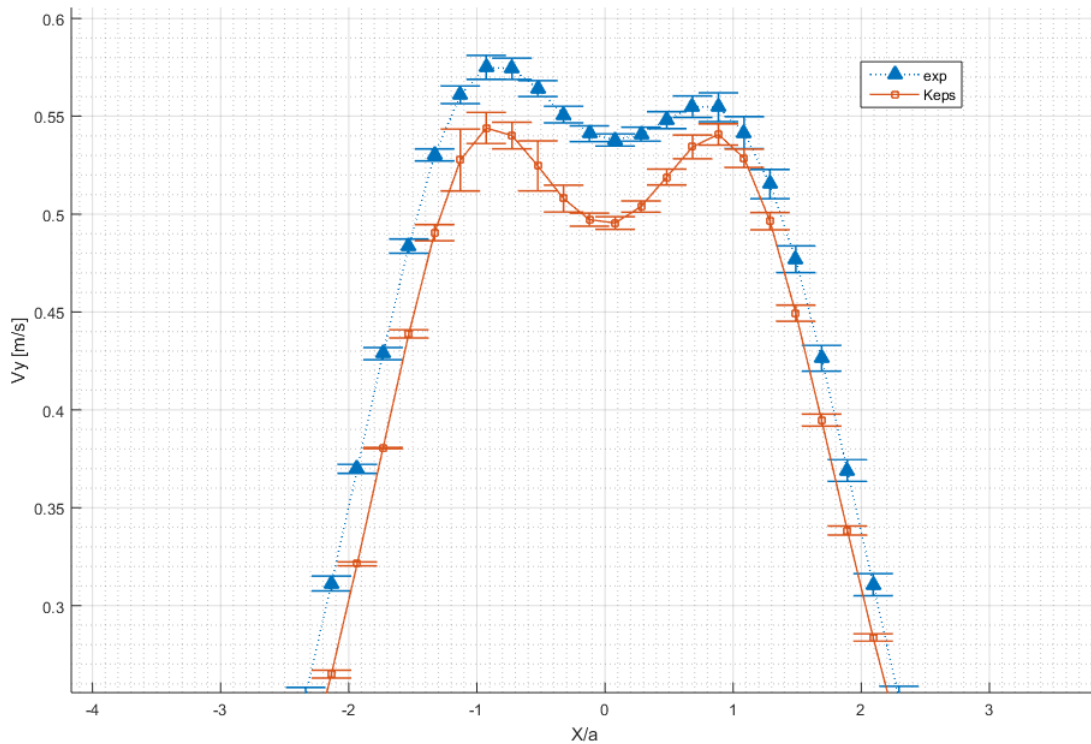


Fig. 4.25 Experimental and Numerical Uncertainty Bars (example)

To give a global estimate of the observed order of convergence \mathbf{p} , it has been calculated, for each local quantity (e.g. velocity profiles), the average observed order of accuracy \mathbf{p}_{ave} and its standard deviation $\sigma(\mathbf{p})$ to express the spreading of the results along each single profile.

The same as the observed order of accuracy has been done for the Grid Convergence Index GCI , evaluating its mean value $GCI_{mean}\%$ and its maximum value $GCI_{max}\%$.

System Response Quantities

The evaluation of the observed order of accuracy and the grid convergence index have been conducted for different systems response quantities:

- V_y velocity profile component
- V_x velocity profile component
- $\overline{V'_x V'_y}$ Reynolds stresses in the x-y plane
- Merging and Converging Points of the flow field

The velocities profiles and Reynolds stresses have been evaluated locally in the axial range between $-8a < x < 8a$ and at five height positions, corresponding to the experimental data measuring locations.

Y/a	1.4	4.2	7	10	11.5
------------	------------	------------	----------	-----------	-------------

Experimental Data Heights

Simulations control

As we have already mentioned in the Verification and Validation description, the numerical error coming from the solution of the discretized set of equations, consist of three main components:

- Round off error
- Iterative Error
- Discretization error

For the round off error, all the simulations and the post process calculations have been performed by using double precision of all the simulation data. It can be reasonably accepted that the round-off error in this case can be ignored since it doesn't play an important role in the numerical error sources.

All the equations residuals were monitored during the run of each simulation, and the range of the residuals for all the 18 simulations (*2 B.C x 3 Mesh x 3 Turbulence Models*) have been between $10^{-5} \div 10^{-7}$. It has been observed that the rate of convergence decreases as the mesh is refined, and the residuals tends to reach an asymptotic value higher than the coarse mesh case. Also for the iterative error it has been assumed that it does not contribute for the global numerical error.

For the convergence of the simulations, it has also been monitored the global conservation statistics for all transport equations (momentum and mass) and, in all the simulations, the global imbalance has been lower than 1%.

Solution Validation

Once the solution verification has been concluded, the solutions validation part, have been started.

For each of the experimental data profiles and for each simulation results have been locally evaluated:

- The validation comparison error $E = S - D$ and its maximum absolute value $|E|_{max}$
- The validation uncertainty $U_{val} = \sqrt{U_{exp}^2 + U_{num}^2}$
(An assumption has been made that the input uncertainty for the mathematical model was negligible $U_{input} = 0$).

For each simulation there were evaluated and tabulated also the following area averaged quantities in order to be able to globally evaluate the validation results of the different models:

$$\Phi_{ave} = \frac{1}{\Delta x} \int \Phi(x) dx \quad (11)$$

- Absolute validation comparison error $|E|_{ave}$
- Validation uncertainty $U_{val,ave}$
- Experimental uncertainty $U_{exp,ave}$
- Numerical uncertainty $U_{num,ave}$
- Absolute validation comparison error plus validation uncertainty $|E|_{ave} + U_{val,ave}$

The absolute validation comparison error plus uncertainty $|E|_{ave} + U_{val,ave}$ have been then, together with its maximum value $|E|_{max}$, used for globally evaluate the quality of the various turbulence models and boundary conditions.

Because of the strong smoothing nature of the integration operator, there have been evaluated the local $|E|_{ave} + U_{val,ave}$ values for different models and plotted.

The Experimental uncertainty $U_{exp,ave}$ and Numerical uncertainty $U_{num,ave}$, have been evaluated in order to have a global evaluation about their magnitude and if they are comparable or one of the two is dominant with respect to the other.

5 Results

V_y Contour plots

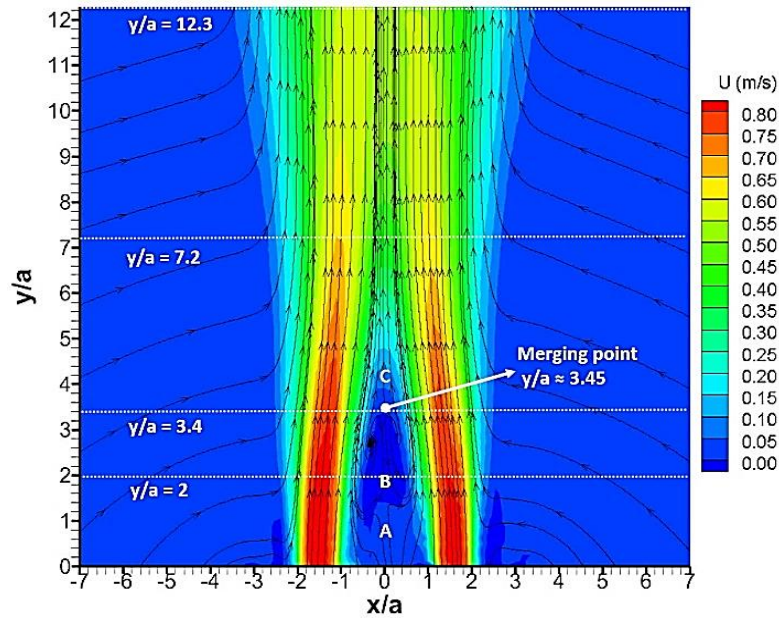


Fig. 5.26 Experimental Velocity V_y contour plot

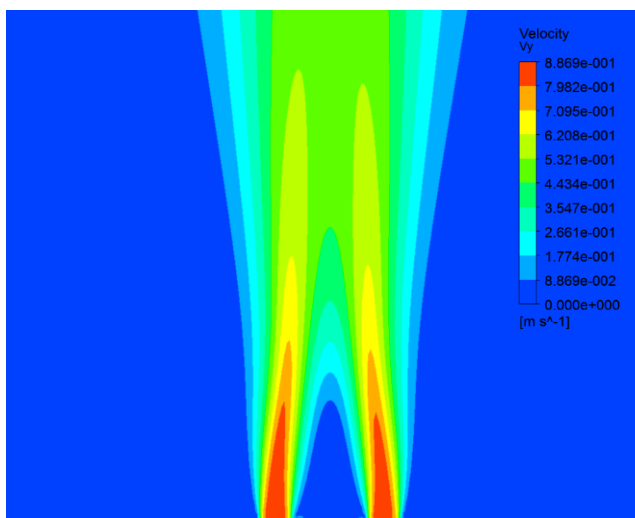


Fig. 5.28 Ke Velocity V_y contour plot - Experimental B.C

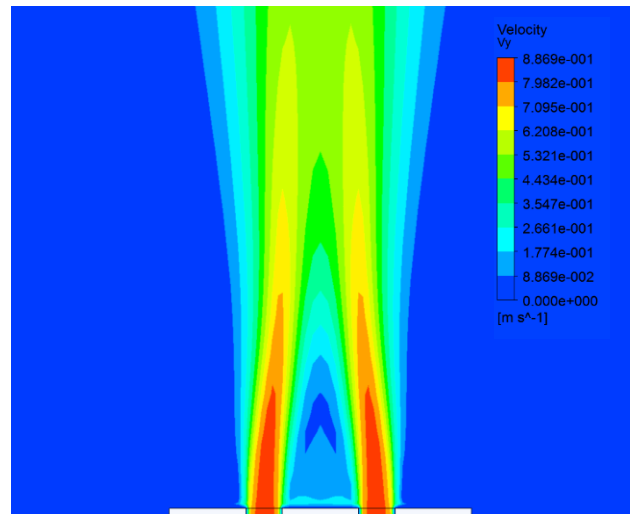


Fig. 5.27 Ke Velocity V_y contour plot - Uniform B.C

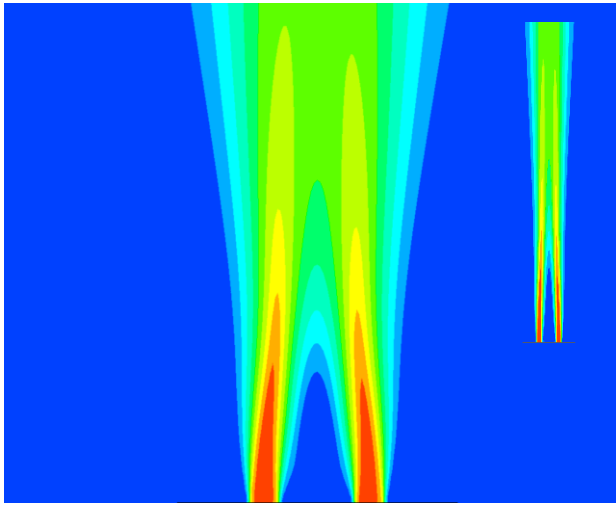


Fig. 5.4 SST Velocity V_y contour plot -Experimental B.C

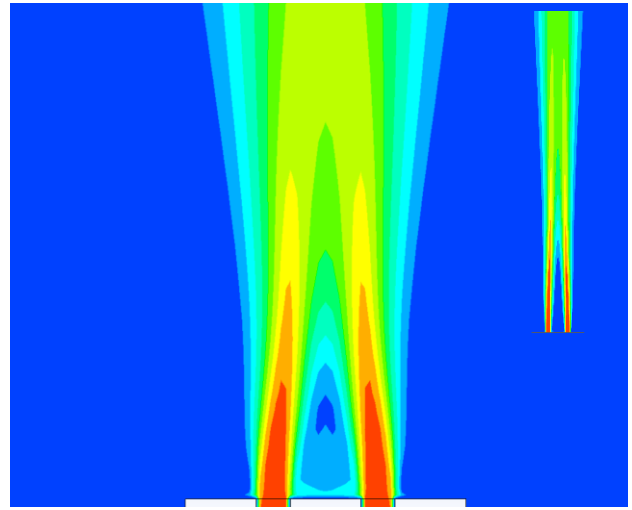


Fig. 5.5 SST Velocity V_y contour plot - Uniform B.C

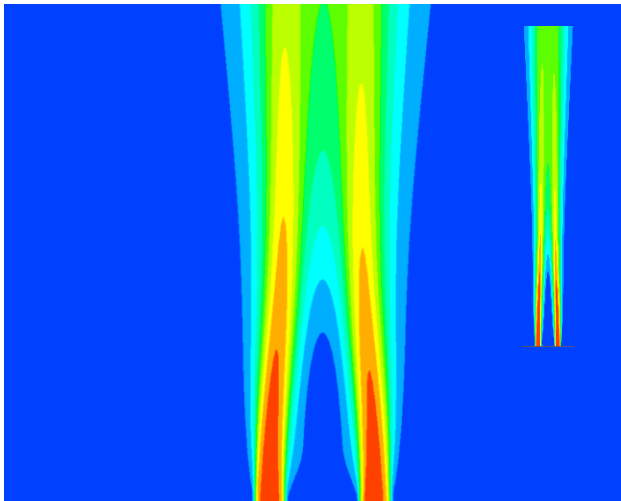


Fig. 5.6 RSM Velocity V_y contour plot -Experimental B.C

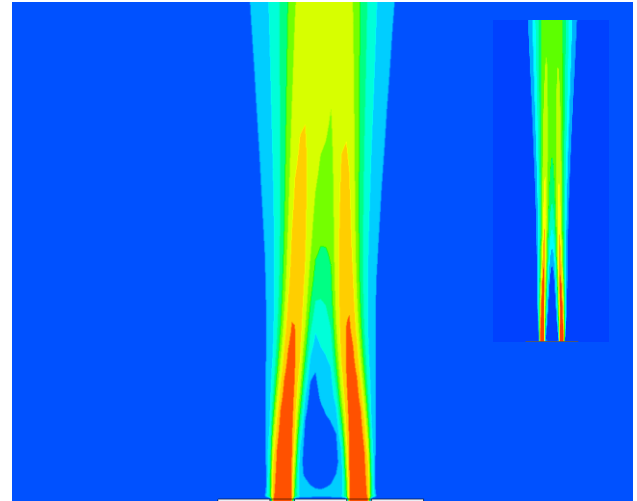
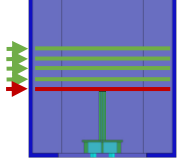


Fig. 5.7 RSM Velocity V_y contour plot -Uniform B.C

It can be noted a first important characteristic of the solutions, in the case of uniform velocity boundary condition the K_ϵ and SST turbulence models have a symmetrical velocity profile along the jets centerline. Instead in the case of experimental velocity boundary conditions the two models are able to capture the velocity profile asymmetry as showed in the experimental measurement plot. The exception is given by the Reynolds stress model where also in the case on uniform velocity profile, it is able to capture the velocity profile asymmetry but as we will see this model is not able to give good simulations predictions when compared with the experimental data.



V_y at $Y/a = 1.4$

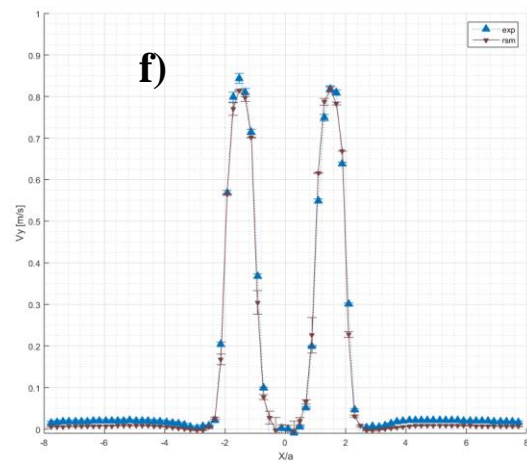
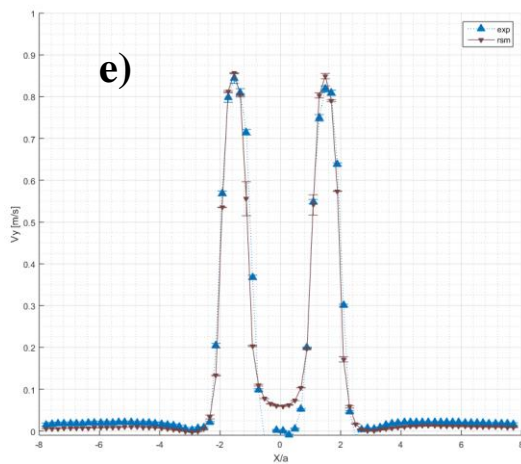
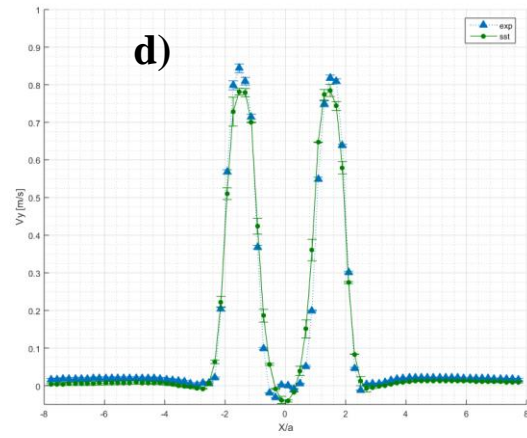
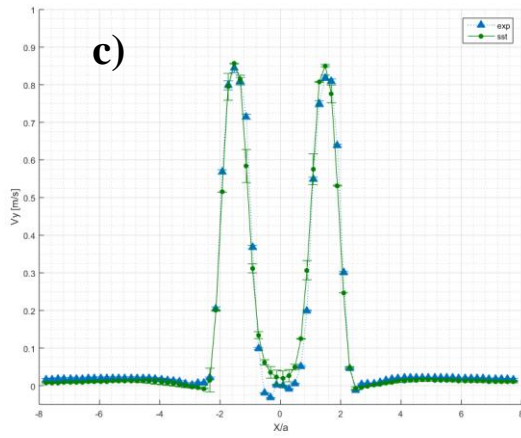
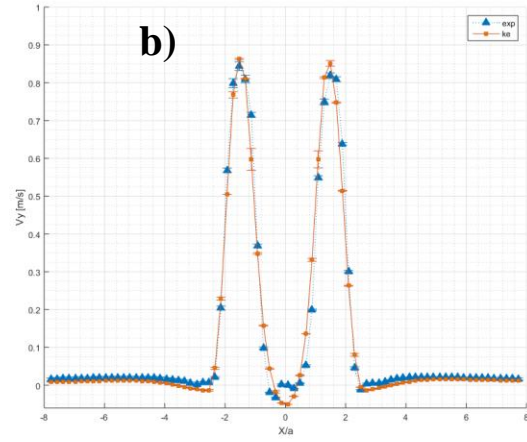
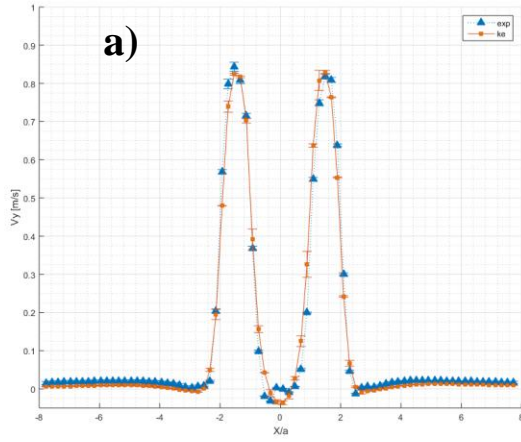


Fig. 5.8 V_y velocities profiles: a) ke Exp. B.C. b) ke Unif. B.C. c) sst Exp. B.C. d) sst Unif. B.C. e) rsm Exp. B.C. f) rsm Unif. B.C.

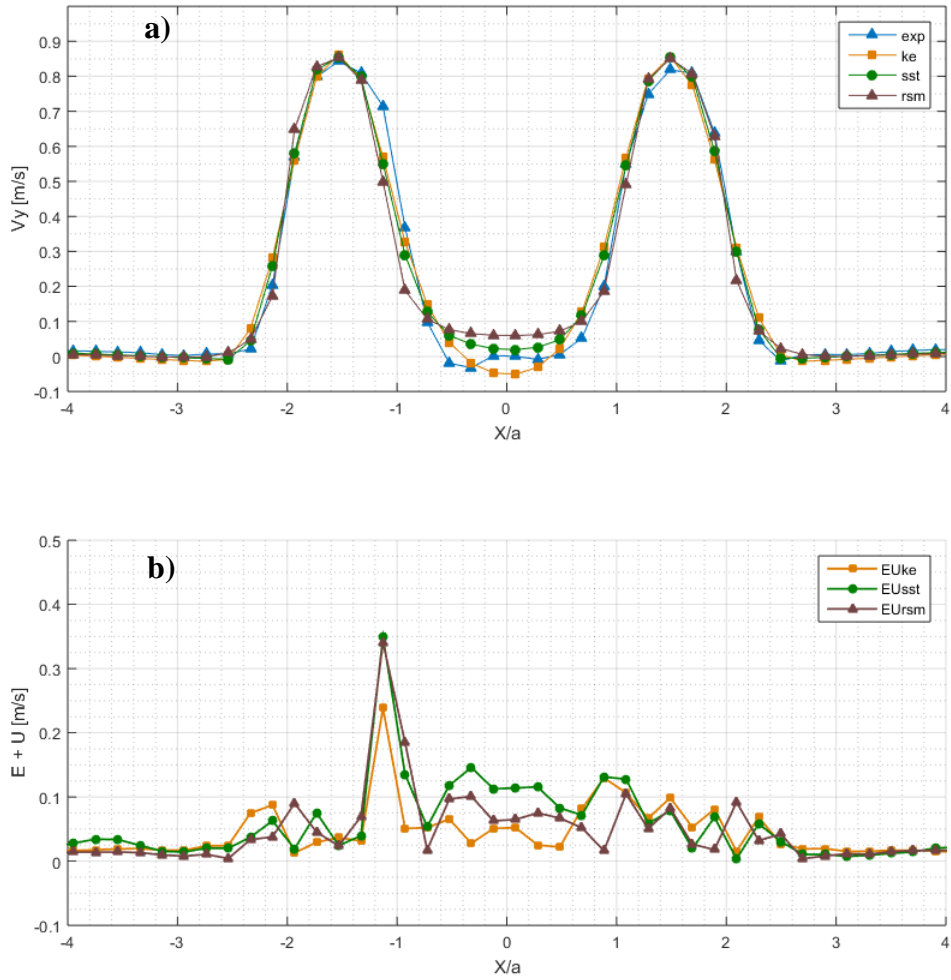


Fig. 5.9 Experimental Velocity inlet case a) V_y velocity profiles – models comparison
 b) Validation absolute modelling error + validation Uncertainty

EXPERIMENTAL	KE	SST	RSM
Pav	1.79	1.53	1.78
Pstd	0.34	0.41	0.37
GCI_{mean} %	1.51	1.89	1.02
GCI_{max} %	6.84	16.47	5.87
 E [m/s]	0.0209	0.0181	0.0244
 E _{MAX} [m/s]	0.1463	0.1641	0.2152
U[m/s]	0.0037	0.0067	0.0039
U_{num}[m/s]	0.0011	0.0051	0.0014
U_{exp}[m/s]	0.0031	0.0027	0.0034
 E +U[m/s]	0.0289	0.0399	0.0329

Tab. 5.1 Experimental Velocity inlet case V&V

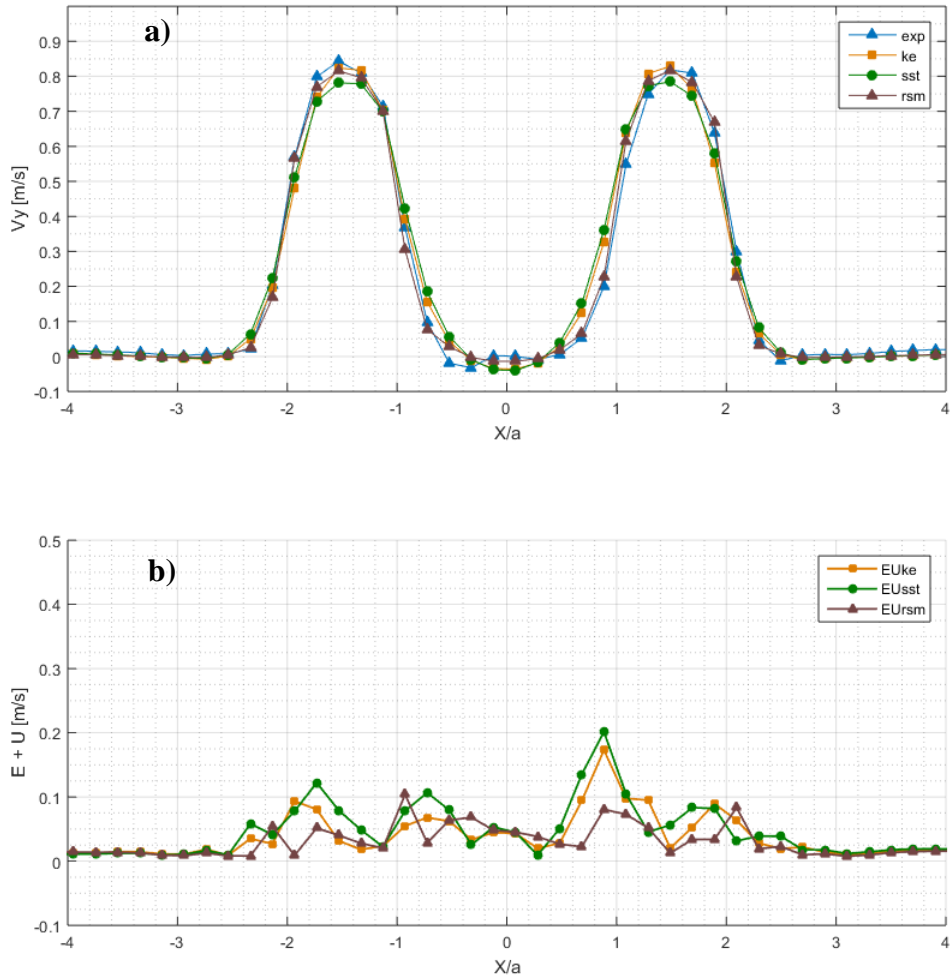
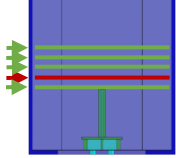


Fig. 5.10 Uniform Velocity inlet case a) V_y velocity profiles – models comparison b) Validation absolute modelling error + validation Uncertainty

UNIFORM	KE	SST	RSM
Pav	1.56	1.27	1.57
Pstd	0.43	0.33	0.41
GCI_{mean} %	1.18	1.20	1.01
GCI_{max} %	4.11	2.28	3.07
 E [m/s]	0.0207	0.0236	0.0158
 E MAX [m/s]	0.1270	0.1617	0.0733
U[m/s]	0.0051	0.0061	0.0058
U_{num}[m/s]	0.0029	0.0049	0.0035
U_{exp}[m/s]	0.0031	0.0031	0.0031
 E +U[m/s]	0.0259	0.0287	0.0217

Tab. 5.2 Uniform Velocity inlet case V&V



V_y at $Y/a = 4.2$

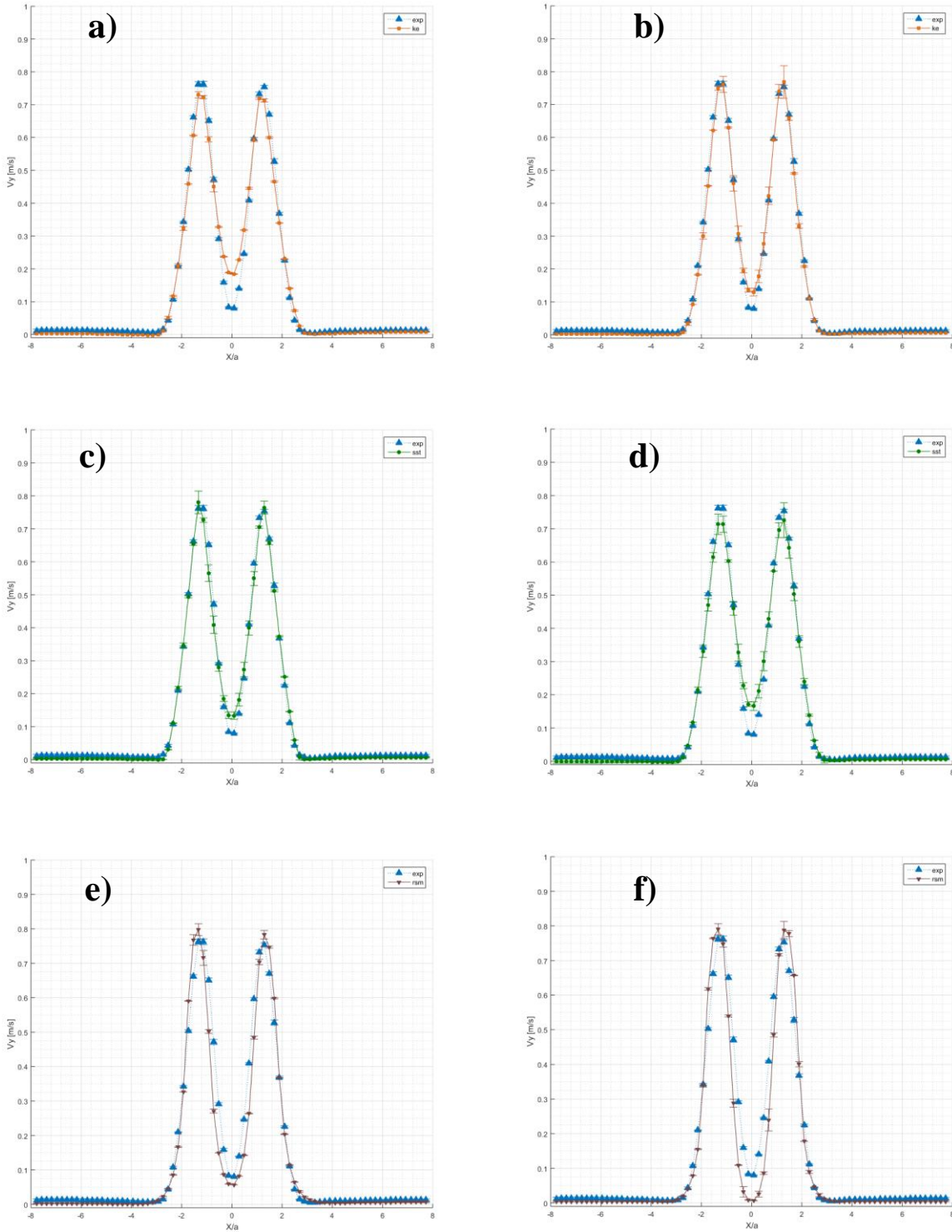


Fig. 5.11 V_y velocities profiles: a) ke Exp. B.C. b) ke Unif. B.C. c) sst Exp. B.C. d) sst Unif. B.C. e) rsm Exp. B.C. f) rsm Unif. B.C.

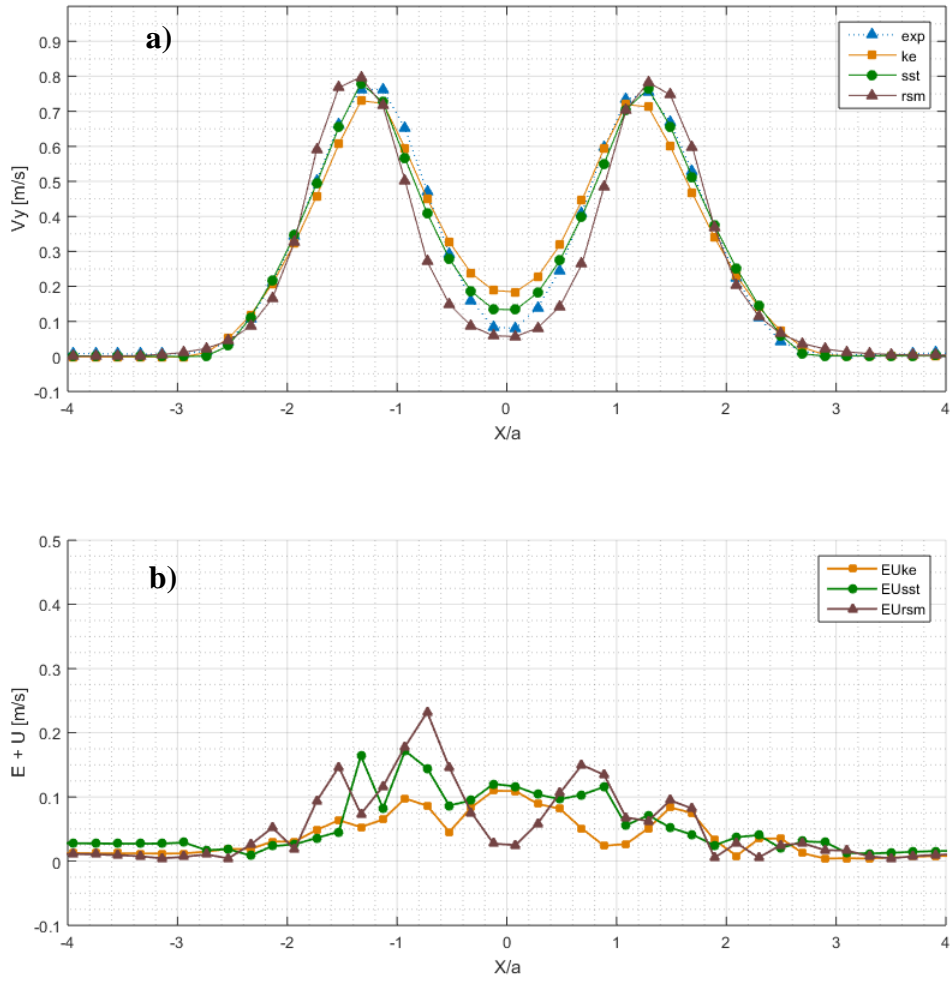


Fig. 5.12 Experimental Velocity inlet case a) V_y velocity profiles – models comparison b) Validation absolute modelling error + validation Uncertainty

EXPERIMENTAL	KE	SST	RSM
Pav	1.47	1.48	1.41
Pstd	0.43	0.43	0.39
GCI_{mean} %	0.68	4.81	0.69
GCI_{max} %	2.88	14.11	2.38
 E [m/s]	0.0135	0.0190	0.0264
 E _{MAX} [m/s]	0.1046	0.0857	0.2005
U[m/s]	0.0035	0.0077	0.0032
U_{num}[m/s]	0.0010	0.0065	0.0015
U_{exp}[m/s]	0.0030	0.0030	0.0030
 E +U[m/s]	0.0225	0.0170	0.0302

Tab. 5.3 Experimental Velocity inlet case V&V

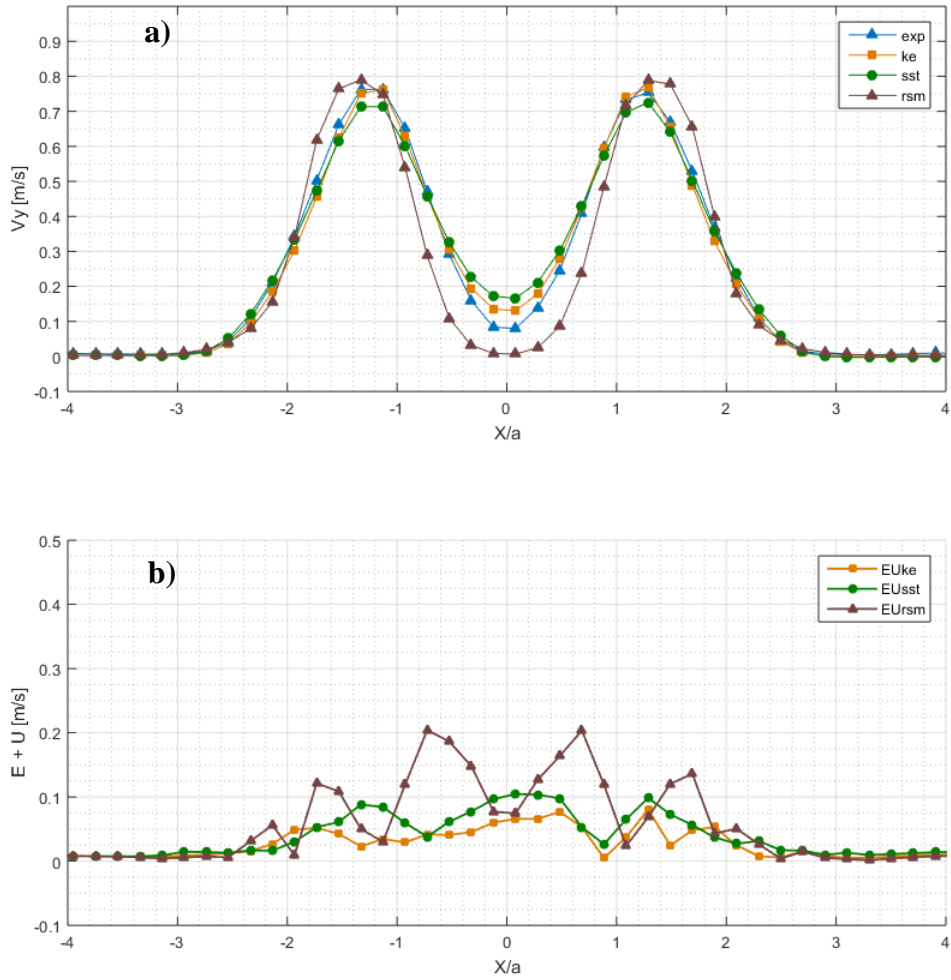
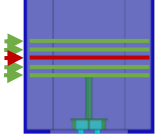


Fig. 5.13 Uniform Velocity inlet case a) V_y velocity profiles – models comparison b) Validation absolute modelling error + validation Uncertainty

UNIFORM	KE	SST	RSM
Pav	1.66	1.37	1.58
Pstd	0.40	0.36	0.45
GCI_{mean} %	1.30	1.68	2.32
GCI_{max} %	4.19	3.97	17.16
 E [m/s]	0.0124	0.0173	0.0310
 E _{MAX} [m/s]	0.0521	0.0880	0.1835
U[m/s]	0.0058	0.0080	0.0044
U_{num}[m/s]	0.0038	0.0066	0.0021
U_{exp}[m/s]	0.0030	0.0030	0.0030
 E +U[m/s]	0.0183	0.0232	0.0354

Tab. 5.4 Uniform Velocity inlet case V&V



V_y at $Y/a = 7$

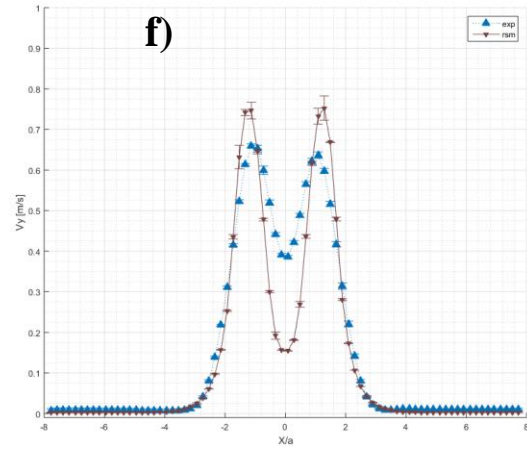
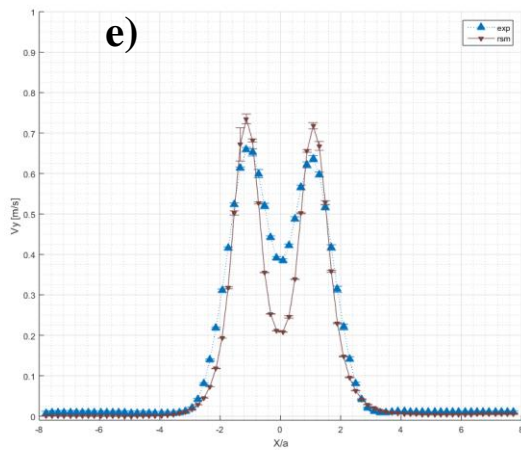
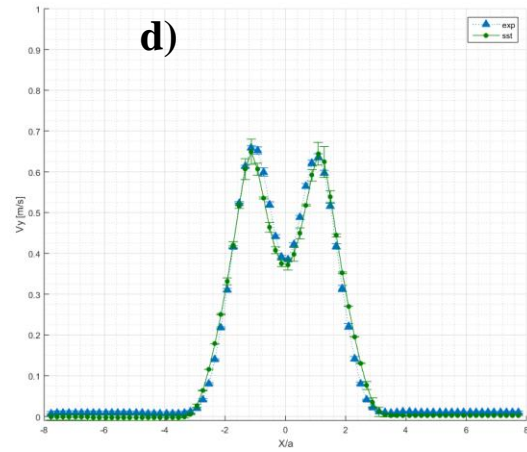
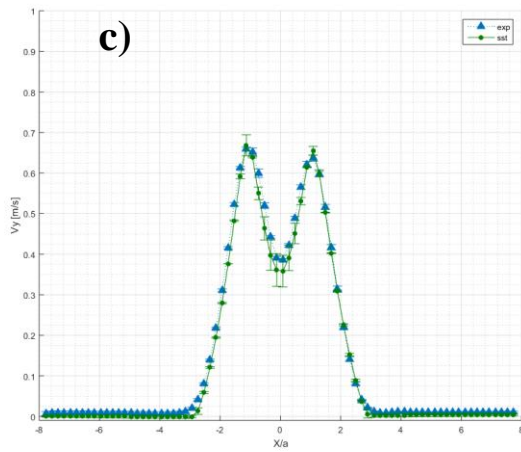
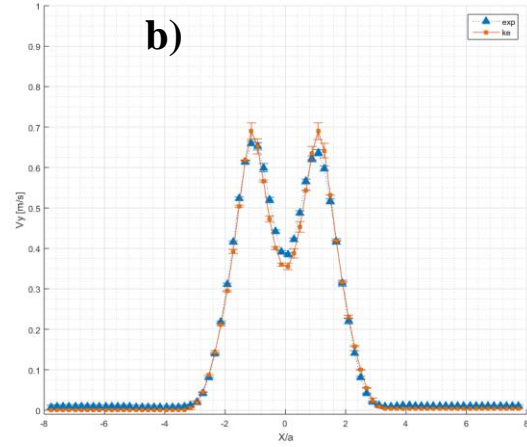
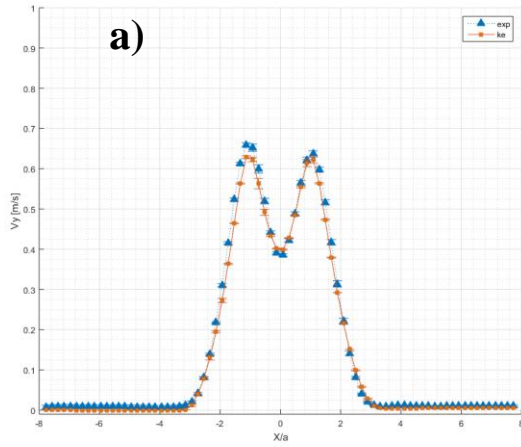


Fig. 5.14 V_y velocities profiles: a) ke Exp. B.C. b) ke Unif. B.C. c) sst Exp. B.C. d) sst Unif. B.C. e) rsm Exp. B.C. f) rsm Unif. B.C.

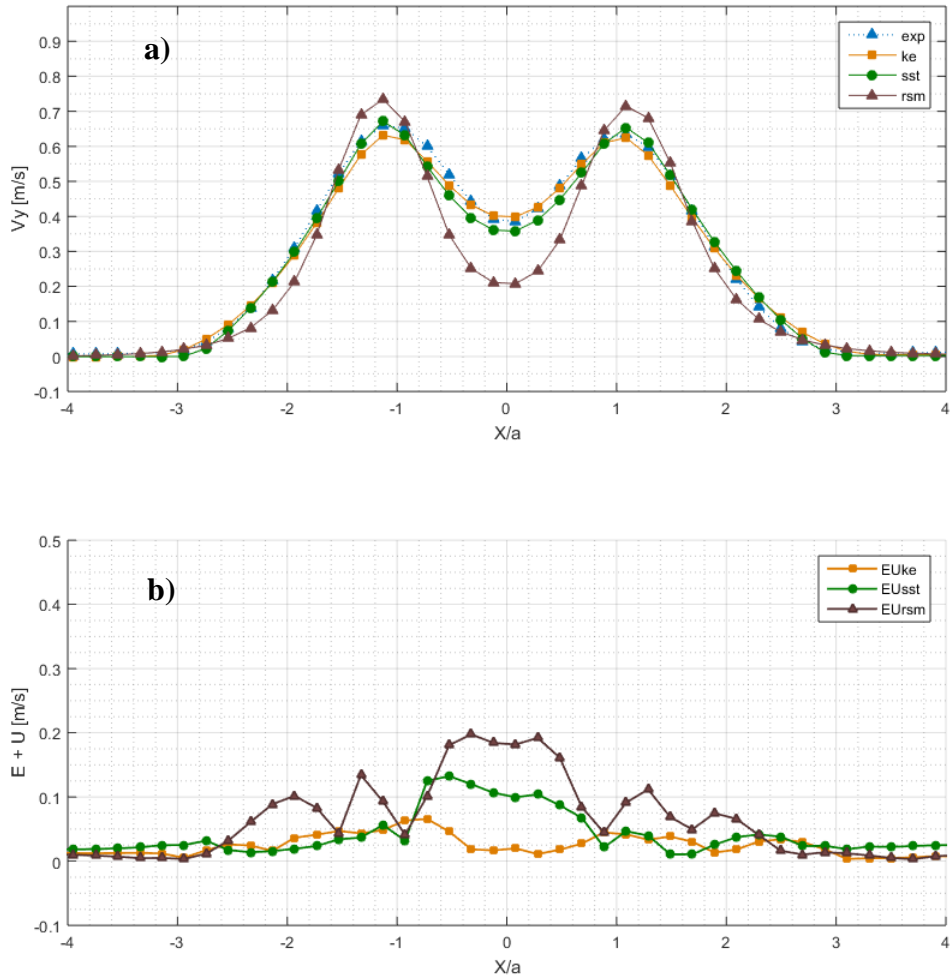


Fig. 5.15 Experimental Velocity inlet case a) V_y velocity profiles – models comparison b) Validation absolute modelling error + validation Uncertainty

EXPERIMENTAL	KE	SST	RSM
Pav	1.64	1.23	1.42
Pstd	0.39	0.38	0.48
GCImean %	0.60	2.63	0.43
GCImax %	1.80	8.97	1.38
 E [m/s]	0.0115	0.0133	0.0319
 E MAX [m/s]	0.0440	0.0620	0.1918
U[m/s]	0.0042	0.0073	0.0040
U_{num}[m/s]	0.0011	0.0054	0.0010
U_{exp}[m/s]	0.0037	0.0037	0.0037
 E +U[m/s]	0.0184	0.0312	0.0393

Tab. 5.5 Experimental Velocity inlet case V&V

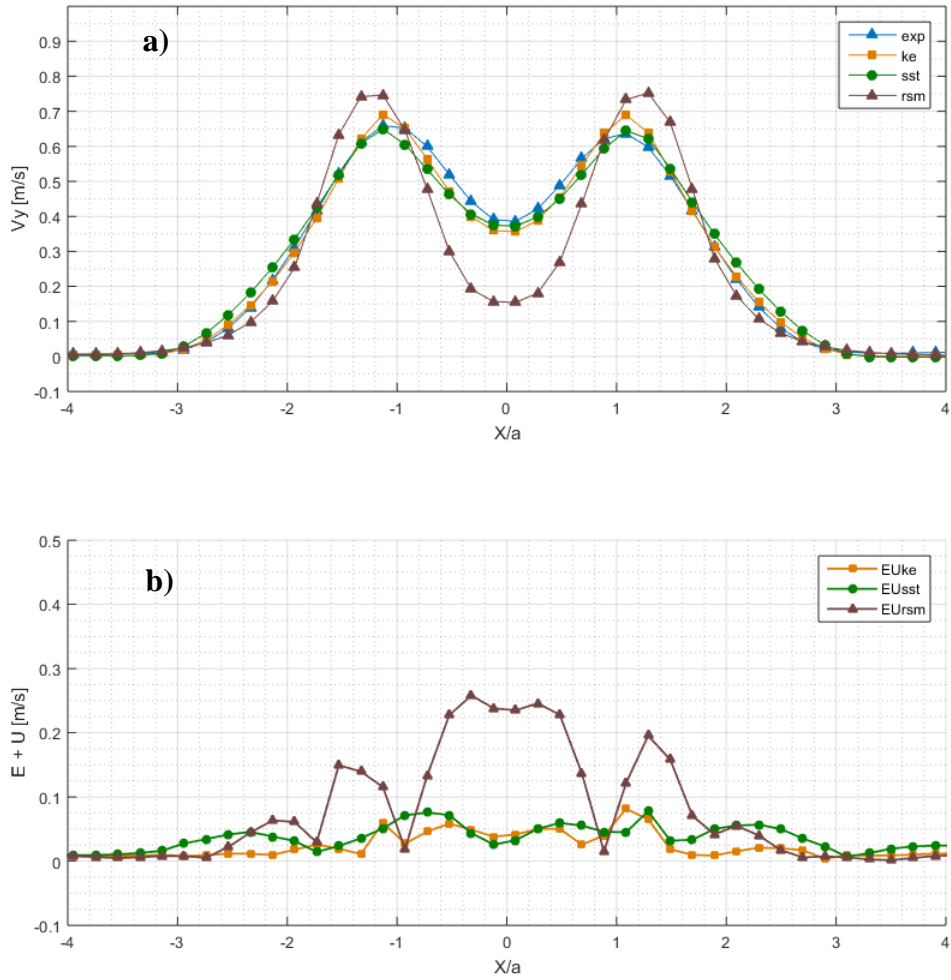
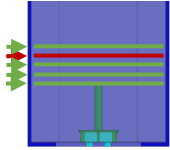


Fig. 5.16 Uniform Velocity inlet case a) V_y velocity profiles – models comparison b) Validation absolute modelling error + validation Uncertainty

UNIFORM	KE	SST	RSM
Pav	1.65	1.39	1.68
Pstd	0.38	0.44	0.42
GCI_{mean} %	0.52	0.88	0.50
GCI_{max} %	1.15	2.26	1.65
 E [m/s]	0.0119	0.0166	0.0399
 E MAX [m/s]	0.0526	0.0654	0.2499
U[m/s]	0.0050	0.0078	0.0049
U_{num}[m/s]	0.0023	0.0058	0.0021
U_{exp}[m/s]	0.0037	0.0037	0.0037
 E +U[m/s]	0.0167	0.0216	0.0448

Tab. 5.6 Uniform Velocity inlet case V&V



V_y at $Y/a = 10$

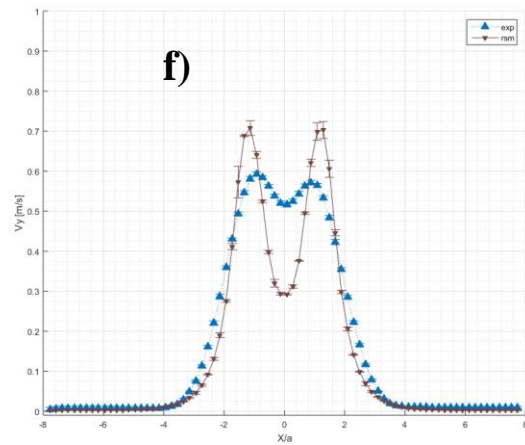
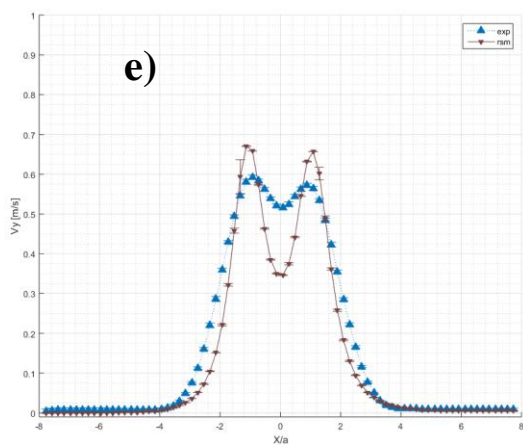
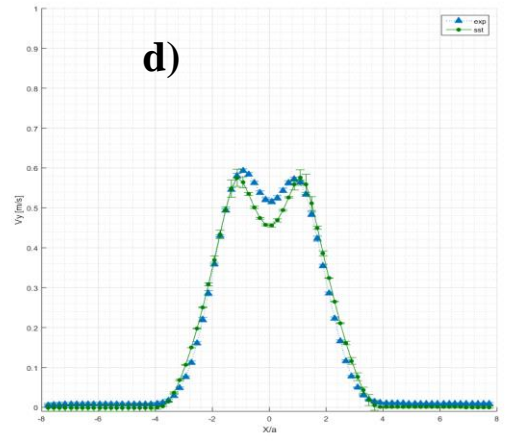
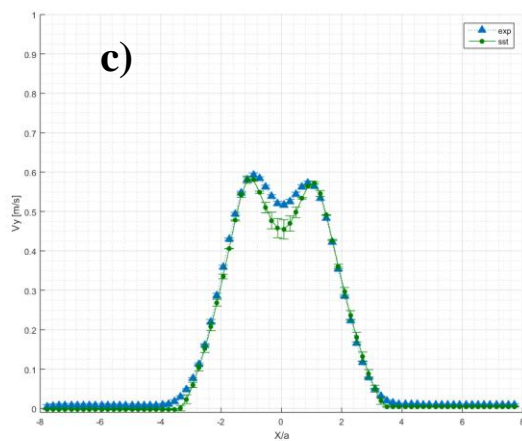
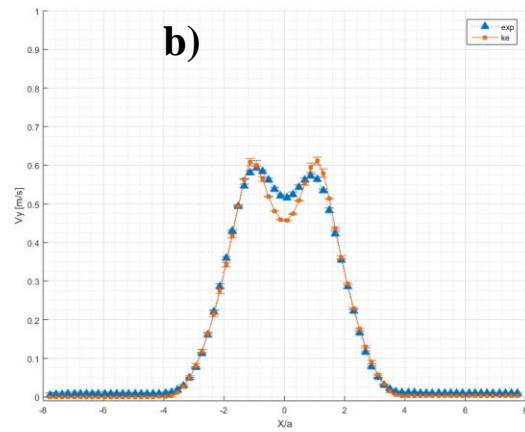
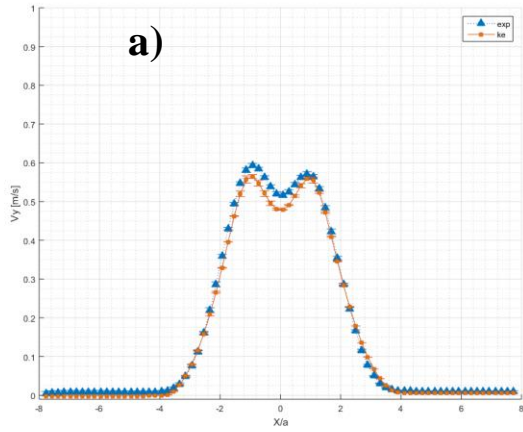


Fig. 5.17 V_y velocities profiles: a) ke Exp. B.C. b) ke Unif. B.C. c) sst Exp. B.C. d) sst Unif. B.C. e) rsm Exp. B.C. f) rsm Unif. B.C.

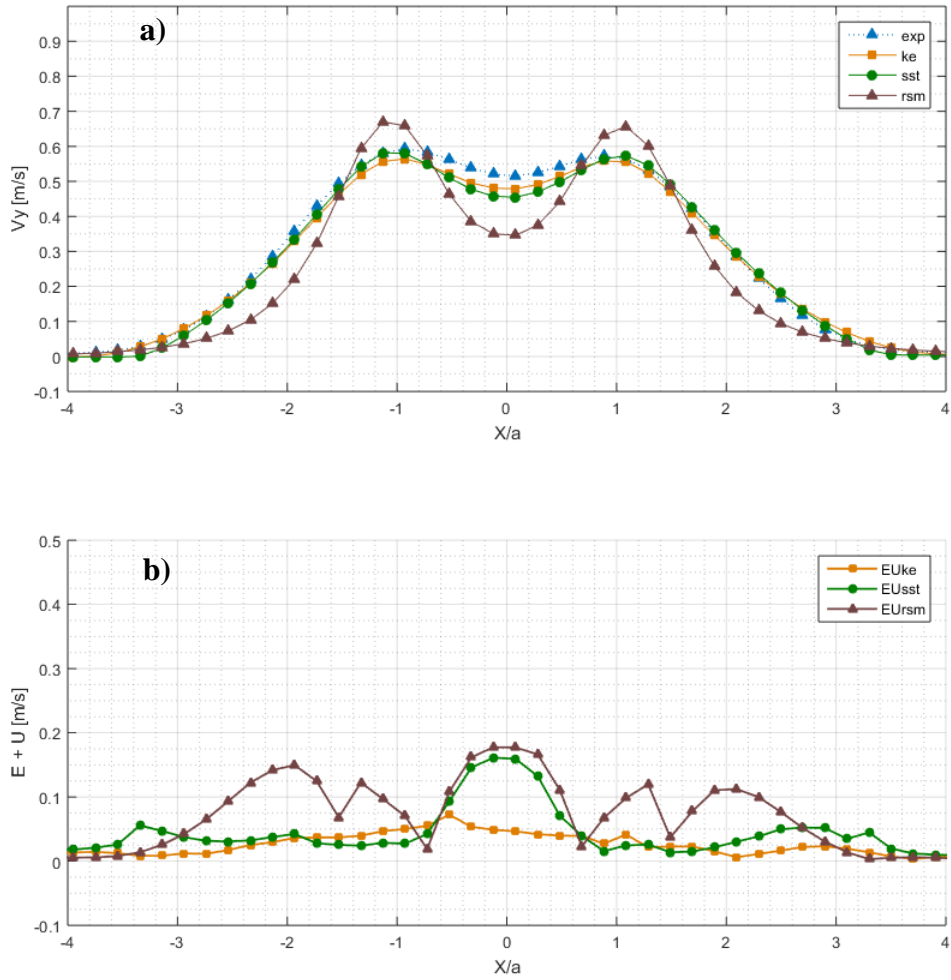


Fig. 5.18 Experimental Velocity inlet case a) V_y velocity profiles – models comparison b) Validation absolute modelling error + validation Uncertainty

EXPERIMENTAL	KE	SST	RSM
Pav	1.54	1.57	1.54
Pstd	0.45	0.41	0.44
GCI_{mean} %	0.57	1.44	0.71
GCI_{max} %	1.63	4.33	3.54
 E [m/s]	0.0121	0.0139	0.0350
 E MAX [m/s]	0.0428	0.0627	0.1702
U[m/s]	0.0041	0.0059	0.0042
U_{num}[m/s]	0.0010	0.0038	0.0012
U_{exp}[m/s]	0.0037	0.0037	0.0037
 E +U[m/s]	0.0187	0.0297	0.0432

Tab. 5.7 Experimental Velocity inlet case V&V

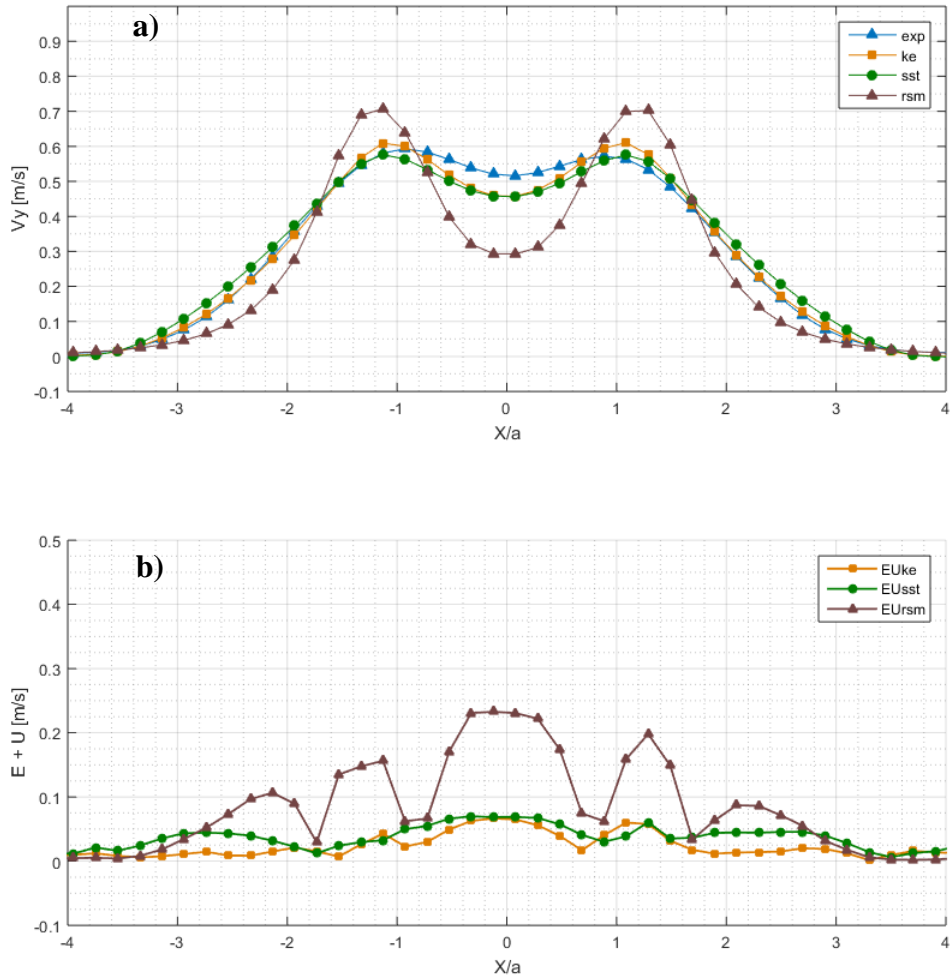
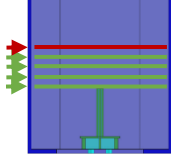


Fig. 5.19 Uniform Velocity inlet case a) V_y velocity profiles – models comparison b) Validation absolute modelling error + validation Uncertainty

UNIFORM	KE	SST	RSM
Pav	1.51	1.25	1.49
Pstd	0.42	0.41	0.46
GCImean %	0.32	0.62	0.68
GCImax %	0.87	1.76	2.56
 E [m/s]	0.0135	0.0185	0.0424
 E MAX [m/s]	0.0612	0.0652	0.2265
U[m/s]	0.0046	0.0071	0.0054
U_{num}[m/s]	0.0020	0.0053	0.0029
U_{exp}[m/s]	0.0037	0.0037	0.0037
 E +U[m/s]	0.0171	0.0232	0.0478

Tab. 5.8 Uniform Velocity inlet case V&V



V_y at $Y/a = 11.5$

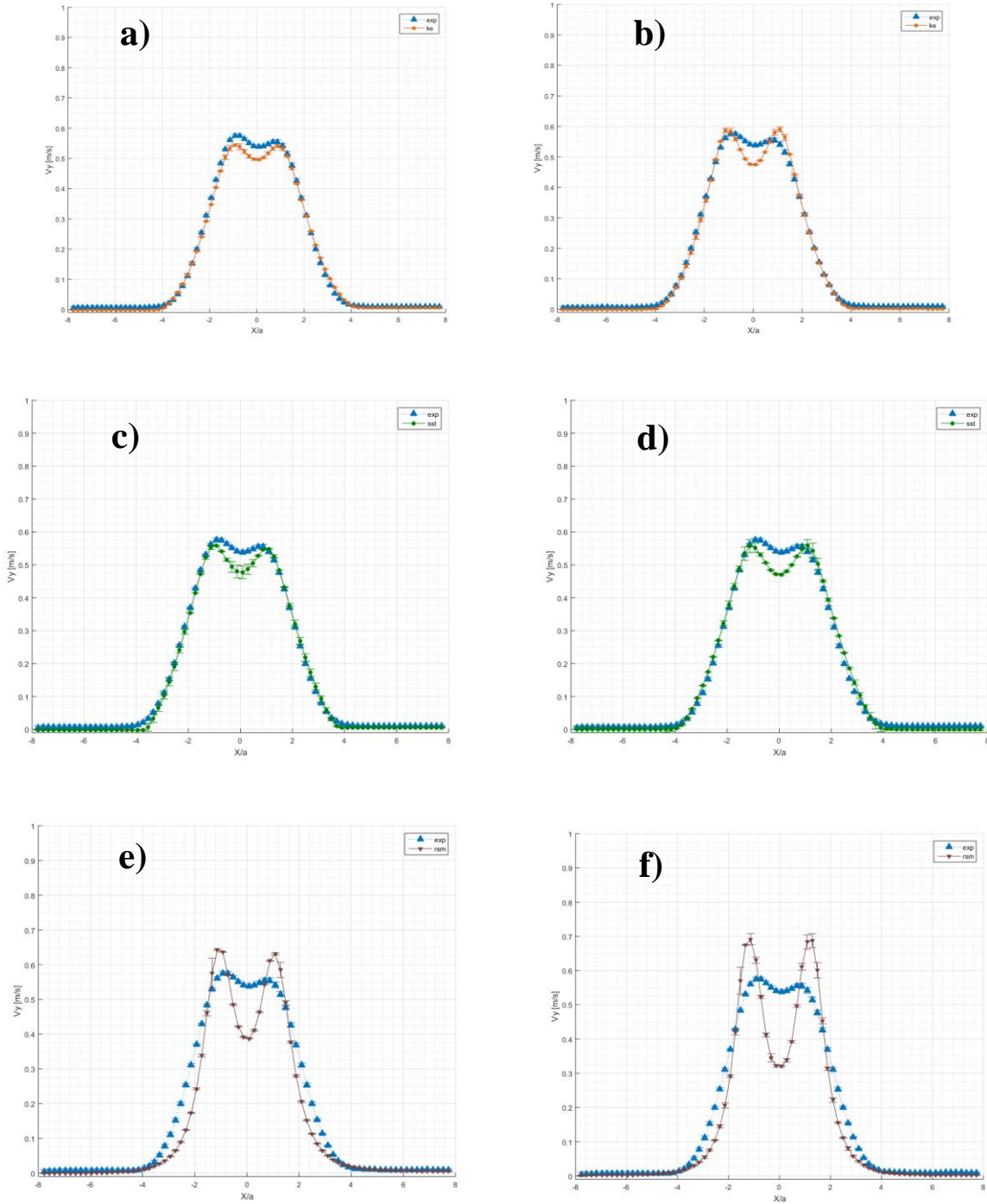


Fig. 5.19 V_y velocities profiles: a) ke Exp. B.C. b) ke Unif. B.C. c) sst Exp. B.C. d) sst Unif. B.C. e) rsm Exp. B.C. f) rsm Unif. B.C.

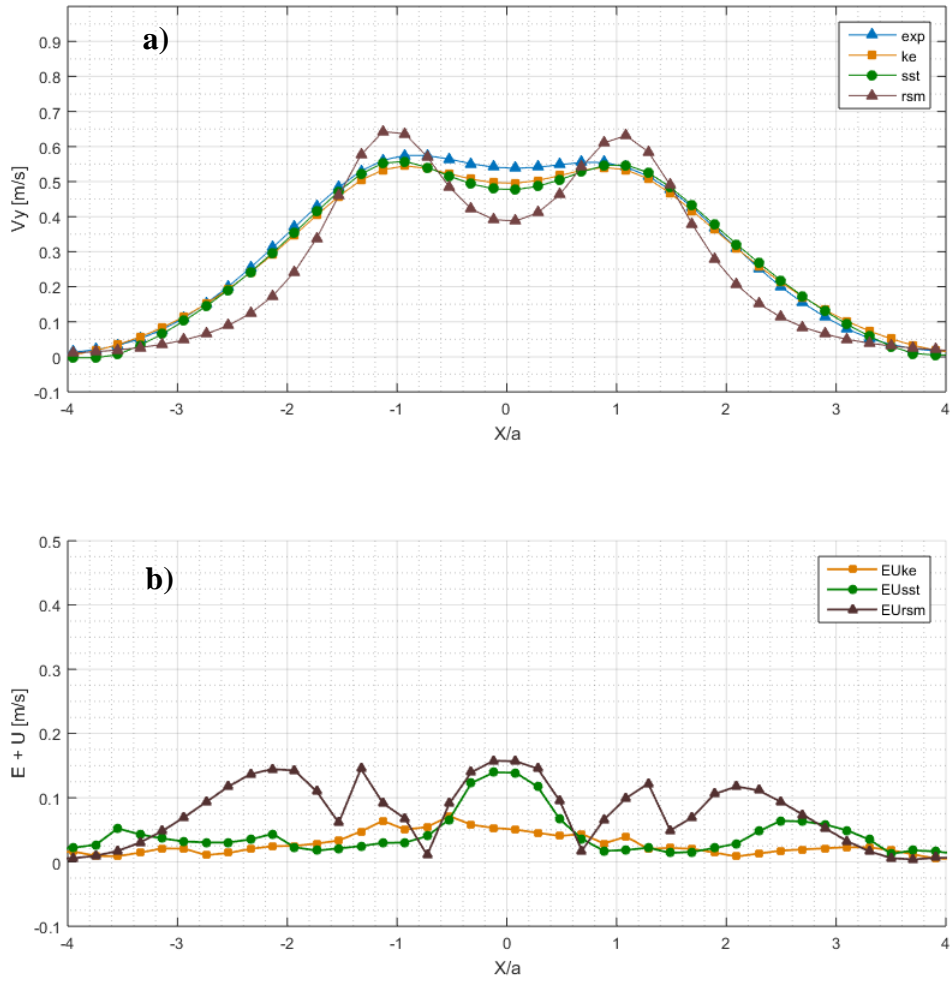


Fig. 5.20 Experimental Velocity inlet case a) V_y velocity profiles – models comparison b) Validation absolute modelling error + validation Uncertainty

EXPERIMENTAL	KE	SST	RSM
Pav	1.47	1.61	1.60
Pstd	0.46	0.45	0.44
GCI_{mean} %	1.08	1.05	0.80
GCI_{max} %	1.57	3.25	3.59
 E [m/s]	0.0122	0.0137	0.0360
 E _{MAX} [m/s]	0.0441	0.0616	0.1505
U[m/s]	0.0045	0.0060	0.0047
U_{num}[m/s]	0.0013	0.0034	0.0013
U_{exp}[m/s]	0.0040	0.0040	0.0040
 E +U[m/s]	0.0195	0.0283	0.0445

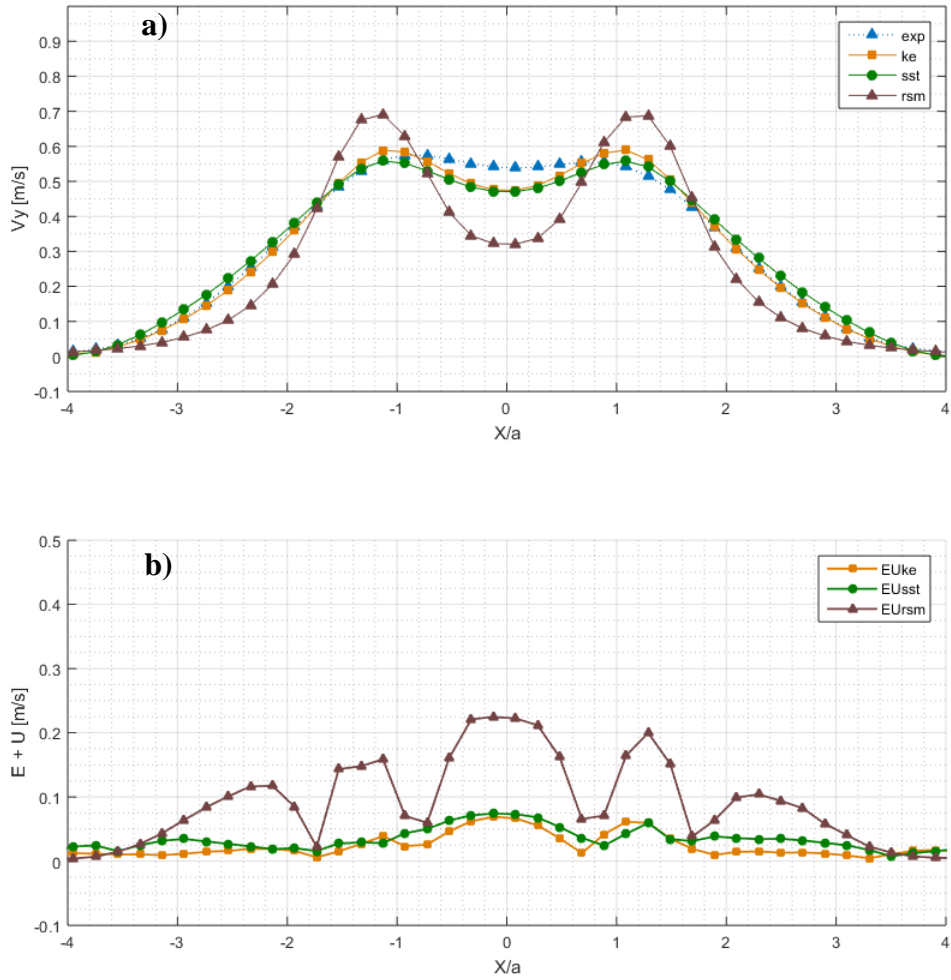
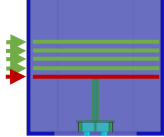


Fig. 5.21 Uniform Velocity inlet case a) V_y velocity profiles – models comparison b) Validation absolute modelling error + validation Uncertainty

UNIFORM	KE	SST	RSM
Pav	1.45	1.25	1.42
Pstd	0.44	0.40	0.44
GCI_{mean} %	0.28	0.59	0.76
GCI_{max} %	0.75	1.62	2.61
 E [m/s]	0.0127	0.0168	0.0455
 E _{MAX} [m/s]	0.0651	0.0697	0.2189
U[m/s]	0.0048	0.0073	0.0058
U_{num}[m/s]	0.0020	0.0055	0.0031
U_{exp}[m/s]	0.0040	0.0040	0.0040
 E +U[m/s]	0.0175	0.0216	0.0514

Tab. 5.10 Uniform Velocity inlet case V&V



V_X at $Y/a = 1.4$

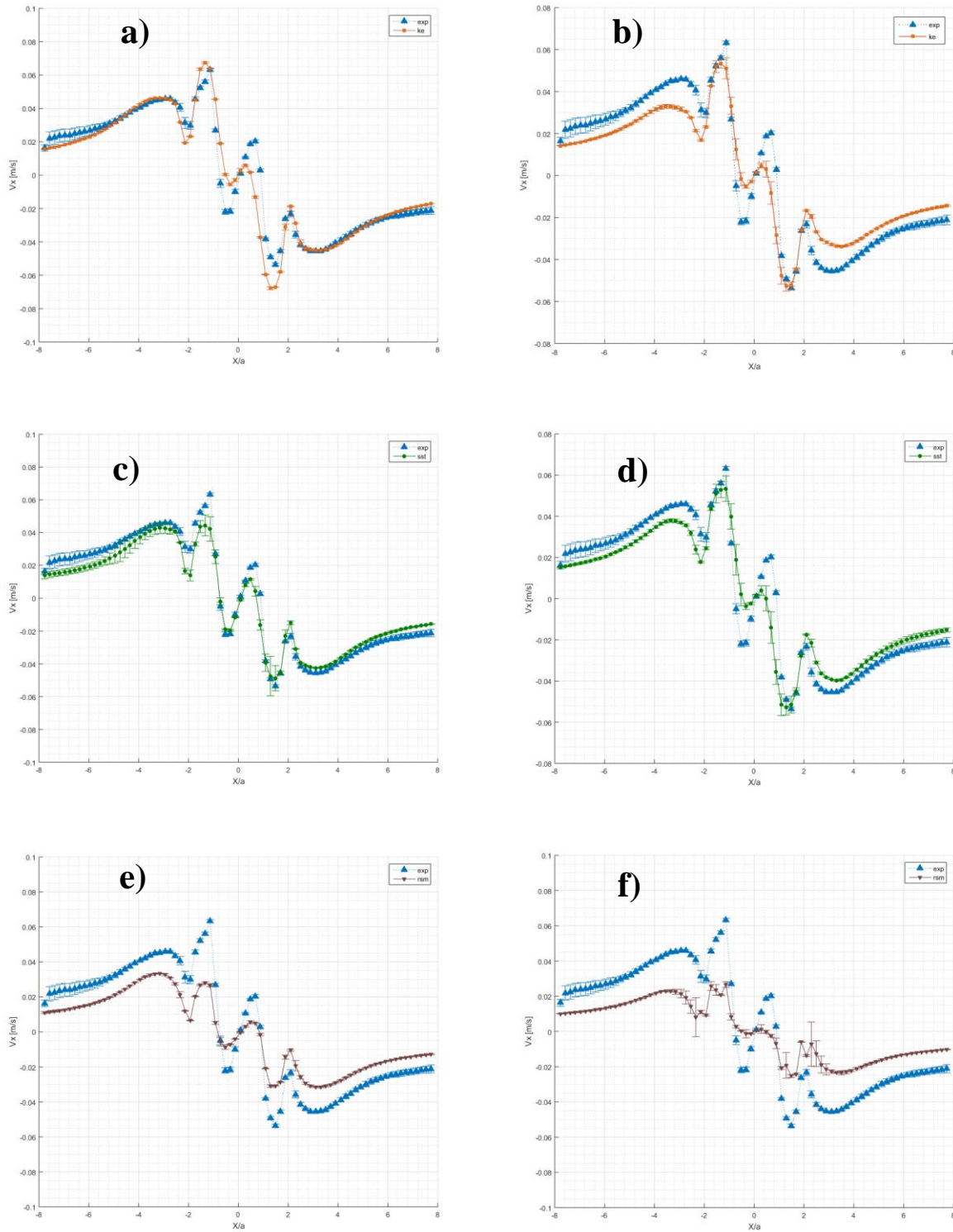


Fig. 5.22 V_x velocities profiles: a) ke Exp. B.C. b) ke Unif. B.C. c) sst Exp. B.C. d) sst Unif. B.C. e) rsm Exp. B.C. f) rsm Unif. B.C.

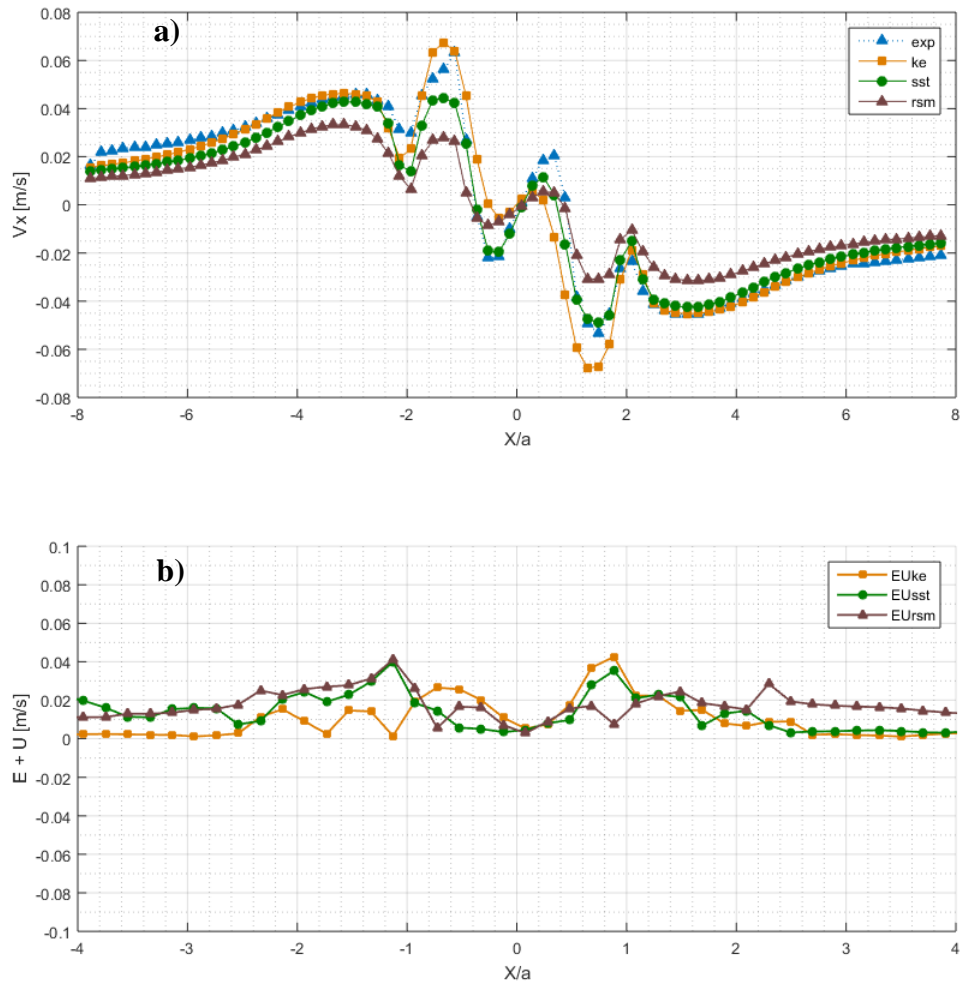


Fig. 5.23 Experimental Velocity inlet case a) V_x velocity profiles – models comparison b) Validation absolute modelling error + validation Uncertainty

EXPERIMENTAL	KE	SST	RSM
Pav	1.90	1.93	1.51824
Pstd	0.25	0.18	0.426574
GCI_{mean} %	1.15	0.65	1.068544
GCI_{max} %	4.97	1.38	3.982417
 E [m/s]	0.0054	0.0059	0.0126
 E _{MAX} [m/s]	0.0404	0.0209	0.0363
U[m/s]	0.0015	0.0025	0.0015
U_{num}[m/s]	0.0002	0.0015	0.0003
U_{exp}[m/s]	0.0031	0.0031	0.0031
 E +U[m/s]	0.0070	0.0070	0.0142

Tab. 5.11 Experimental Velocity inlet case V&V

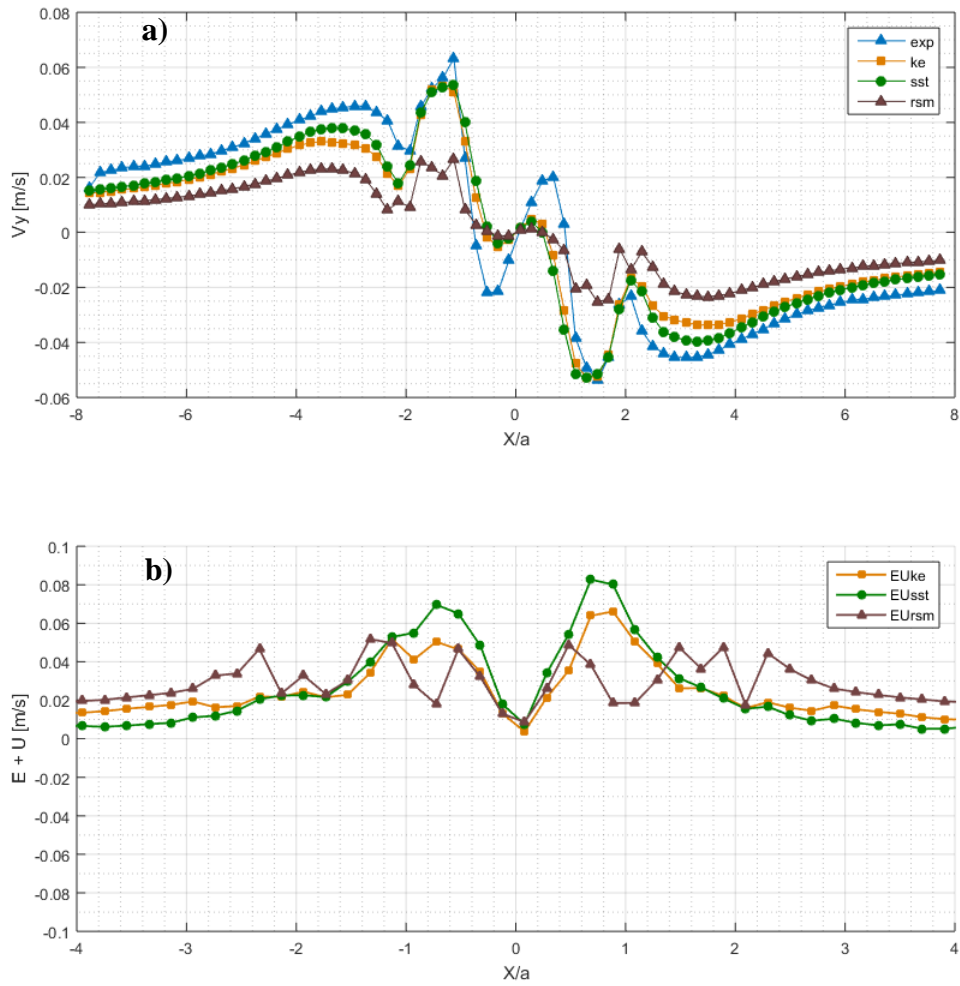
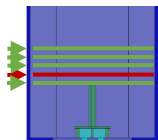


Fig. 5.24 Uniform Velocity inlet case a) V_x velocity profiles – models comparison b) Validation absolute modelling error + validation Uncertainty

UNIFORM	KE	SST	RSM
Pav	1.28	1.34	1.4642
Pstd	0.39	0.40	0.4462
GCI_{mean} %	0.75	2.07	0.2541
GCI_{max} %	2.27	7.12	0.6852
 E [m/s]	0.0091	0.0077	0.0176
 E _{MAX} [m/s]	0.0313	0.0383	0.0366
U[m/s]	0.0036	0.0040	0.0025
U_{num}[m/s]	0.0026	0.0031	0.0013
U_{exp}[m/s]	0.0031	0.0031	0.0031
 E +U[m/s]	0.0127	0.0113	0.0201

Tab. 5.12 Uniform Velocity inlet case V&V



V_x at $Y/a = 4.2$

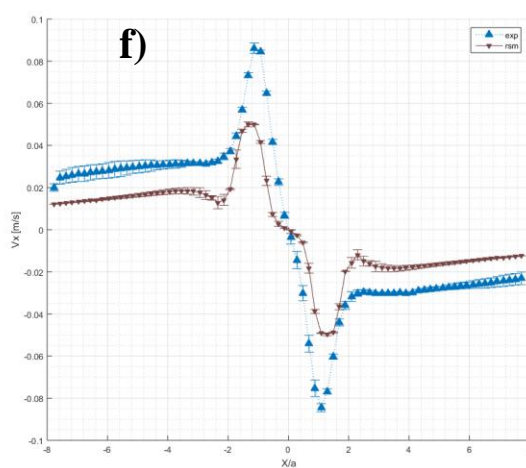
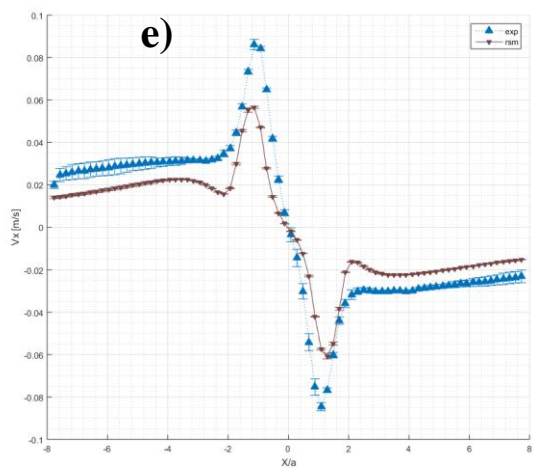
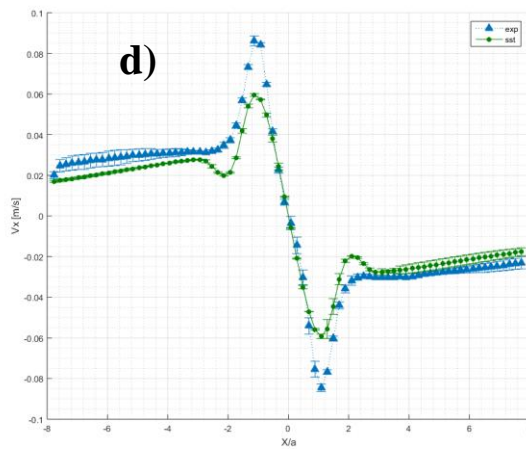
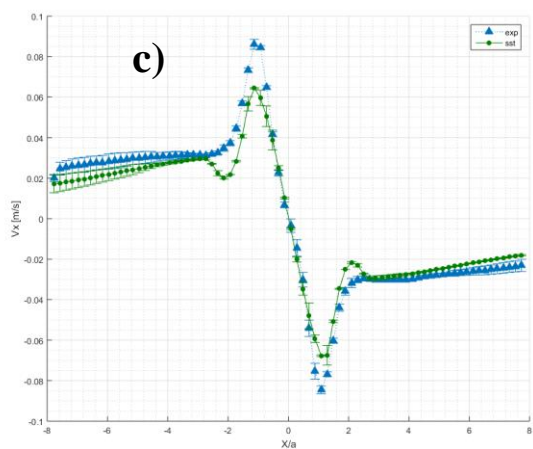
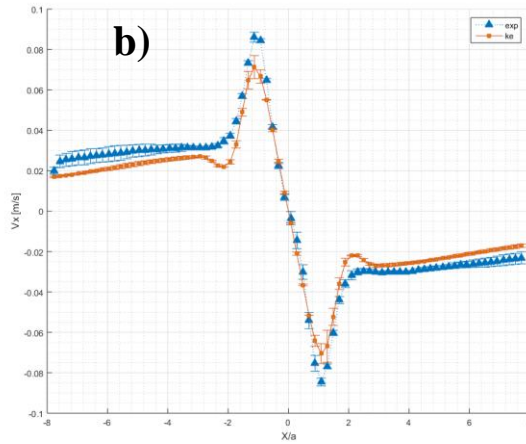
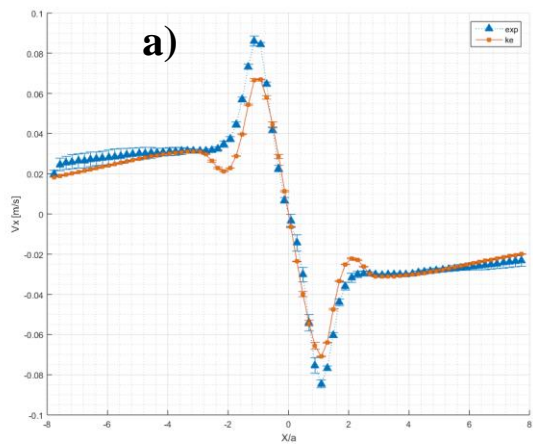


Fig. 5.25 V_x velocities profiles: a) ke Exp. B.C. b) ke Unif. B.C. c) sst Exp. B.C. d) sst Unif. B.C. e) rsm Exp. B.C. f) rsm Unif. B.C.

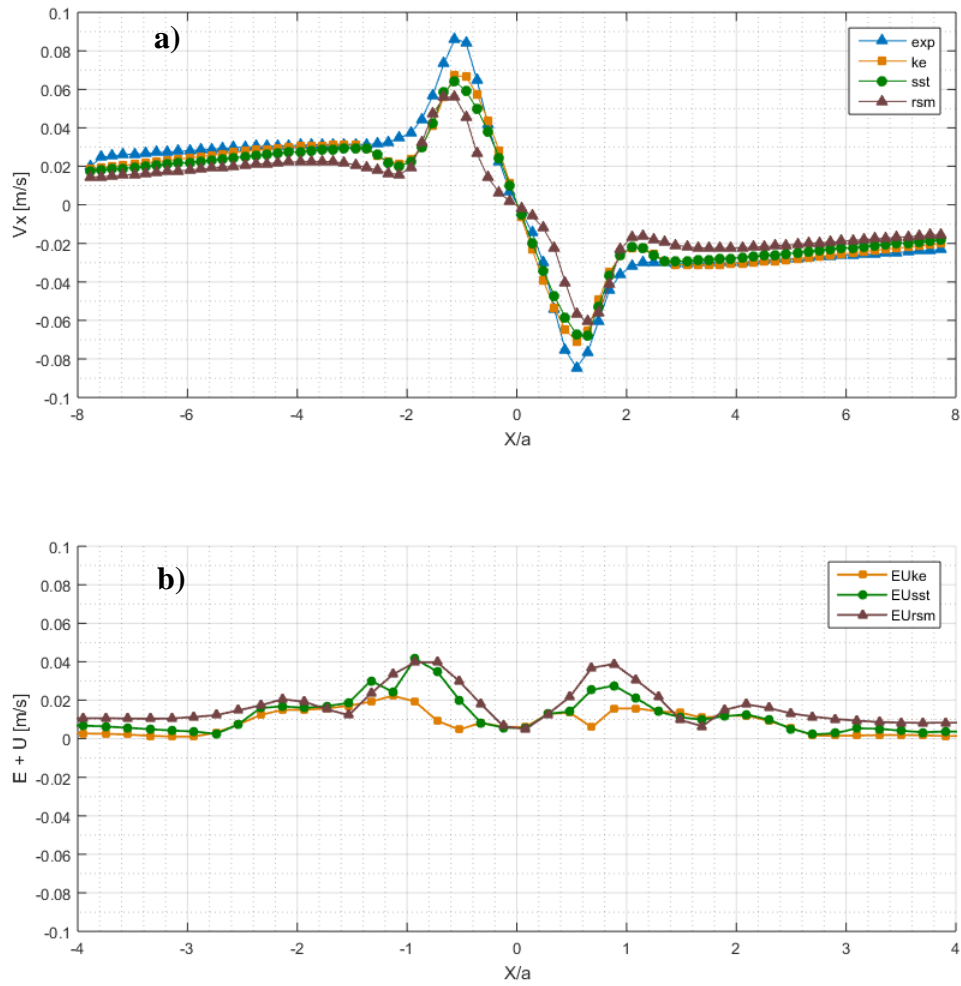


Fig. 5.26 Experimental Velocity inlet case a) V_x velocity profiles – models comparison b) Validation absolute modelling error + validation Uncertainty

EXP	KE	SST	RSM
Pav	1.94	1.46	1.36
Pstd	0.12	0.48	0.47
GCI_{mean} %	1.84	0.81	1.70
GCI_{max} %	3.87	1.96	3.20
 E [m/s]	0.0046	0.0060	0.0117
 E _{MAX} [m/s]	0.0189	0.0252	0.0383
U[m/s]	0.0019	0.0023	0.0019
U_{num}[m/s]	0.0001	0.0010	0.0002
U_{exp}[m/s]	0.0030	0.0030	0.0030
 E +U[m/s]	0.0065	0.0080	0.0137

Tab. 5.13 Experimental Velocity inlet case V&V

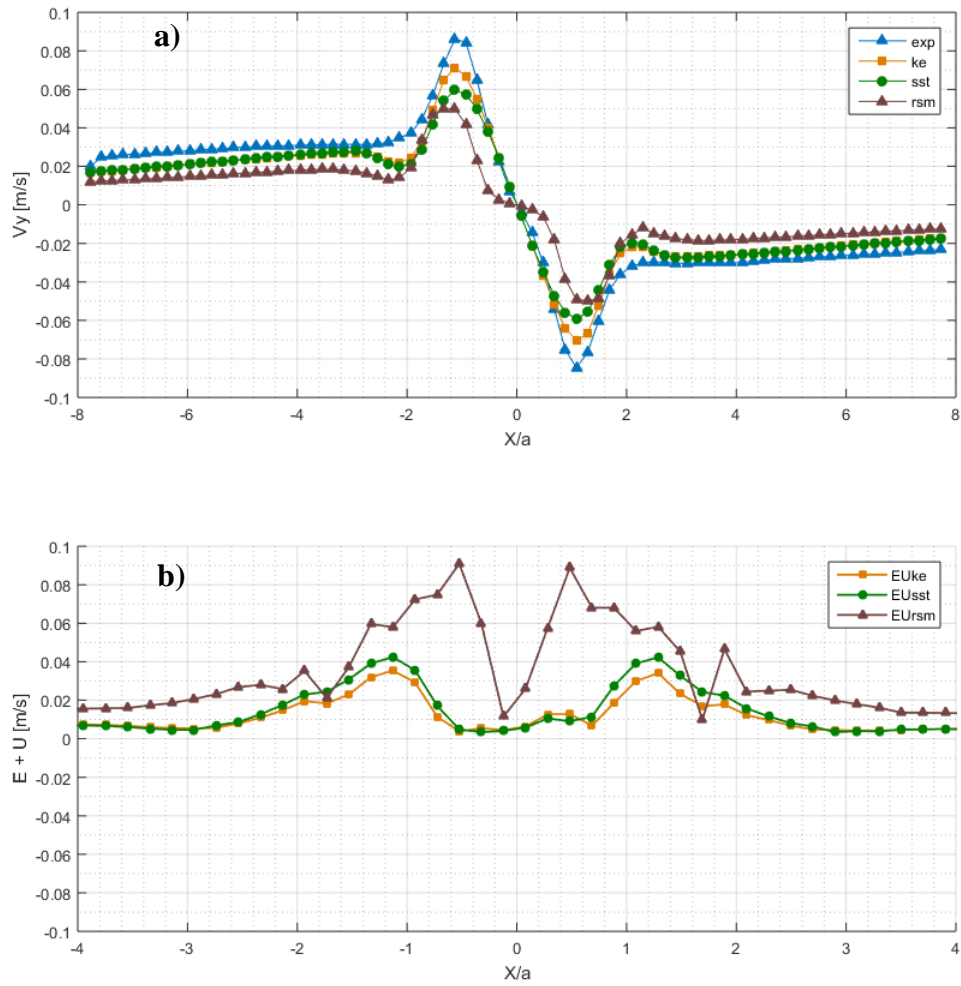
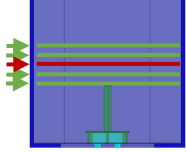


Fig. 5.27 Uniform Velocity inlet case a) V_x velocity profiles – models comparison b) Validation absolute modelling error + validation Uncertainty

CALC	KE	SST	RSM
Pav	1.21	1.35	1.11
Pstd	0.36	0.42	0.20
GCI_{mean} %	1.13	2.22	1.85
GCI_{max} %	1.83	4.62	2.83
 E [m/s]	0.0065	0.0077	0.0154
 E _{MAX} [m/s]	0.0177	0.0269	0.0427
U[m/s]	0.0025	0.0024	0.0044
U_{num}[m/s]	0.0009	0.0010	0.0032
U_{exp}[m/s]	0.0030	0.0030	0.0030
 E +U[m/s]	0.0090	0.0102	0.0198

Tab. 5.14 Uniform Velocity inlet case V&V



V_x at $Y/a = 7$

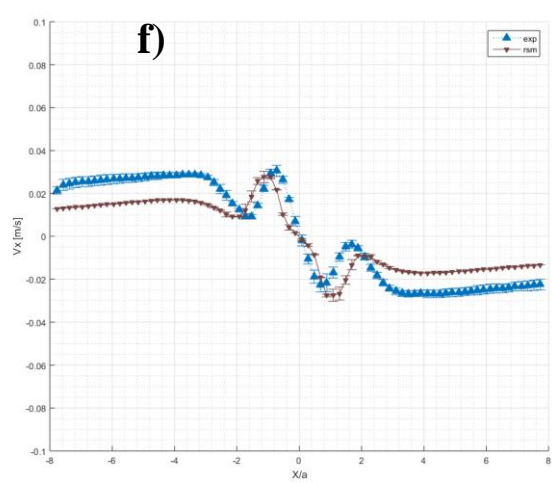
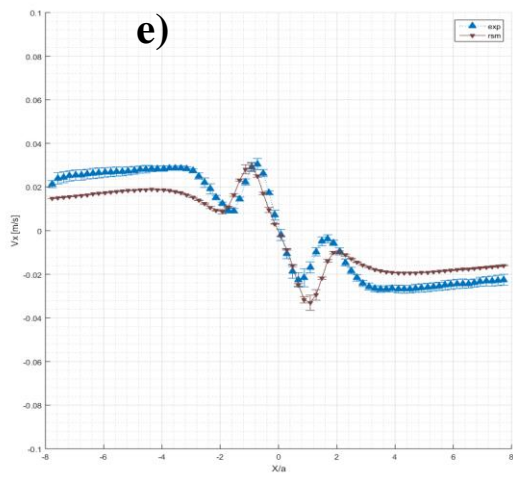
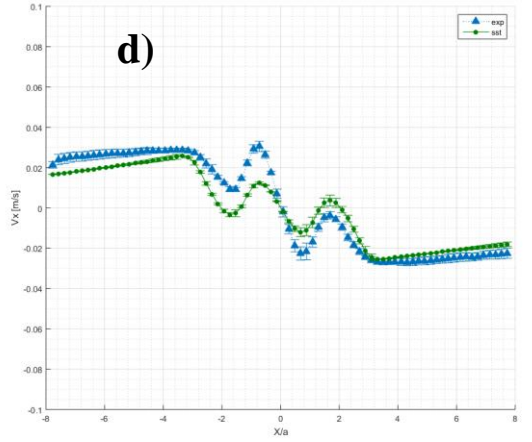
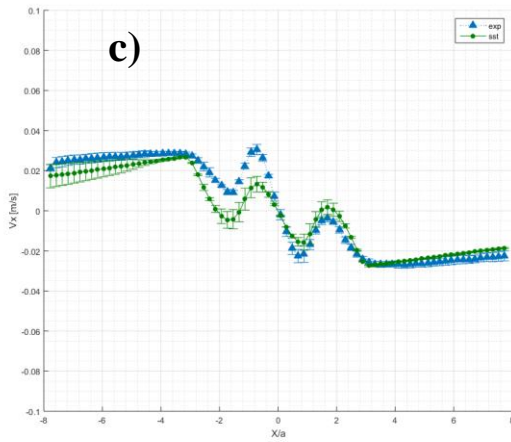
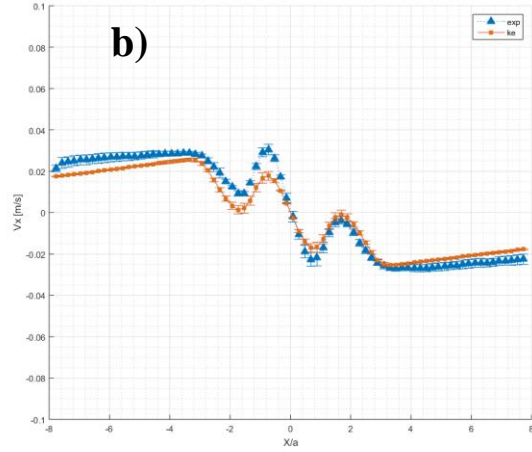
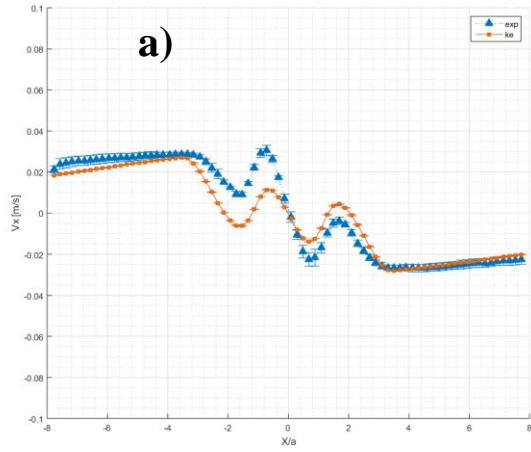


Fig. 5.28 V_x velocities profiles: a) ke Exp. B.C. b) ke Unif. B.C. c) sst Exp. B.C. d) sst Unif. B.C. e) rsm Exp. B.C. f) rsm Unif. B.C.

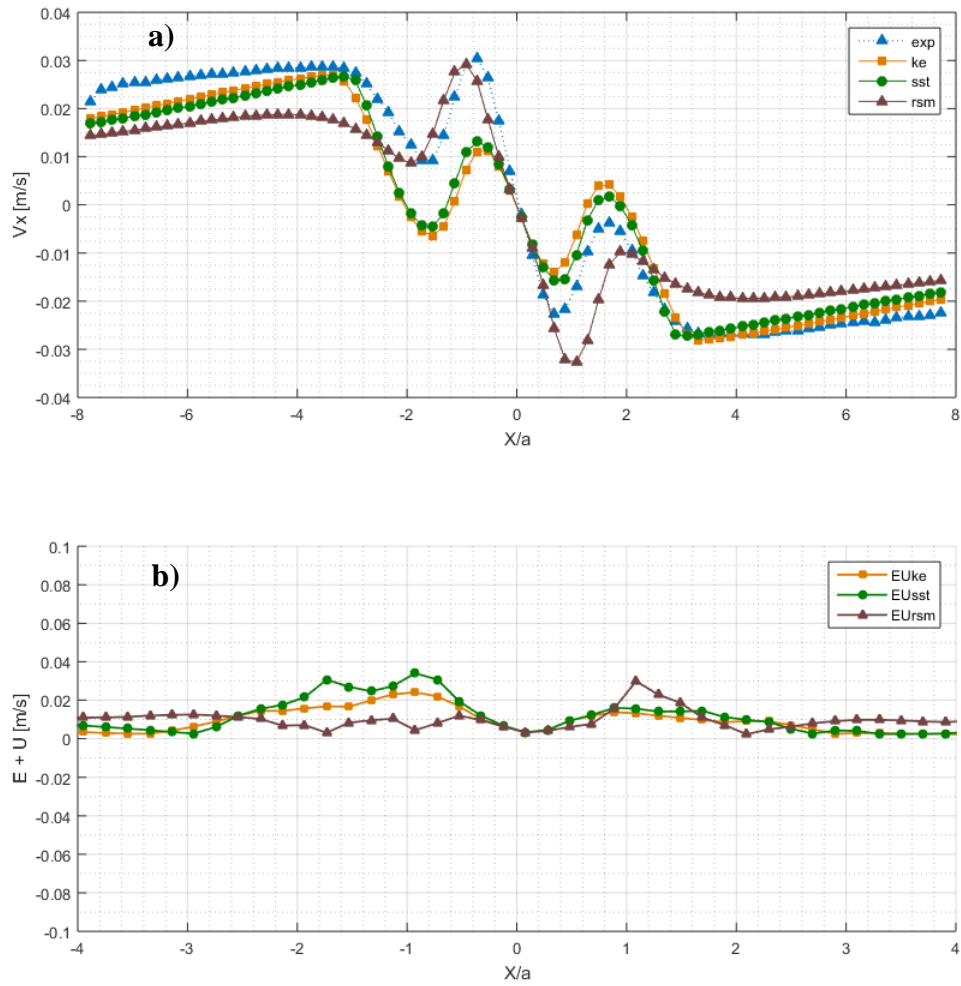


Fig. 5.29 Experimental Velocity inlet case a) V_x velocity profiles – models comparison b) Validation absolute modelling error + validation Uncertainty

EXPERIMENTAL	KE	SST	RSM
Pav	1.45	1.34	1.59
Pstd	0.32	0.45	0.46
GCI_{mean} %	1.70	1.15	0.38
GCI_{max} %	3.21	2.69	1.58
 E [m/s]	0.0055	0.0058	0.0078
 E _{MAX} [m/s]	0.0212	0.0177	0.0197
U[m/s]	0.0018	0.0026	0.0019
U_{num}[m/s]	0.0008	0.0015	0.0002
U_{exp}[m/s]	0.0037	0.0037	0.0037
 E +U[m/s]	0.0074	0.0073	0.0097

Tab. 5.15 Experimental Velocity inlet case V&V

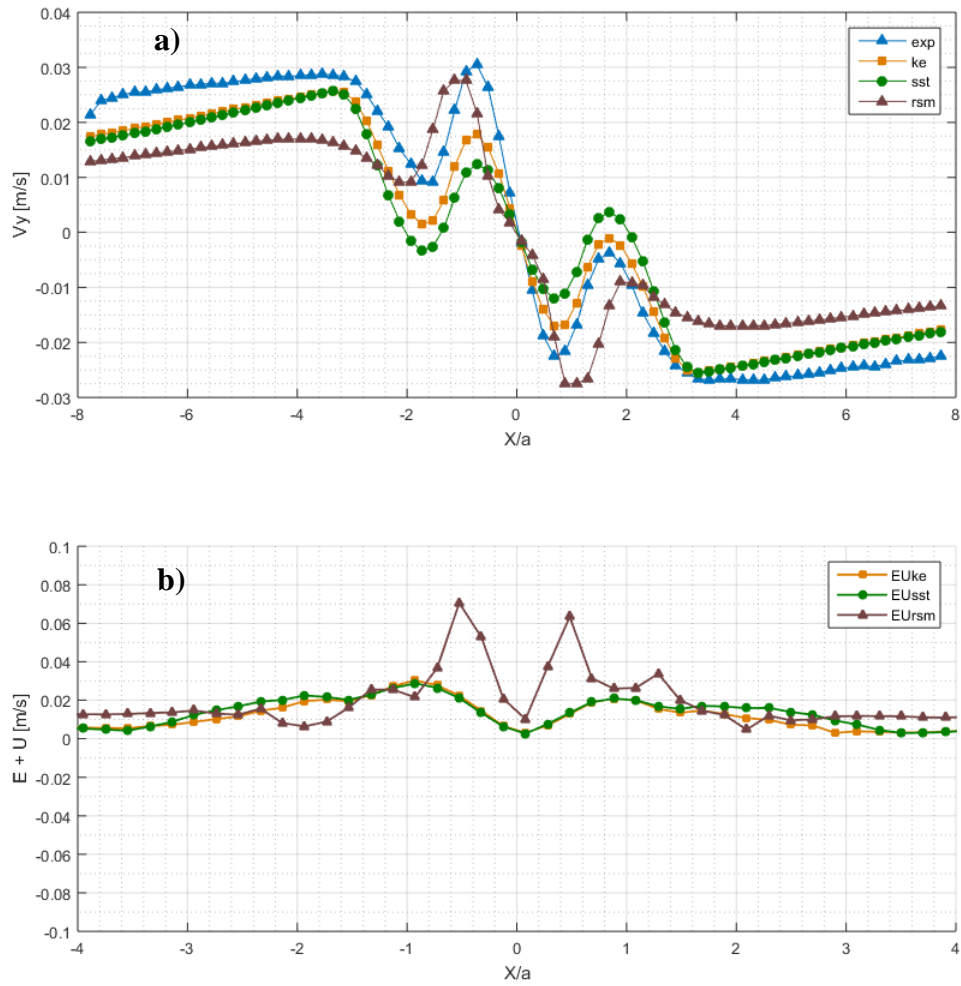
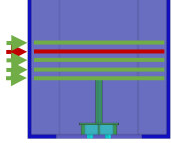


Fig. 5.30 Uniform Velocity inlet case a) V_x velocity profiles – models comparison b) Validation absolute modelling error + validation Uncertainty

UNIFORM	KE	SST	RSM
Pav	1.93	1.04	1.75
Pstd	0.12	0.13	0.25
GCImean %	0.81	1.75	1.65
GCImax %	1.24	2.73	2.28
 E [m/s]	0.0047	0.0064	0.0095
 E MAX [m/s]	0.0127	0.0184	0.0169
U[m/s]	0.0026	0.0024	0.0032
Unum[m/s]	0.0013	0.0011	0.0019
Uexp[m/s]	0.0037	0.0037	0.0037
 E +U[m/s]	0.0073	0.0090	0.0127

Tab. 5.16 Uniform Velocity inlet case V&V



V_x at $Y/a = 10$

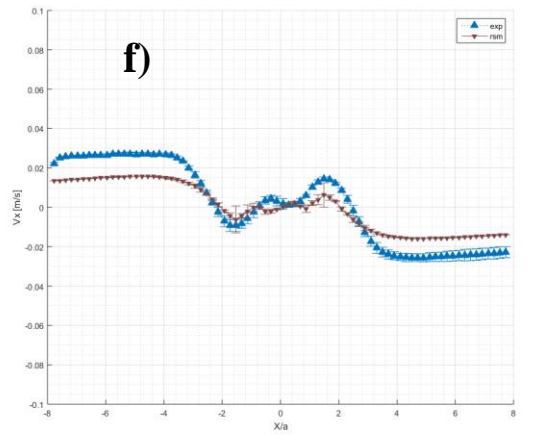
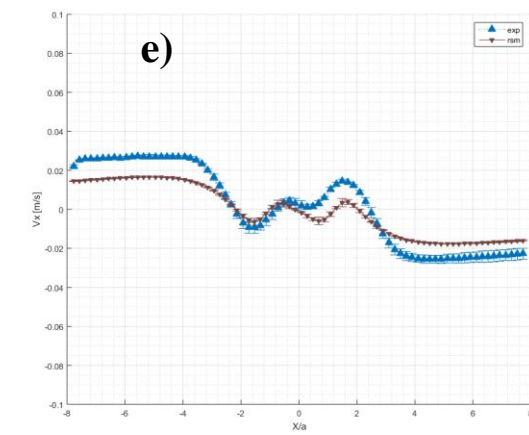
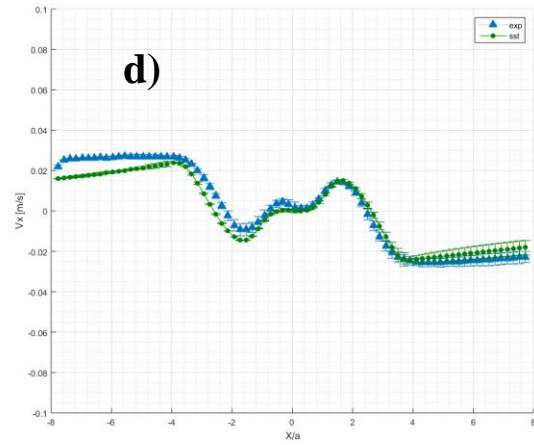
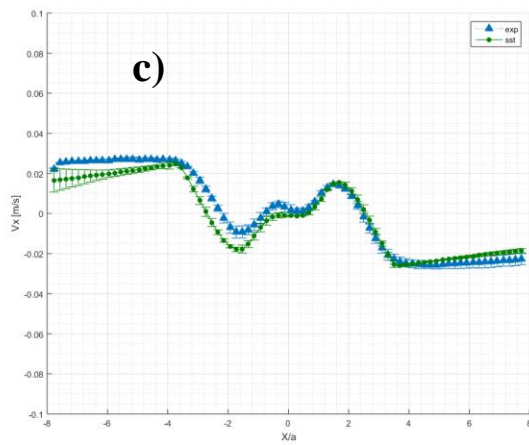
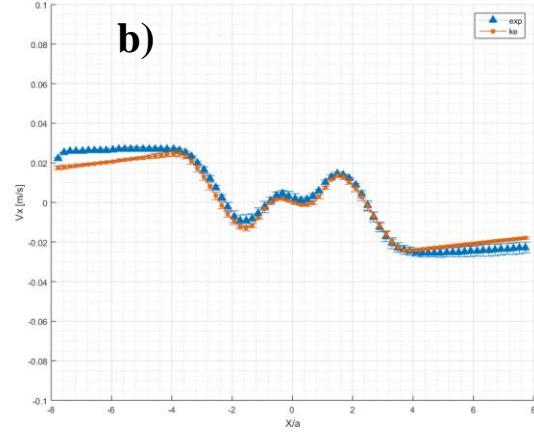
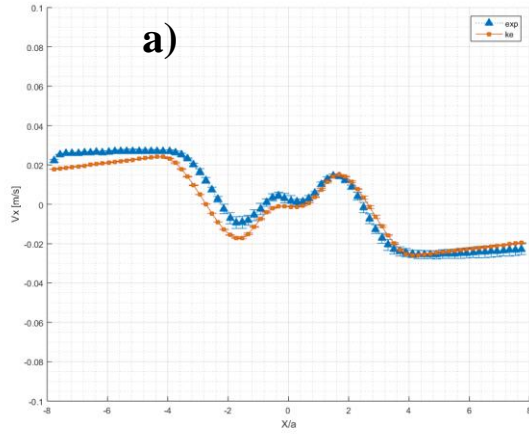


Fig. 5.31 V_x velocities profiles: a) ke Exp. B.C. b) ke Unif. B.C. c) sst Exp. B.C. d) sst Unif. B.C. e) rsm Exp. B.C. f) rsm Unif. B.C.

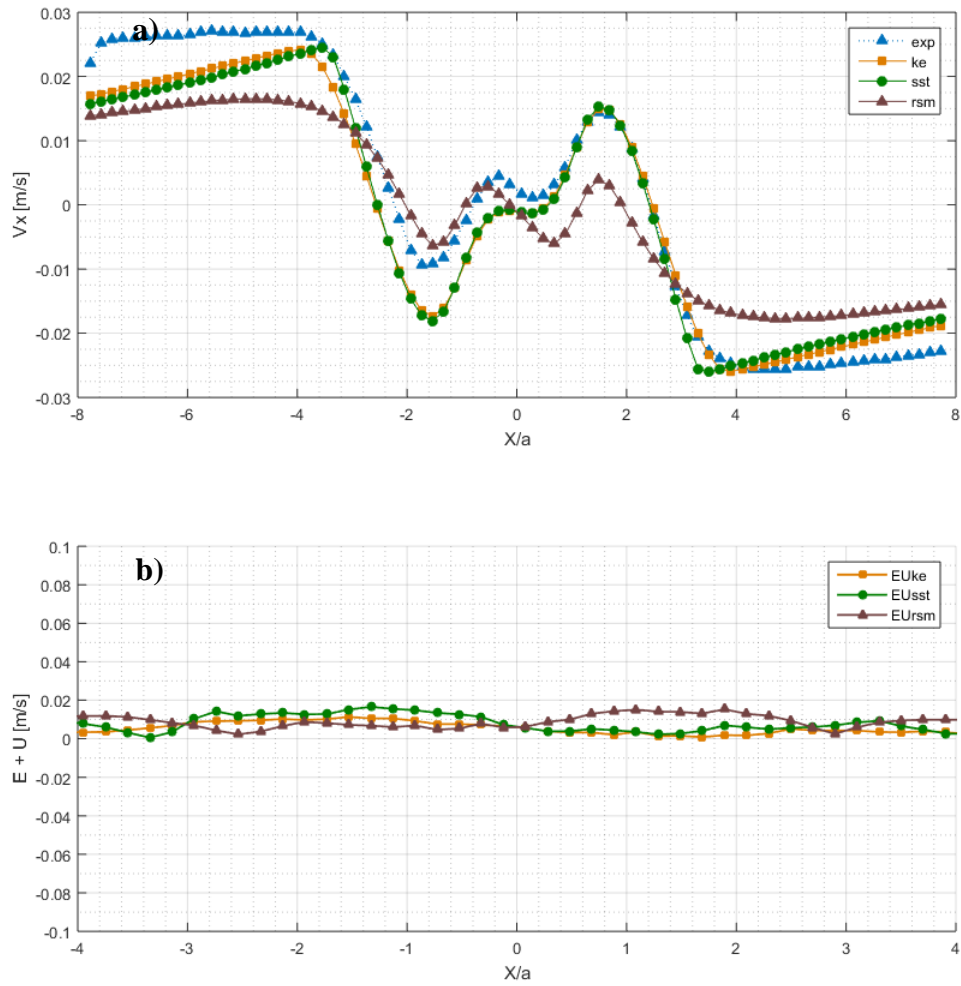


Fig. 5.32 Experimental Velocity inlet case a) V_x velocity profiles – models comparison b) Validation absolute modelling error + validation Uncertainty

EXPERIMENTAL	KE	SST	RSM
Pav	1.65	1.43	1.36
Pstd	0.32	0.42	0.23
GCI_{mean} %	1.24	0.98	0.90
GCI_{max} %	2.41	2.80	1.82
 E [m/s]	0.0039	0.0047	0.0077
 E _{MAX} [m/s]	0.0089	0.010	0.0126
U[m/s]	0.0016	0.0022	0.0017
U_{num}[m/s]	0.0001	0.0011	0.0003
U_{exp}[m/s]	0.0037	0.0037	0.0037
 E +U[m/s]	0.0057	0.0105	0.0100

Tab. 5.17 Experimental Velocity inlet case V&V

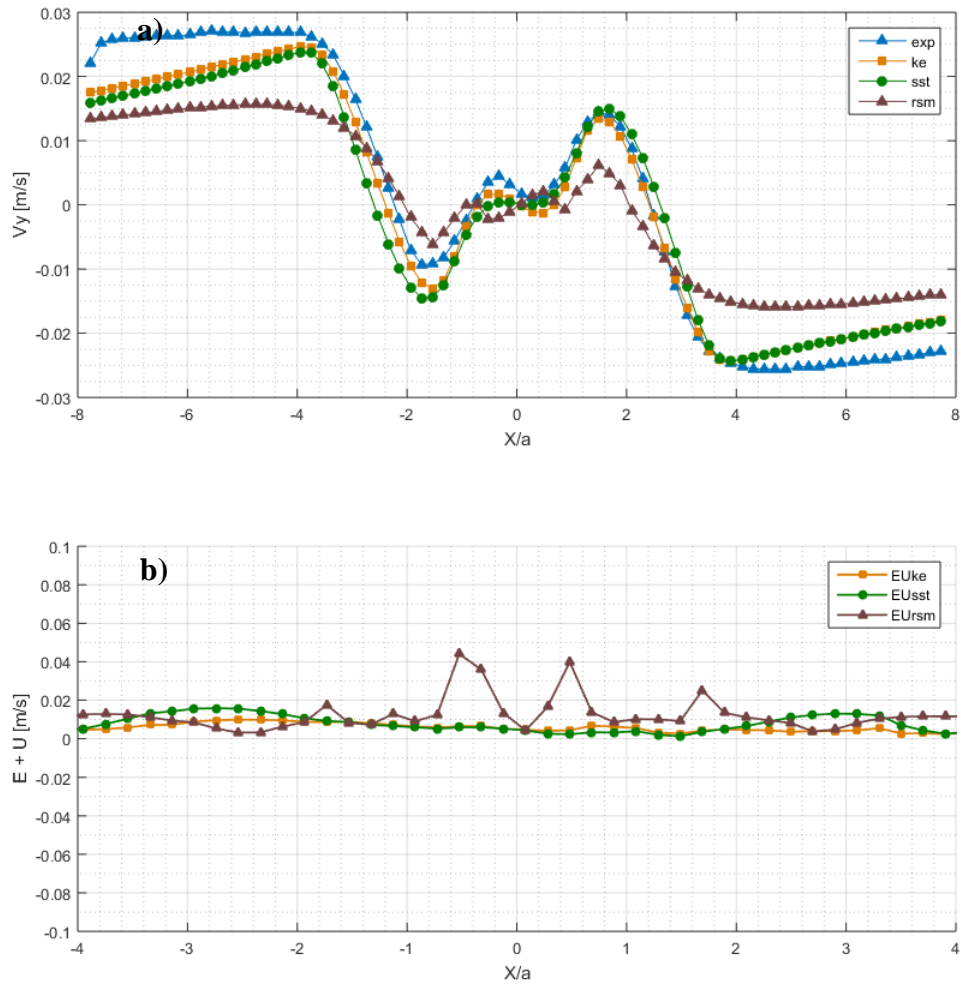
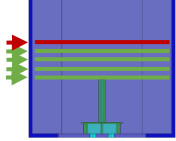


Fig. 5.33 Uniform Velocity inlet case a) V_x velocity profiles – models comparison b) Validation absolute modelling error + validation Uncertainty

UNIFORM	KE	SST	RSM
Pav	1.81	1.20	1.08
Pstd	0.37	0.37	0.26
GCI_{mean} %	0.84	1.81	0.71
GCI_{max} %	1.23	2.60	1.36
 E [m/s]	0.0032	0.0043	0.0079
 E _{MAX} [m/s]	0.0076	0.0092	0.0120
U[m/s]	0.0018	0.0020	0.0023
U_{num}[m/s]	0.0006	0.0008	0.0010
U_{exp}[m/s]	0.0037	0.0037	0.0037
 E +U[m/s]	0.0051	0.0062	0.0103

Tab. 5.18 Uniform Velocity inlet case V&V



V_x at $Y/a = 11.5$

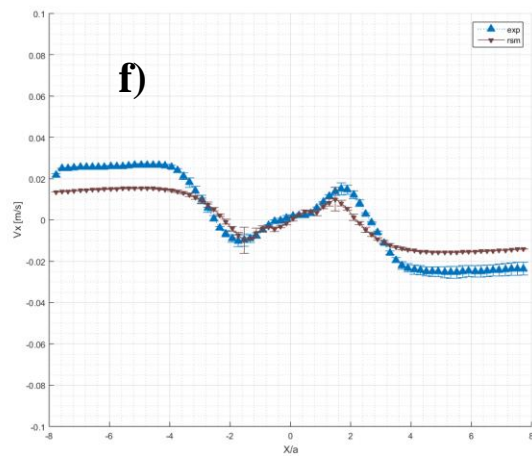
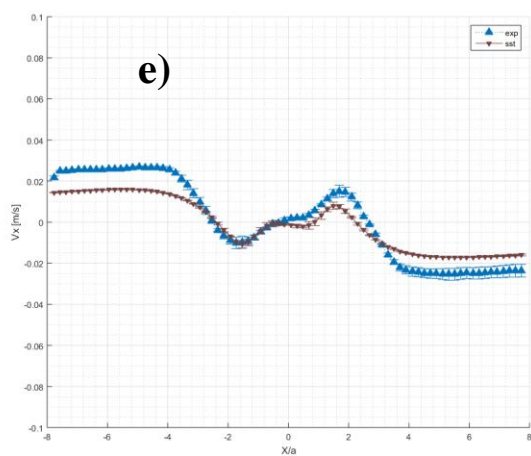
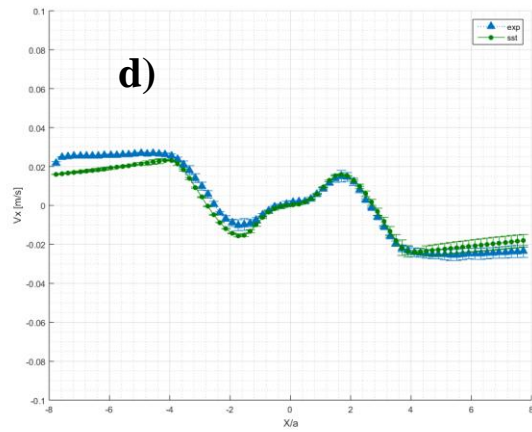
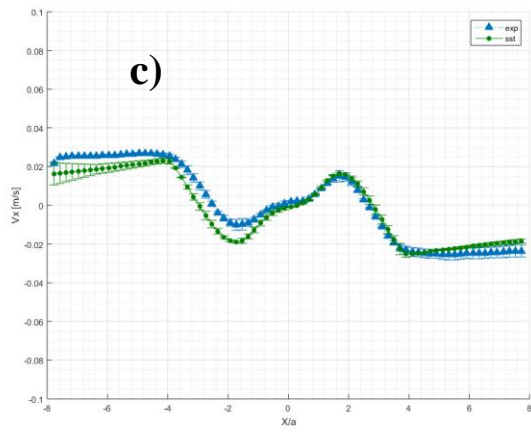
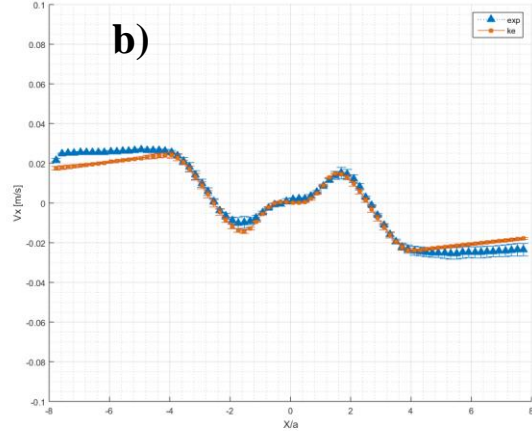
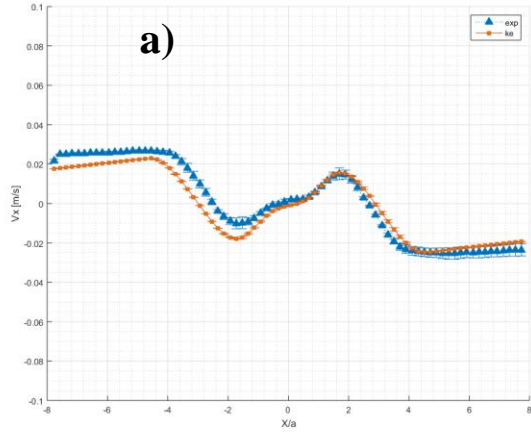


Fig. 5.34 V_x velocities profiles: a) ke Exp. B.C. b) ke Unif. B.C. c) sst Exp. B.C. d) sst Unif. B.C. e) rsm Exp. B.C. f) rsm Unif. B.C.

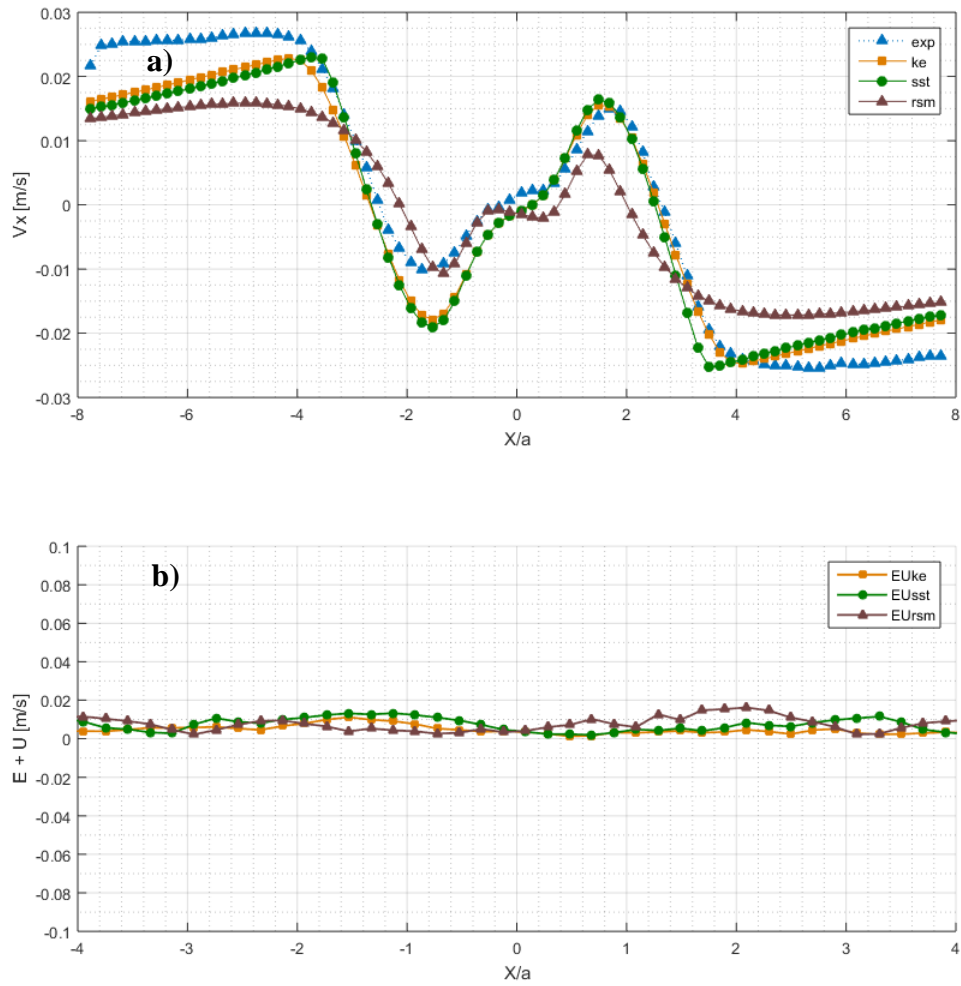


Fig. 5.35 Experimental Velocity inlet case a) V_x velocity profiles – models comparison b) Validation absolute modelling error + validation Uncertainty

EXPERIMENTAL	KE	SST	RSM
Pav	1.65	1.44	1.52
Pstd	0.32	0.43	0.27
GCI_{mean} %	1.30	1.04	0.75
GCI_{max} %	2.84	2.81	2.10
 E [m/s]	0.0038	0.0044	0.0070
 E _{MAX} [m/s]	0.0081	0.0092	0.0127
U [m/s]	0.0014	0.0021	0.001572
U_{num} [m/s]	0.0001	0.0011	0.000344
U_{exp} [m/s]	0.0040	0.0040	0.004039
 E +U [m/s]	0.0055	0.0103	0.0091

Tab. 5.19 Experimental Velocity inlet case V&V

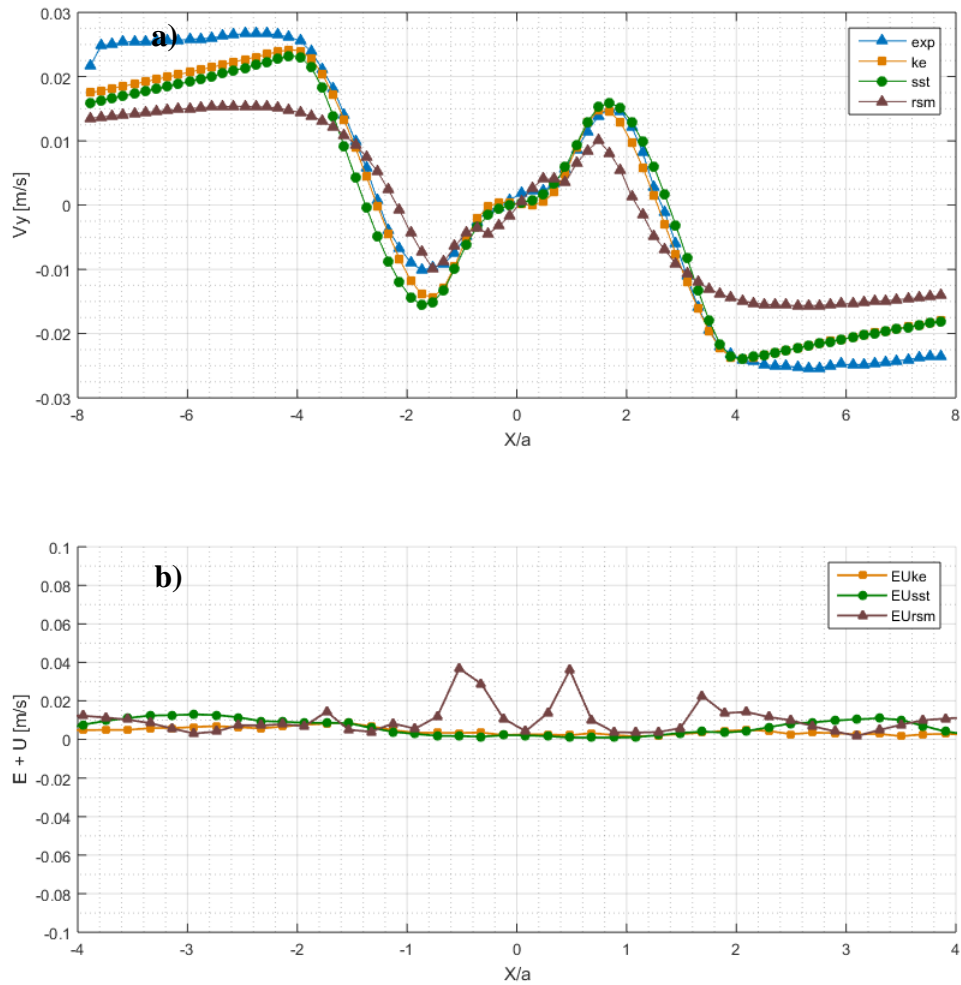


Fig. 5.36 Uniform Velocity inlet case a) V_x velocity profiles – models comparison b) Validation absolute modelling error + validation Uncertainty

UNIFORM	KE	SST	RSM
Pav	1.77	1.22	1.22
Pstd	0.41	0.32	0.37
GClmean %	0.83	1.67	0.62
GClmax %	1.24	3.02	1.11
E [m/s]	0.0027	0.0036	0.0071
E MAX [m/s]	0.0070	0.0085	0.0113
U [m/s]	0.0016	0.0018	0.0021
U _{num} [m/s]	0.0005	0.0007	0.0009
U _{exp} [m/s]	0.0040	0.0040	0.0040
E +U [m/s]	0.0043	0.0052	0.0092

Tab. 5.20 Uniform Velocity inlet case V&V

Reynolds Stress Tensor components at $Y/a = 1.4$

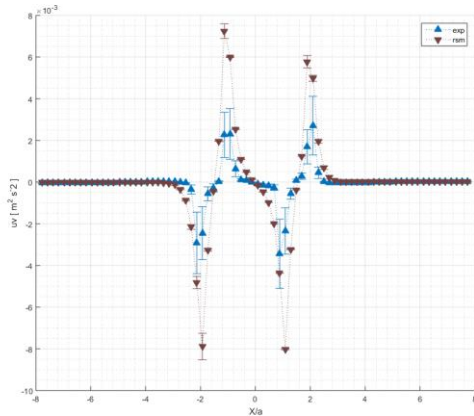
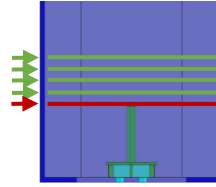


Fig. 5.37 Experimental BC – Rs

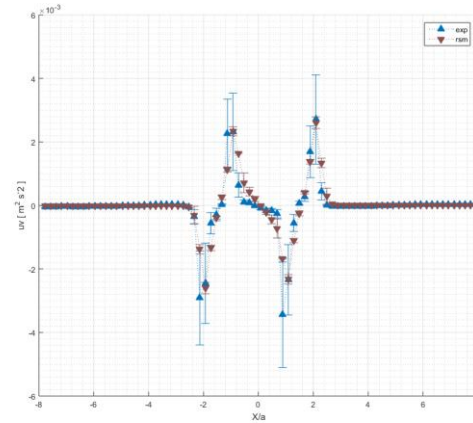


Fig. 5.38 Uniform BC – Rs

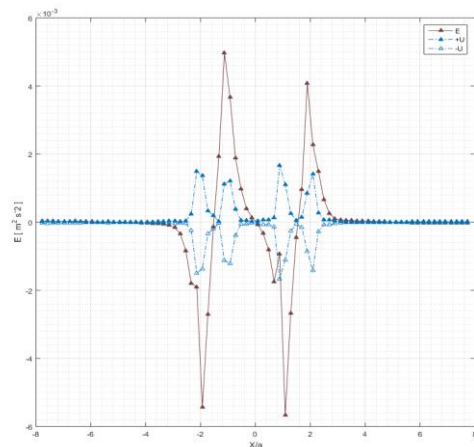


Fig. 5.39 Experimental BC – E, ±U

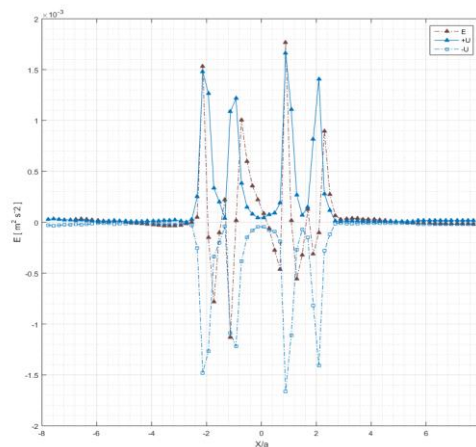


Fig. 5.40 Uniform BC – E, ±U

EXPERIMENTAL	RSM
$ E [m^2 s^{-2}]$	0.000661
$U [m^2 s^{-2}]$	0.000177
$U_{num} [m^2 s^{-2}]$	2.7E-05
$U_{exp} [m^2 s^{-2}]$	0.000171
$ E +U [m^2 s^{-2}]$	0.000838

Tab. 5.21 V&V – Experimental BC

UNIFORM	RSM
$ E [m^2 s^{-2}]$	0.000162
$U [m^2 s^{-2}]$	0.000177
$U_{num} [m^2 s^{-2}]$	1.85557E-05
$U_{exp} [m^2 s^{-2}]$	0.000171167
$ E +U [m^2 s^{-2}]$	0.000338308

Tab. 5.22 V&V – Uniform BC - Rs

Reynolds Stress Tensor components at $Y/a = 4.2$

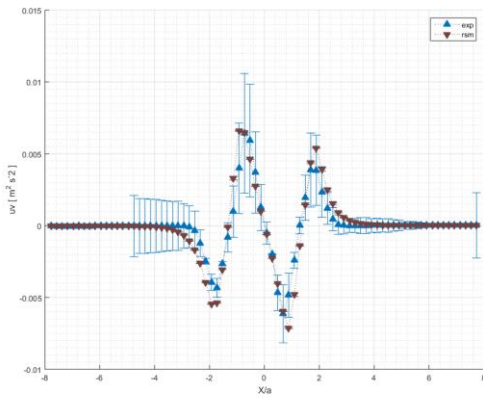
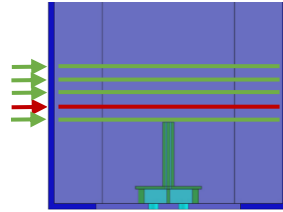


Fig. 5.41 Experimental BC – Rs

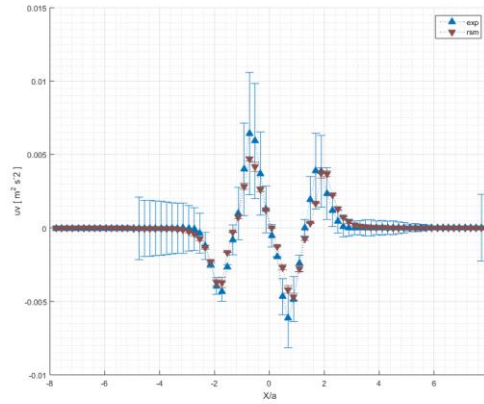


Fig. 5.42 Uniform BC – Rs

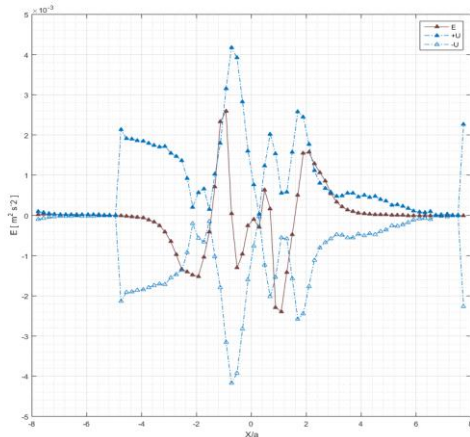


Fig. 5.43 Experimental BC – E, ±U

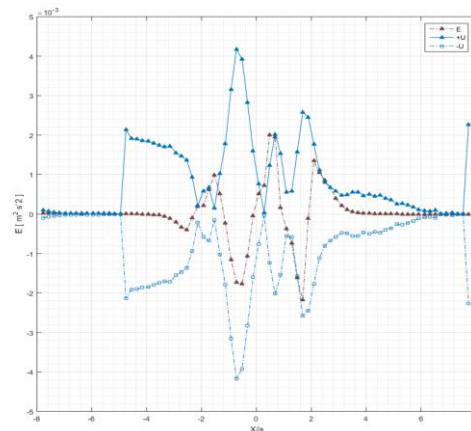


Fig. 5.44 Uniform BC – E, ±U

EXPERIMENTAL	RSM
$ E [m^2 s^{-2}]$	0.000448
$U [m^2 s^{-2}]$	0.000881
$U_{num} [m^2 s^{-2}]$	1.2E-05
$U_{exp} [m^2 s^{-2}]$	0.000880263
$ E +U [m^2 s^{-2}]$	0.00132893

Tab. 5.23 V&V – Experimental BC

UNIFORM	RSM
$ E [m^2 s^{-2}]$	0.000329
$U [m^2 s^{-2}]$	0.000881
$U_{num} [m^2 s^{-2}]$	2.88E-05
$U_{exp} [m^2 s^{-2}]$	0.00088
$ E +U [m^2 s^{-2}]$	0.00121

Tab. 5.24 V&V – Uniform BC - Rs

Reynolds Stress Tensor components at $Y/a = 7a$

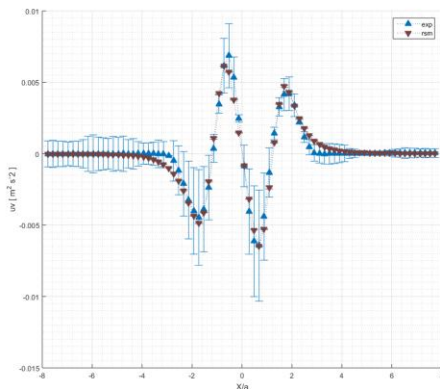
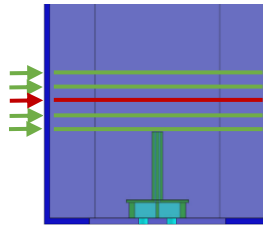


Fig. 5.45 Experimental BC – R_s

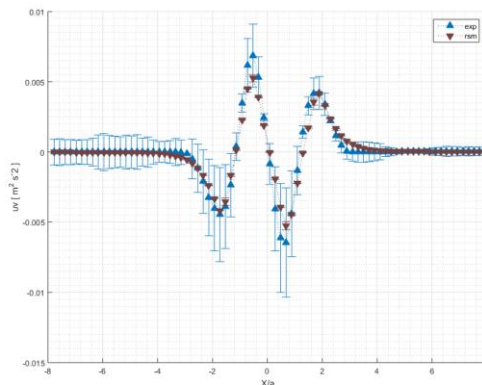


Fig. 5.46 Uniform BC – R_s

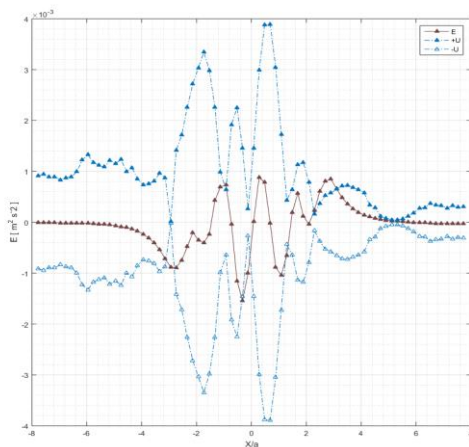


Fig. 5.47 Experimental BC – $E, \pm U$

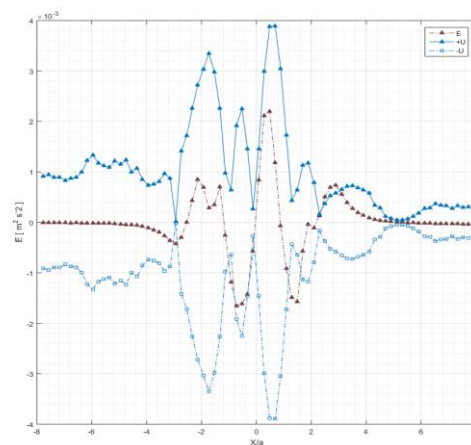


Fig. 5.48 Uniform BC – $E, \pm U$

EXPERIMENTAL	RSM
$ \mathbf{E} [m^2 s^{-2}]$	0.0003
$\mathbf{U} [m^2 s^{-2}]$	0.001058
$\mathbf{U}_{\text{unum}} [m^2 s^{-2}]$	8.66E-06
$\mathbf{U}_{\text{exp}} [m^2 s^{-2}]$	0.001058
$ \mathbf{E} +\mathbf{U} [m^2 s^{-2}]$	0.001357

Tab. 5.25 V&V – Experimental BC

UNIFORM	RSM
$ \mathbf{E} [m^2 s^{-2}]$	0.000356
$\mathbf{U} [m^2 s^{-2}]$	0.001058
$\mathbf{U}_{\text{unum}} [m^2 s^{-2}]$	1.23E-05
$\mathbf{U}_{\text{exp}} [m^2 s^{-2}]$	0.001058
$ \mathbf{E} +\mathbf{U} [m^2 s^{-2}]$	0.001414

Tab. 5.26 V&V – Uniform BC - R_s

Reynolds Stress Tensor components at $Y/a = 10$

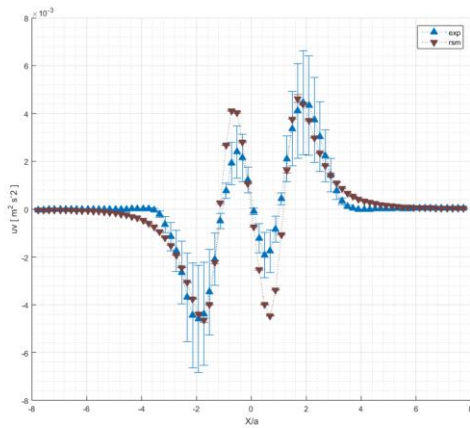
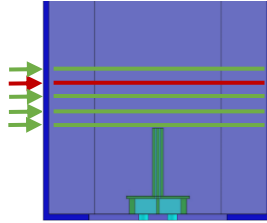


Fig. 5.49 Experimental BC – R_s

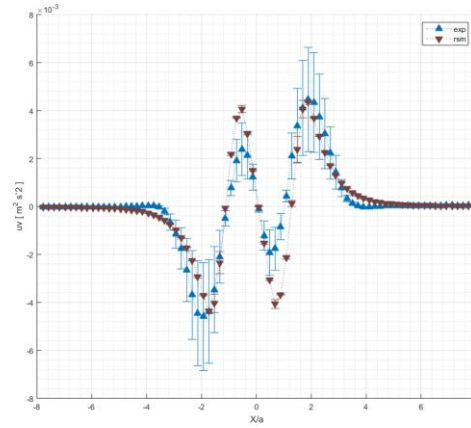


Fig. 5.50 Uniform BC – R_s

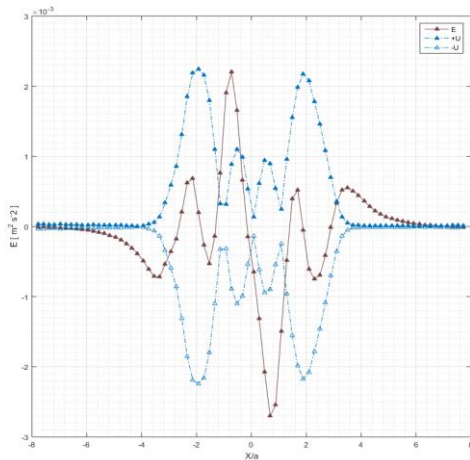


Fig. 5.51 Experimental BC – $E, \pm U$

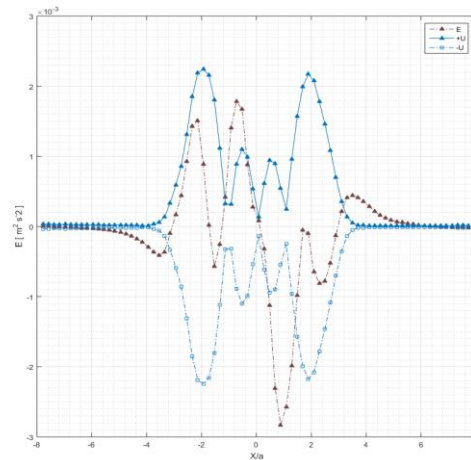


Fig. 5.52 Uniform BC – $E, \pm U$

EXPERIMENTAL	RSM
$ E [m^2 s^{-2}]$	0.000444
$U [m^2 s^{-2}]$	0.000483
$U_{num} [m^2 s^{-2}]$	1.17E-05
$U_{exp} [m^2 s^{-2}]$	0.000482
$ E +U [m^2 s^{-2}]$	0.000927

Tab. 5.27 V&V – Experimental BC

UNIFORM	RSM
$ E [m^2 s^{-2}]$	0.000435
$U [m^2 s^{-2}]$	0.000484
$U_{num} [m^2 s^{-2}]$	2.07E-05
$U_{exp} [m^2 s^{-2}]$	0.000482136
$ E +U [m^2 s^{-2}]$	0.00091902

Tab. 5.28 V&V – Uniform BC - R_s

Reynolds Stress Tensor components at $Y/a = 11.5$

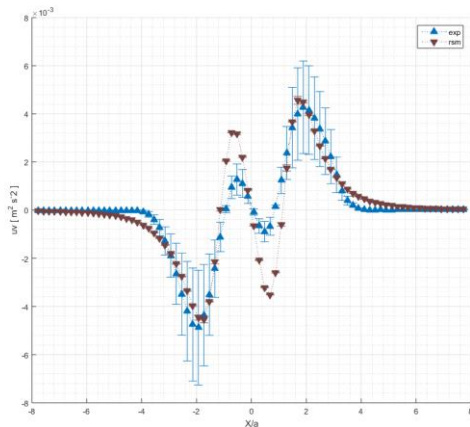
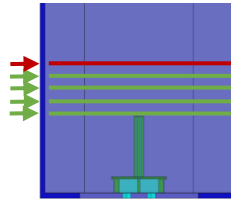


Fig. 5.53 Experimental BC – Rs

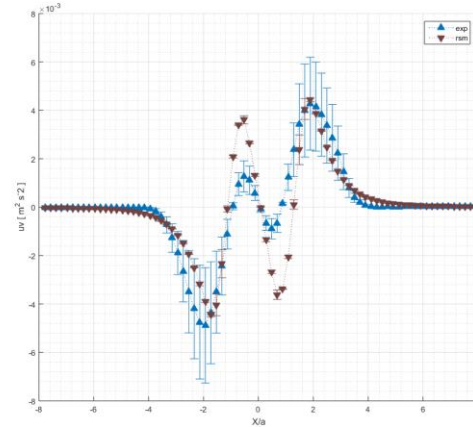


Fig. 5.54 Uniform BC – Rs

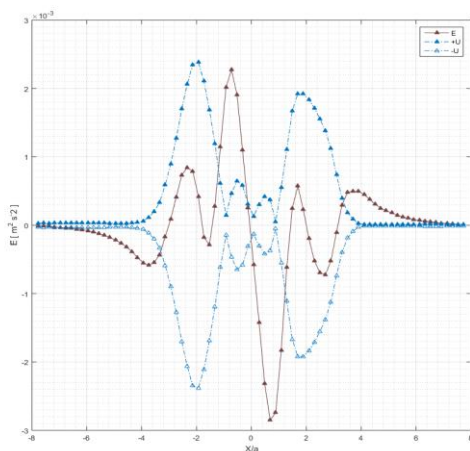


Fig. 5.55 Experimental BC – E, $\pm U$

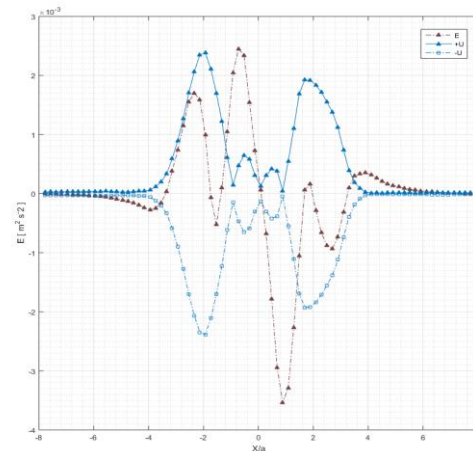


Fig. 5.56 Uniform BC – E, $\pm U$

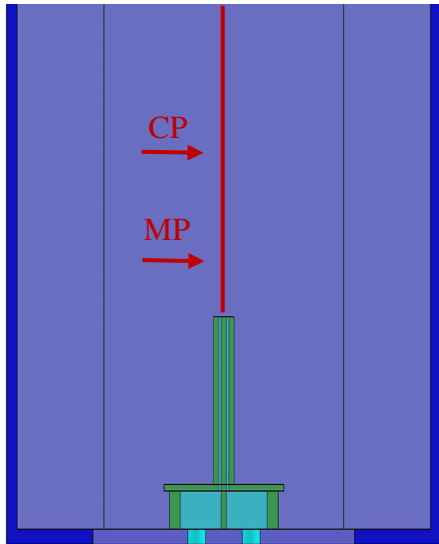
EXPERIMENTAL	RSM
$ E [m^2 s^{-2}]$	0.000494
$U [m^2 s^{-2}]$	0.000494
$U_{num} [m^2 s^{-2}]$	1.51E-05
$U_{exp} [m^2 s^{-2}]$	0.000493292
$ E +U [m^2 s^{-2}]$	0.000988325

Tab. 5.29 V&V – Experimental BC

UNIFORM	RSM
$ E [m^2 s^{-2}]$	0.000562
$U [m^2 s^{-2}]$	0.000496
$U_{num} [m^2 s^{-2}]$	2.54E-05
$U_{exp} [m^2 s^{-2}]$	0.000493292
$ E +U [m^2 s^{-2}]$	0.001057405

Tab. 5.30 V&V – Uniform BC - Rs

Merging Point (MP) and Combining Point (CP)



Experiments
$CP_{LDA} = \sim 15.52 \text{ a}$
$CP_{PIV} = \sim 16.84 \text{ a}$

Tab. 5.31 Converging Point Position LDA-PIV measurements

Experiments
$MP_{LDA} = 1.72 \text{ a} \sim 3.45 \text{ a}$
$MP_{PIV} = 2.66 \text{ a} \sim 3.15 \text{ a}$

Tab. 5.32 Merging Point Position LDA-PIV measurements

Figure 5.57 Merging and Converging Points

Uniform Inlet Velocity Profile

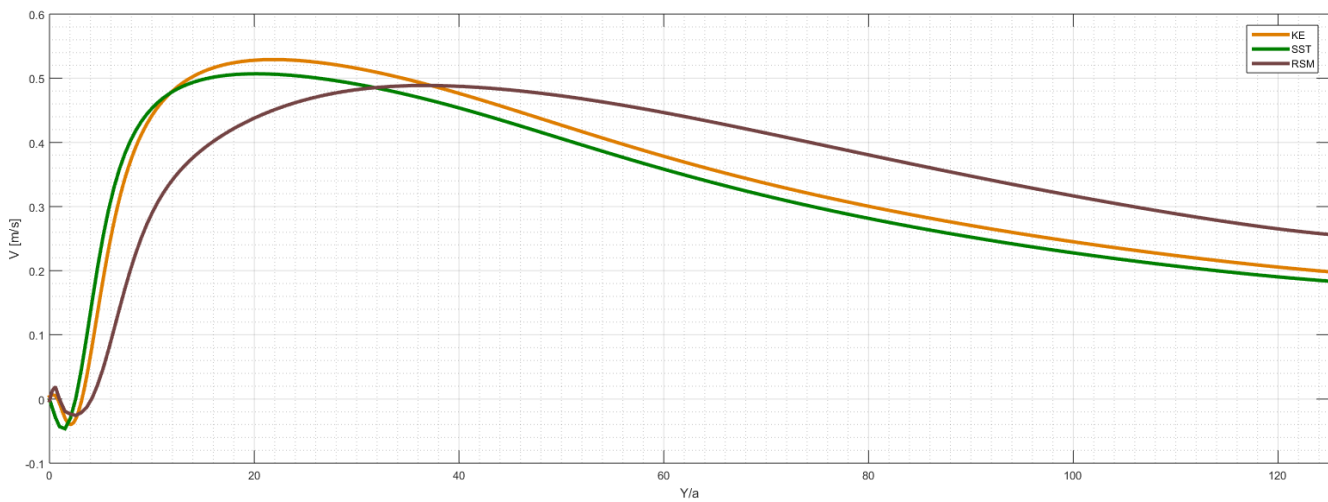


Figure 5.58 Axial Velocity profile - ke/sst/rsm models

Uniform	MP [Y/a]	p	GCI %
KE	3.11	4.18	1.17
SST	2.57	9.13	1.4
RSM	4.172	3.61	2.73

Uniform	CP [Y/a]	p	GCI %
KE	21.5	0.85	1.7
SST	20.13	2.64	0.18
RSM	36.31	7.65	0.44

Experimental Inlet Velocity Profile

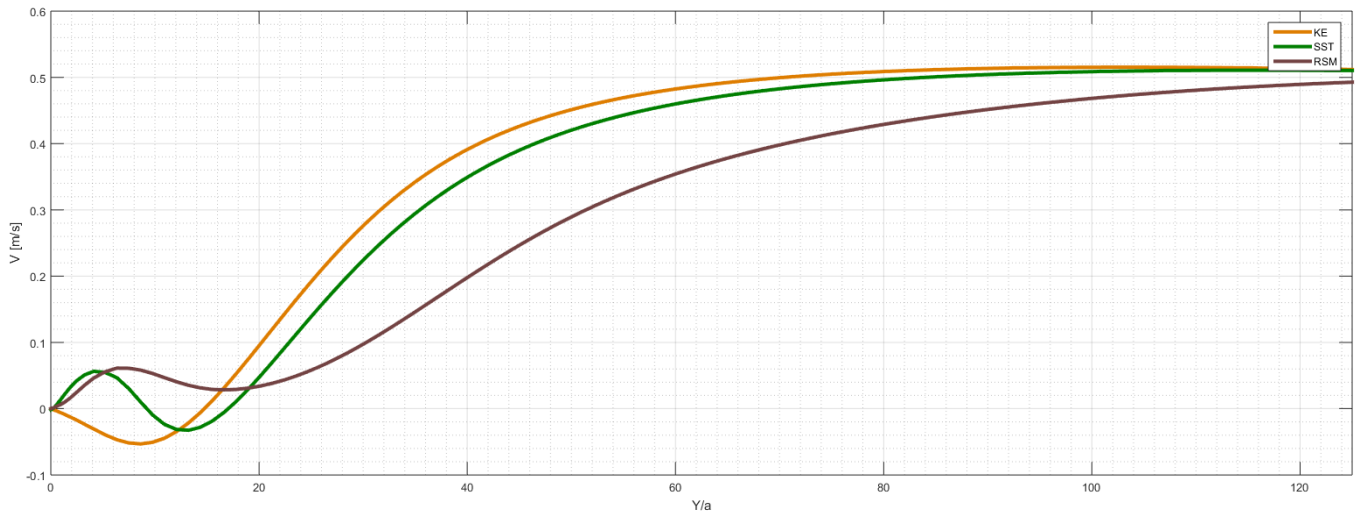


Figure 5.59 Axial Velocity profile - ke/sst/rsm models

Experimental	MP [Y/a]	p	GCI %
KE	15.3	6.27	7
SST	9.3	4.88	3.5
RSM	x	x	x

Experimental	CP [Y/a]	p	GCI %
KE	91.09	3.5	4.4
SST	112.9	1.72	1.61
RSM	124.3	3.31	2.3

Summary

Average Absolute error $|E|$ [m/s]

$$|E|_{ave} = \frac{1}{\Delta x} \int |E|(x) dx$$

V_y	Y/a = 1.4	Y/a = 4.2	Y/a = 7	Y/a = 10	Y/a = 11.5
K-eps EXP	0.0209	0.0135	0.0115	0.0121	0.0122
K-eps UNI	0.0207	0.0124	0.0119	0.0135	0.0127
SST EXP	0.0181	0.0190	0.0133	0.0139	0.0137
SST UNI	0.0236	0.0173	0.0166	0.0185	0.0168
RSM EXP	0.0244	0.0264	0.0319	0.0350	0.0360
RSM UNI	0.0158	0.0310	0.0399	0.0424	0.0455

Tab. 5.33 V_y Average absolute validation comparison error $|E|$ - Lower error highlighted

V_x	Y/a = 1.4	Y/a = 4.2	Y/a = 7	Y/a = 10	Y/a = 11.5
K-eps EXP	0.0054	0.0046	0.0055	0.0039	0.0038
K-eps UNI	0.0091	0.0065	0.0047	0.0032	0.0027
SST EXP	0.0059	0.0060	0.0058	0.0047	0.0044
SST UNI	0.0077	0.0077	0.0064	0.0043	0.0036
RSM EXP	0.0126	0.0117	0.0095	0.0077	0.007
RSM UNI	0.0176	0.0154	0.0078	0.0079	0.0071

Tab. 5.33 V_x Average absolute validation comparison error $|E|$ - Lower errors highlighted

6 Comments and Future Work

In the region close to the inlet nozzles, in the range of $1.4 < y/a < 4.2$, the merging and part of the combining region, the simulations velocities profiles of the streamwise velocity component V_y , have more or less the same average absolute modelling error $|E|$, and maximum absolute modelling error $|E|_{max}$. The sensitivity, on the V_y profiles, of Inlet boundary conditions, in this region, is not very appreciable.

On the opposite side, the velocity V_x component profiles, show a sensible influence from the boundary conditions, in fact the experimental inlet velocity profile boundary condition, gives better results and a low average validation comparison error $|E|$, and $\kappa - \varepsilon$ and SST turbulence models, are similar in terms of error.

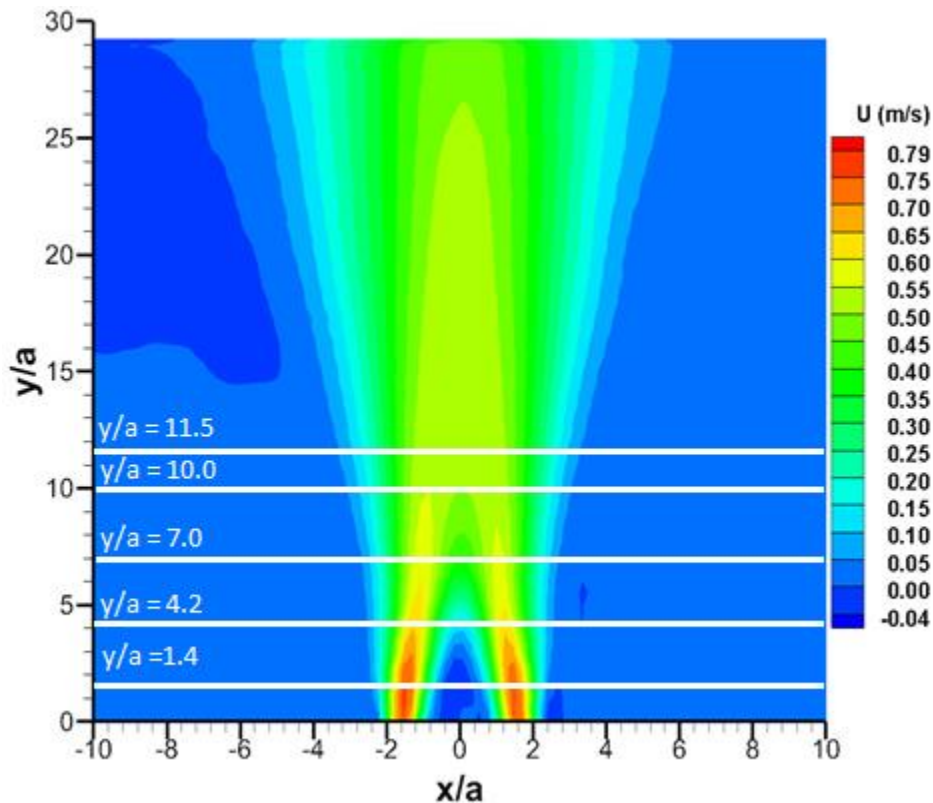


Figure 6.4 Experimental measurements heights

In the developed combined region $4.2 < y/a < 11.5$, the SSG Reynolds Stress Model, gives the poorest quality results, it tends to be less diffusive than the $\kappa - \varepsilon$ and SST turbulence models. In this region, $\kappa - \varepsilon$ and SST models, have comparable results, with better predictions for the $\kappa - \varepsilon$ model. In this region, the influence of boundary conditions, start to be effective and appreciable.

The V_y velocity profiles, for the uniform inlet velocity boundary case, tend to be symmetrical along their centerline, instead the V_y velocity profiles, for the experimental boundary condition, tends to better capture the asymmetry of the profile.

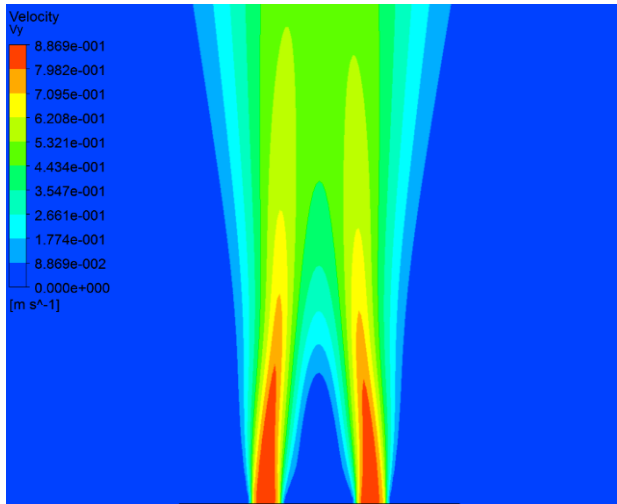


Figure 6.5 V_y -Experimental B.C.

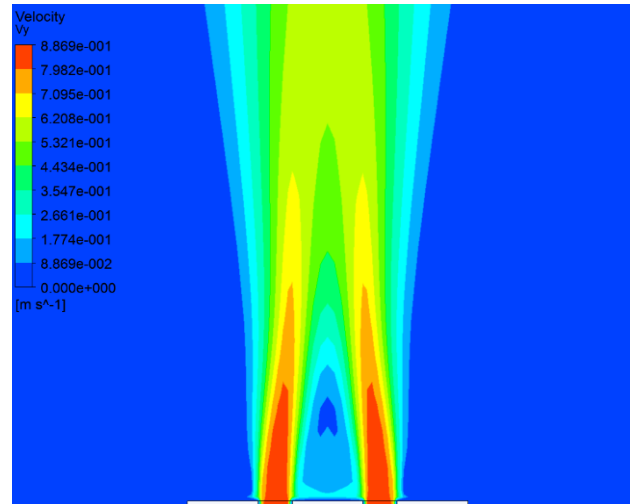


Figure 6.3 V_y -Uniform B.C.

For the velocity V_x profile instead, the influence of boundary conditions is less evident, but with a slightly lower average validation comparison error E for the uniform boundary case.

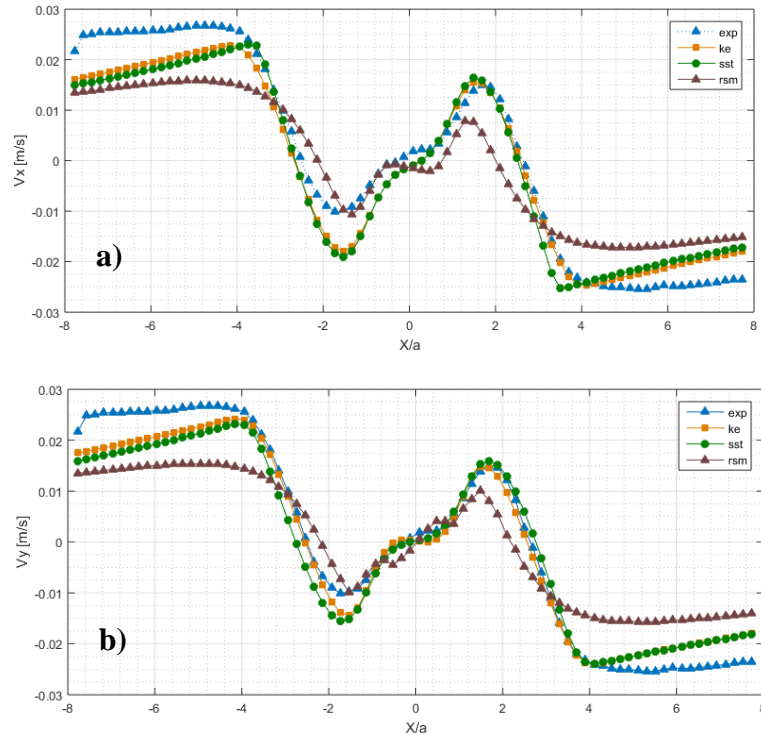


Figure 6.4 V_x at $Y/a = 11.5$ - a) Experimental B.C. case b) Uniform B.C. case

The evaluation of the average observed order of accuracy p_{obs} , shows that in every case its value is always between $0.5 p_{CFX} < p_{obs} < p_{CFX}$, where $p_{CFX} = 2$, except very few points, were locally, the observed order of accuracy is out of this range, we can state that the series of the simulation results are in the asymptotic range.

The GCI mean values are globally of the same order or lesser than the average experimental measurement uncertainties, except for some points of the domain where they are higher, and it is mainly because of the non-monotonic convergence of the coarse and medium mesh solutions towards the fine mesh, this will cause the intersections of the solutions profiles at some points as showed in Fig.6.5.

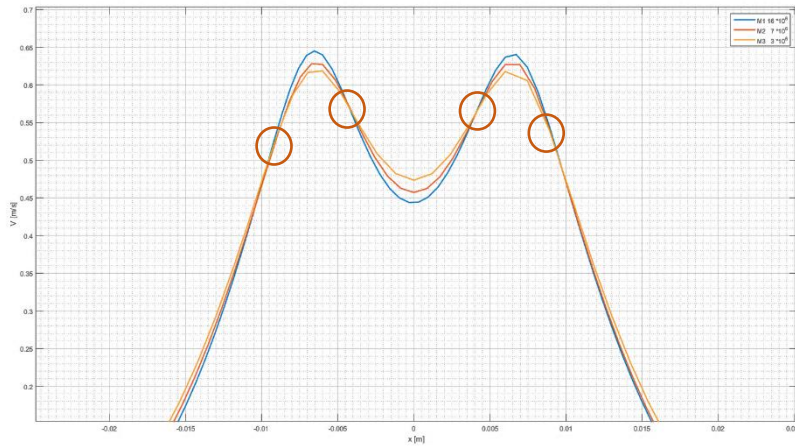


Fig. 6.5 Example - Non monotone convergence ($M1=16 \times 10^6$, $M2=7 \times 10^6$, $M3=3 \times 10^6$)

The solution verification part has been satisfactory but its main drawback is that it was very time consuming due to the large number of nodes required for reaching a set of mesh converging solutions (50 millions of nodes for the finest mesh), in the literature it has been presented another method for the evaluation of the observed order of convergence which requires a less number of nodes, it is the Least Square Method (LSM) by Eca and Hookestra [7], for the evaluation of the observed order of accuracy, but in order to be effective it necessitates at least a set of 4 different solutions on 4 different meshes.

The evaluation case by case, of the validation comparison error E and its associated uncertainty U , shows that for the V_y velocity profiles, there is always an order of magnitude of difference between the validation comparison error E and the validation uncertainty U . In this case it can be stated that the modelling error is the dominant part of the validation comparison error, since it is greater than the numerical and experimental uncertainty “noisy” level.

$$|E| \gg U_{val} \rightarrow \delta_{model} \cong E$$

Instead for the case of V_x , the average validation comparison error is greater, but of the same order, of the average uncertainty level, the modeling error is within the “noise level” imposed by the numerical, input, and experimental uncertainties.

For the Reynolds stress components, evaluated using the SSG Reynolds Stress Model, the degree of noisy level, on average, is greater or equal to the validation comparison error, so it can be stated that the modelling error is of the same order of the uncertainty noisy level.

$$|E| < U_{val} \rightarrow \delta_{model} \cong U$$

In this case as reported in Chapter 5, it can be seen that the validation comparison error $|E|$ is always within the $\pm U$, uncertainty level. The model can be defined validated with at the U validation uncertainty level, and since the major contribution to the global uncertainty U is given by the experimental uncertainty U_{exp} , nothing can be done from the CFD numerical side, since the numerical uncertainty U_{num} is always one order of magnitude lower.

It has been pointed out that in this work, for the validation part an important assumption has been made about the uncertainty due to the input parameters, $U_{input} = 0$. In the future for a complete and more reliable validation study, this component should be evaluated.

For the evaluation of the positions of the merging point MP and combining point CP, the experimental data range is quite large, but it can be seen that the results are largely affected by inlet boundary conditions, and the experimental velocity profile boundary gives the poorest results, compared to the uniform velocity profile boundary results. In the latter case the MP point is within the range of the experiments, while the CP is more downstream with respect to the experimental data range.

In this study it has been observed how the boundary conditions can affect the simulation results, a good evaluation of the velocity and turbulence inlet boundary conditions gives better validation results. It has also been observed as the k-epsilon turbulence model is no worse than SST or RSM turbulence models, but can give also better validation results, contrary to popular belief. Since it has been observed a large discrepancy between the experimental and the uniform boundary conditions solutions, in particular concerning the V_y profile asymmetry, that can be assessed to the asymmetrical nature of the inlet nozzle slot component (Fig.6.6), it can be proposed as a future work the use of a Hybrid LES-RANS model for a better characterization of the inlet conditions at the exit of the two rectangular nozzles, since the coupling between k-epsilon model and accurate inlet boundary conditions, especially turbulence quantities, has shown good predictive capabilities.

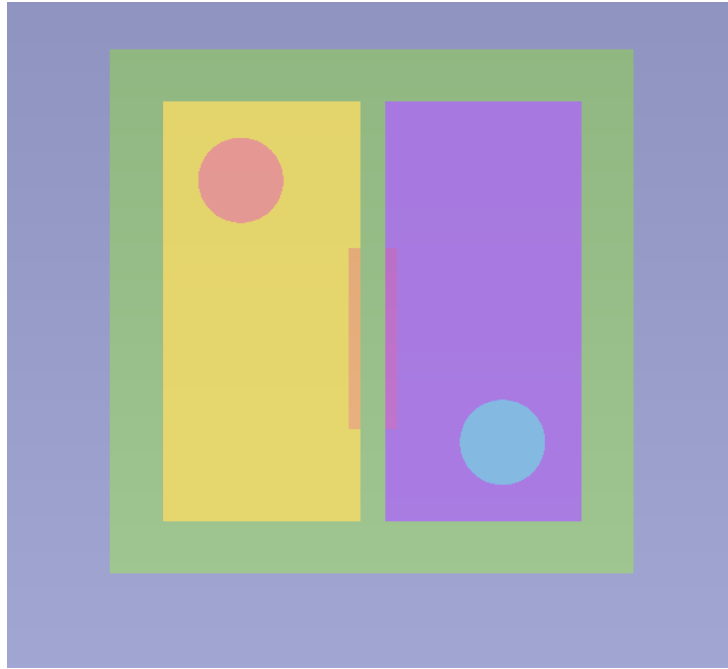


Figure 6.6 Bottom View of the nozzle slot inlet - asymmetry

7 References

1. Wang, H., Hassan, Y.A., “Benchmark Data for Validation of Computational Simulations of Nuclear System Thermal Fluids Behavior”, ASME V&V 30 Committee, December 2015.
2. Wang H., Lee S, Hassan Y.A., “Particle image velocimetry measurement of the flow in the converging region of two parallel jets”, Nuclear Engineering and Design, 2015.
3. ASME, “Standards for Verification and Validation in Computational Fluid Dynamics and Heat Transfer”, The American Society of Mechanical Engineers, 2009
4. Tanaka, M., “Application of Grid Convergence Index Estimation for Uncertainty Quantification in V&V of Multidimensional Thermal-Hydraulic Simulation”, ASME V&V Symposium, May 13-15, Las Vegas, Nevada, USA.
5. Roache, P.J., “Verification of Codes and Calculations”, AIAA Journal, Vol. 36, No.5, May 1998.
6. Sargent, R.G., “Verification and Validation of Simulation Models, Syracuse University

7. Oberkampf, W.L., Roy, C.J., “Verification and Validation in Scientific Computing”, Cambridge University Press, 2010.
8. Ferziger, J.H., Peric, M., “Computational Methods for Fluid Dynamics”, Springer, 3rd Edition 2002.
9. Eca, L., “Code Verification, Solution Verification and validation in RANS solvers”, ASME 2010 29th International Conference on Ocean, Offshore and Arctic Engineering, Shanghai, China June 2010
10. C.J. Roy, “Review of code and solution verification procedures for computational simulations”, Journal of Computational Physics, Volume 205, May 2005, pp: 131-156
11. Roache, P.J., “Perspective: A method for uniform reporting of grid refinement studies”, Journals of fluid engineering, vol 116, sept. 19947
12. ASME V&V 20 “Standard for Verification and Validation in Computational Fluid Dynamics and Heat Transfer”
13. ANSYS, “Ansys CFX-Solver theory guide”, Release 17.0